Aerial and Stratospheric Platforms and Reconfigurable Intelligent Surfaces in Future Wireless Networks

by

Safwan Alfattani

Thesis submitted to the
University of Ottawa
In partial fulfillment of the requirements
For the Ph.D. degree in
Electrical and Computer Engineering

School of Electrical Engineering and Computer Science
Faculty of Engineering
University of Ottawa

In the name of Allah, the Most Gracious, the Most Merciful

Abstract

Future wireless networks are envisioned to support a wide range of novel use cases, and connect a massive number of people and devices in an energy efficient way. Several key enabling technologies were considered to support this vision including Internet of Things (IoT) networks, aerial and stratospheric platforms, and reconfigurable intelligent surfaces (RIS). In this dissertation, we study different problems related to the integration between these technologies. First, we propose a cost-effective framework for data collection from IoT sensors using multiple unmanned aerial vehicles (UAVs). This is achieved by efficient clustering of the sensors and optimized deployment of cluster heads (CHs). Then, the number of deployed UAVs and their trajectories will be optimized to minimize the data collection flight time. The impacts of the trajectory approach, environment type, and UAVs' altitude as well as the fairness of UAVs trajectories on the data collection process are investigated. Given that IoT nodes might have different priorities and time deadlines, and respecting the limited battery capacity of UAVs, we enhance the data collection framework to account for these practical constraints. First, an algorithm for finding the minimal number of CHs and their best locations is proposed. Then, the minimal number of UAVs and their trajectories are obtained by solving the associated capacitated vehicle routing problem. The results investigate the impacts of the selected trajectory approach, the battery capacity and time deadlines on the consumed energy, number of visited CHs, and number of deployed UAVs. Next, given the energy issue on aerial platforms, we present our vision for integrating RIS in aerial and stratospheric platforms to provide energy-efficient communications. We propose a control architecture for such integration, discuss its benefits and identify potential use cases and associated research challenges. Then, to substantiate our vision, we study the link budget of RIS-assisted communications under the specular and the scattering reflection paradigms. Specifically, we analyze the characteristics of RIS-equipped stratospheric and aerial platforms and compare their communication performance with that of RIS-assisted terrestrial networks, using standardized channel models. In addition, we derive the optimal aerial platforms placements under both reflection paradigms. The obtained results provide important insights for the design of RIS-assisted communications. For instance, given that high altitude platform stations (HAPS) have large RIS surfaces, they provide superior link budget performance in most studied scenarios. In contrast, the limited RIS area on UAVs and the large propagation loss in low Earth orbit (LEO) satellite communications make them unfavorable candidates for supporting terrestrial users. Then, motivated by the demonstrated potential of HAPS equipped with RIS (HAPS-RIS), we propose a so-

lution to support the stranded users in terrestrial networks through a dedicated control station (CS) and HAPS-RIS. We refer to this approach as "*beyond-cell*" communications. We demonstrate that this approach works in tandem with legacy terrestrial networks to support uncovered or unserved users. Optimal transmit power and RIS unit assignment strategies for the users based on different network objectives are introduced. Furthermore, to increase the percentage of admitted users in an efficient manner, a novel resource-efficient optimization problem is formulated that maximizes the number of connected UEs, while minimizing the total power consumed by the CS and RIS. Since the resulting problem is a mixed-integer nonlinear program (MINLP), a low-complexity two-stage algorithm is developed. Finally, given the different applications and various options of HAPS payload, we envision the use of a multi-mode HAPS that can adaptively switch between different modes so as to reduce energy consumption and extend the HAPS loitering time. These modes comprise a HAPS super macro base station (HAPS-SMBS) mode for enhanced computing, caching, and communication services, a HAPS relay station (HAPS-RS) mode for active communication, and a HAPS-RIS mode for passive communication. This multi-mode HAPS ensures that operations rely mostly on the passive communication payload while switching to an energy-greedy active mode only when necessary. We illustrate the envisioned multi-mode HAPS, and discuss its benefits and challenges. Then, we validate the multi-mode efficiency through a case study. At the end of the dissertation, several future research directions are proposed including hybrid orthogonal and non-orthogonal multiple access (OMA/NOMA) beyond-cell communications assisted by HAPS-RIS, configuration of RIS units on stratospheric platforms, energy management for HAPS-RIS, and supporting aerial users through terrestrial RIS.

Dedicated to whom this thesis matters most,

My mother,
my father,
my wife, Esra,
and my kids (Maryam and Hassan).

Acknowledgements

First and foremost, I can never count the blessings and bounties of the Almighty Allah on me. All the praise is due purely to Him alone.

I would like to express my sincere gratitude to my supervisor Prof.Abbas Yongacoglu for his continuous support and invaluable guidance during my graduate study. His great experience and constant encouragement made my journey much easier.

My deepest appreciation goes also to my co-supervisor Prof. Halim Yanikomeroglu, for giving me the opportunity to work under his supervision. His great experience, deep technical knowledge and inspiring vision regarding the research directions made my PhD journey an interesting learning experience with tremendous success. His patience, dedication, manners, flexibility as well as continuous motivation and encouragement enabled me to overcome several challenges during my study. He is my role model for a great visionary scholar dedicated to research. From him, I learned a lot, not just the things related to my study and research.

My sincere gratitude and special thanks goes also to Prof. Wael Jaafar and Prof. Animesh Yadav, who were behind my success and achievements during my study. Their great expertise, detailed feedback, insightful comments, tremendous editing and enhancement efforts helped me to publish high quality papers in reputable venues. From them I learned a lot, and I am deeply thankful to them.

During my PhD journey, I was privileged to work and collaborate with experienced colleagues and excellent researchers. I would like to thank all whom I collaborate with, and all whom I learned from.

I am deeply grateful to the crucial role of my parents. Their patience, love, support, encouragement and prayers had significant impact on my life.

I am extremely thankful to my wife, Esra, for her patience, generous support, care and love during this journey. A special gratitude goes to my kids (Maryam and Hassan), who were born during my graduate study, for their love and patience.

Finally, I thankfully acknowledge that my graduate study journey was fully sponsored and and supported by a scholarship from King AbdulAziz University in Saudi Arabia.

Table of Contents

List of Tables xiii

List of Figures xiv

List of Abbreviations xvii

List of Publications xx

1 Introduction **1**

1.1 Thesis Objective 3

1.2 Thesis Outline and Organization 4

2 Multi-UAV Data Collection Framework for Wireless Sensor Networks **6**

2.1 Introduction 6

2.2 System Model 8

2.3 Problem Formulation 10

2.4 Proposed Solution 11

2.4.1 WSN Nodes Clustering 11

2.4.2 Trajectory Planning 12

2.4.2.1 UAVs hover exactly above CHs 13

2.4.2.2 UAVs hover within a range of CHs 15

2.5 Simulation Results 17

2.6 Conclusion 24

3 **Energy-Efficient Multi-UAV Data Collection for IoT Networks with Time Deadlines** **25**
3.1 Introduction . . . 25
3.2 System Model . . . 27
3.2.1 Network and Channel Models . . . 27
3.2.2 UAV Data Collection Model . . . 28
3.2.3 UAV Energy Model . . . 29
3.3 Problem Formulation . . . 30
3.4 Solution Approach . . . 32
3.4.1 IoT Sensors Clustering . . . 32
3.4.2 Multi-UAV Trajectory Planning . . . 34
3.5 Numerical Results . . . 35
3.6 Conclusion . . . 40

4 **Aerial Platforms with Reconfigurable Intelligent Surfaces for Beyond 5G** **42**
4.1 Introduction . . . 42
4.2 Overview of RIS in Communications . . . 44
4.2.1 Background . . . 44
4.2.2 Types of Communications with RIS . . . 45
4.2.2.1 RIS-Assisted Communications . . . 46
4.2.2.2 RIS-Initiated Communications . . . 46
4.3 Aerial Platforms with RIS: Integration and Control Architecture . . . 47
4.3.1 Ground Control Station . . . 47
4.3.2 Onboard Aerial Platform Control . . . 48
4.4 Aerial Platforms with RIS: Potential Use Cases . . . 48
4.4.1 HAPS with RIS to Support Remote Areas . . . 48
4.4.2 UAVs with RIS to Support Terrestrial and IoT Networks . . . 51

4.4.3 Tethered Balloons with RIS to Support Terrestrial/Aerial Users . . 53
4.5 Related Research Challenges 54
4.5.1 Accurate RIS and Aerial Channel Models 55
4.5.2 RIS Deployment on Aerial Platforms' Surfaces 55
4.5.3 Benchmarking the Operations of RIS, Relays, and MIMO 56
4.5.4 Simulation Tools for RIS Behavior 56
4.5.5 Channel Estimation and RIS Control Update 56
4.6 Conclusion 57

5 Link Budget Analysis for Reconfigurable Intelligent Surfaces in Aerial Platforms 58

5.1 Introduction 58
5.2 Link Budget Analysis for RIS-Assisted Terrestrial Networks 62
5.2.1 The Specular Reflection Paradigm 63
5.2.2 The Scattering Reflection Paradigm 64
5.2.2.1 Log-distance Channel Model 65
5.2.2.2 3GPP Channel Model 66
5.3 Link Budget Analysis for RIS-Assisted Non-Terrestrial Networks 67
5.3.1 Aerial Platforms Characteristics 68
5.3.2 The Specular Reflection Paradigm 69
5.3.3 The Scattering Reflection Paradigm 70
5.3.3.1 Log-distance Channel Model 71
5.3.3.2 3GPP Channel Model 72
5.4 Results and Discussion 78
5.4.1 Impact of the Number of Reflectors and Environment Type 78
5.4.2 Impact of the Carrier Frequency 81
5.4.3 Data Rate Evaluation and Impact of Platform Location 84
5.4.4 Outage Probability Analysis 86
5.5 Conclusion 89

6 Beyond-Cell Communications via HAPS-RIS 90
6.1 Introduction . . . 90
6.2 System Model . . . 92
6.2.1 Within-Cell Connection: UEs to Terrestrial BSs . . . 94
6.2.2 Beyond-Cell Connection: UEs to CS via HAPS-RIS . . . 95
6.3 Problem Formulation . . . 96
6.3.1 Sum Rate (Throughput) Maximization . . . 96
6.3.2 Minimum Rate Maximization (Max-Min Rate) . . . 97
6.3.3 Reflecting Units Minimization . . . 97
6.4 Resource-efficient Maximization . . . 98
6.5 Proposed Solution . . . 99
6.5.1 Sum Rate Maximization . . . 99
6.5.2 Minimum Rate Maximization (Max-Min Rate) . . . 100
6.5.3 Reflecting Units Minimization . . . 101
6.6 Resource-efficient Maximization . . . 101
6.6.0.1 Complexity Analysis . . . 103
6.7 Numerical Results and Discussion . . . 103
6.7.1 Relationship between BS Density and Direction Connection with UEs 106
6.7.2 Comparison Between Allocation Schemes . . . 107
6.7.2.1 Sum rate and worst UE rate maximization based allocation 107
6.7.2.2 Reflectors Minimization Based Allocation . . . 108
6.7.3 Resource-efficiency maximization . . . 108
6.7.4 Percentage of connected UEs . . . 108
6.8 Conclusion . . . 111

7 Multi-Mode HAPS for Next Generation Wireless Networks 112

7.1 Introduction . . . 112
7.2 HAPS versus other NTN Systems . . . 113
7.2.1 HAPS versus LEO Satellites . . . 114
7.2.2 HAPS versus UAVs . . . 114
7.3 Single-Mode HAPS Communication Payload . . . 115
7.3.1 HAPS-SMBS . . . 115
7.3.1.1 Increasing network capacity . . . 116
7.3.1.2 Supporting aerial networks and aerial users . . . 116
7.3.1.3 Supporting intelligent transportation systems . . . 117
7.3.1.4 Providing aerial datacenter services . . . 117
7.3.2 HAPS-RS . . . 117
7.3.2.1 Backhauling traffic from small cells . . . 118
7.3.2.2 Supporting IoT networks . . . 118
7.3.2.3 Establishing and maintaining inter-HAPS links . . . 118
7.3.3 HAPS-RIS . . . 118
7.3.3.1 Securing communications . . . 119
7.3.3.2 Supporting beyond-cell communications . . . 119
7.4 Proposed Multi-Mode HAPS Communication Payload . . . 120
7.4.1 HAPS Mode Selection . . . 121
7.4.2 Benefits . . . 122
7.4.3 Challenges and Research Directions . . . 122
7.5 Case Study . . . 123
7.5.1 HAPS-RS versus HAPS-RIS . . . 123
7.5.2 HAPS-SMBS versus HAPS-RS/HAPS-RIS . . . 126
7.6 Conclusion . . . 127

8 Summary and Future Work **128**

8.1 Summary . . . 128

8.2 Future Research Directions . . . 131

8.2.1 Hybrid OMA/NOMA Beyond-cell Communications Assisted by HAPS-RIS . . . 131

8.2.1.1 Frequency-division based NOMA transmission . . . 131

8.2.1.2 Time-division based NOMA transmission . . . 133

8.2.1.3 Problem Formulation . . . 133

8.2.2 Configuration of RIS-equipped Aerial Platforms . . . 134

8.2.2.1 System Model . . . 134

8.2.3 Energy Management for HAPS with Reconfigurable Smart Surfaces 136

8.2.3.1 System model . . . 137

8.2.4 Reconfigurable intelligent Surface-Assisted Control of Unmanned Aerial Vehicles in Dense Urban Environments . . . 138

8.2.4.1 System model . . . 140

8.2.4.2 Problem Description . . . 142

References **144**

List of Tables

3.1 Simulation parameters 39

4.1 Comparison between HAPS-RS and HAPS-RIS for communication 51

5.1 Parameters of HAPS/LEO LoS probability model (5.40) 74

5.2 Average clutter loss and shadow fading standard deviation in the Ka-band 75

5.3 Link Budget Summary 78

5.4 Typical parameters of different types of platforms. 78

List of Figures

2.1 System model. 8

2.2 Convergence of k-means (10 iterations). 17

2.3 Required number of CHs vs. communication range of SNs. 18

2.4 Distance traveled by the UAV vs. number of CHs. 19

2.5 Trajectories of UAVs. 20

2.6 Average traveled distance gain vs. UAV altitude. 20

2.7 An example of unfair and fair trajectory optimizations with 3 UAVs and 20 CHs. 21

2.8 Average distance traveled per UAV vs. number of CHs. 22

2.9 Standard deviation of trajectories vs. number of CHs. 23

3.1 System model of UAV-based data collection in clustered IoT networks with time deadlines. 28

3.2 Average number of CH vs. d_{th}. 35

3.3 An example of CHs locations and UAV trajectories (48 CHs and 11 UAVs). 36

3.4 Energy vs. battery capacity. 37

3.5 No. of CHs and UAVs vs. battery capacity. 37

3.6 Energy vs. deadline. 38

3.7 No. of CHs and UAVs vs. deadline. 38

4.1 Control architecture of RIS-equipped aerial platforms. 46

4.2 HAPS-RIS for backhauling remote gBSs, supporting IoT data collection and providing inter-HAPS communications. 49

4.3 Communication support of terrestrial networks with blockages using UxNB-RIS. 53

4.4 Communications support of terrestrial and aerial users using TBAL-RIS. . . 55

5.1 System model of RIS in a terrestrial environment. 62

5.2 System model of an aerial platform equipped with RIS. 68

5.3 LoS probability of HAPS/LEO vs. elevation angle (different environments). 74

5.4 Attenuation due to atmospheric gases PL_g vs. frequency (different path lengths). 76

5.5 Scintillation loss PL_s vs. elevation angle. 77

5.6 Received power vs. number of reflectors (different platforms; specular reflection paradigm). 80

5.7 Received power vs. number of reflectors (different platforms and environment types; scattering reflection paradigm). 81

5.8 Received power vs. carrier frequency (different platforms). 82

5.9 Received power vs. carrier frequency (different platforms and environment types). 83

5.10 Data rate vs. receiver antenna gain. 85

5.11 Data rate vs. normalized Rx-RIS distance ν (different platforms and environment types). 86

5.12 cdf of the received power at ground terminals assisted by RIS-equipped aerial platforms (different environment types). 88

5.13 Outage probability vs. coverage radius for RIS-assisted communications (different environment types). 88

6.1 System model for HAPS-RIS beyond-cell communications. 93

6.2 Locations of the UEs $\in \{\mathcal{K}_1, \mathcal{K}_2\}$ and BSs ($f_c = 2$ GHz, $\sigma_{\text{BS}-\text{UE}} = 8$ dB). . . 104

6.3 Relation between BS densities and percentage of UEs with direct connections for different frequencies. 105

6.4 Comparison between terrestrial and HAPS-RIS communications with different allocation strategies. 105

6.5 Relation between R_{min} for HAPS-RIS served UEs and the total required number of reflecting units. 106

6.6 Resource-efficiency performance of connected UEs for different R_{min}. 109

6.7 Maximizing connected UEs performance for different N_{max}. 109

6.8 Maximizing connected UEs performance for different $P^{\text{CS}}_{\text{max}}$. 110

7.1 Relation between applications and enabling HAPS modes. 120

7.2 HAPS mode selection mechanism. 121

7.3 Backhauling capacity comparison between HAPS-RS and HAPS-RIS. . . . 124

7.4 Energy efficiency comparison between HAPS-RS and HAPS-RIS. 125

7.5 Latency comparison between HAPS-SMBS and HAPS-RS/HAPS-RIS. . . 126

8.1 Hybrid OMA/NOMA scheme, where UEs in the same cluster use OMA scheme. 132

8.2 RIS on aerial platforms focus the reflected signal toward a targeted user. . 136

8.3 HAPS onboard subsystems. 138

8.4 BS-UAV communications are supported by reflections from smart buildings. 142

List of Abbreviations

Acronym	**Meaning**
3D	Three Dimensional
3GPP	Third Generation Partnership Project
5G	Fifth Generation
BS	Base Station
CAPEX	Capital Expenditures
CAV	Connected Autonomous Vehicle
CH	Cluster Heads
CITC	Communications and Information Technology Commission
CS	Control Station
CSI	Channel State Information
CVRPTW	Capacitated Vehicle Routing Problem with Time Windows
EE	Energy Efficiency
EM	Electromagnetic Waves
FIR	Finite Impulse Response
FSO	Free-Space Optics
FSPL	Free-space Propagation
FSS	Frequency Selective Surfaces
GA	Genetic Algorithm
GLS	Guided Local Search
gNB	Ground Node B
GP	Geometric Programming
HAPS	High Altitude Platform Stations
HAPS-BS	HAPS Base Station

HAPS-RIS	HAPS equipped with RIS
HAPS-RS	HAPS Relay Station
HAPS-SMBS	HAPS Super Macro Base Station
HCA	Hierarchical Cluster Analysis
IoT	Internet of Things
ITS	Intelligent Transportation System
ITU	International Telecommunication Union
LEO	Low Earch Orbit
LoS	Line of Sight
LRIS	Large-sized RIS
MIMO	Massive Multiple-Input Multiple-Output
MINLP	Mixed-Integer Nonlinear Program
mmWave	millimeter-wave
NLoS	Non Line of Sight
NN	Nearest Neighbor
NOMA	Non Orthogonal Multiple Access
NTN	Non-Terrestrial Networks
OFDM	Orthogonal Frequency Division Multiplexing
OMA	Orthogonal Multiple Access
OPEX	Operational Expenditures
PAGEOS	Passive Geodetic Earth Orbiting Satellite
PLS	Physical Layer Security
PV	Photovoltaic
QoS	Quality-of-Service
RC	Reflection Coefficient
RE	Resource-Efficiency
RF	Radio Frequency
RIS	Reconfigurable Intelligent Surfaces
SINR	Signal-to-Interference-plus-Noise Ratio
SN	Sensor Node
SNR	Signal-to-Noise Ratio
SR	Sum Rate
SRIS	Small-sized RIS
SWAP	Size, Weight, and Power

TBAL-RIS	Tethered Balloon Equipped with RIS
TDMA	Time-Division Multiple Access
THz	Terahertz
TSP	Travelling Salesman Problem
TSPN	Travelling Salesman Problem with Neighborhoods
UAV	Unmanned Aerial Vehicle
UE	User Equipment
UxNB	UAV Base Station/Relay
VR/AR	Virtual/Augmented Reality
WSN	Wireless Sensor Network

List of Publications

S. Alfattani, W. Jaafar, H. Yanikomeroglu, and A. Yongacoglu, "Multi-UAV data collection framework for wireless sensor networks", *IEEE Global Communications Conference (Globecom)*, Waikoloa, Hawaii, USA, Dec. 2019, pp. 1-6.

O. Ghdiri, W. Jaafar, **S. Alfattani**, J. Ben Abderrazak and H. Yanikomeroglu, "Energy-efficient multi-UAV data collection for IoT networks with time deadlines", *IEEE Global Communications Conference (Globecom)*, Taipei, Taiwan, Dec. 2020, pp. 1-6.

O. Ghdiri, W. Jaafar, **S. Alfattani**, J. Ben Abderrazak and H. Yanikomeroglu, "Offline and online UAV-enabled data collection in time-constrained IoT networks", *IEEE Transactions on Green Communications and Networking,* vol. 5, no. 4, pp. 1918-1933, Dec. 2021.

S. Alfattani, W. Jaafar, Y. Hmamouche, H. Yanikomeroglu, A. Yongacoglu, N. Đào and P. Zhu "Aerial platforms with reconfigurable smart surfaces for 5G and beyond", *IEEE Communications Magazine*, vol. 59, no. 1, pp. 96–102, Jan. 2021.

S. Alfattani, W. Jaafar, Y. Hmamouche, H. Yanikomeroglu and A. Yongacoglu, "Link budget analysis for reconfigurable smart surfaces in aerial platforms", *IEEE Open Journal of the Communications Society,* vol. 2, pp. 1980-1995, 2021.

G. Kurt, M. G. Khoshkholgh, **S. Alfattani**, A. Ibrahim, T. Darwish, M. Alam, H. Yanikomeroglu, and A. Yongacoglu, "A vision and framework for the high altitude platform station (HAPS) networks of the future", *IEEE Communications Surveys and Tutorials*, vol. 23, no. 2, pp. 729 – 779, Secondquarter 2021.

M. Rivera, M. Chegini, Wael Jaafar, **S. Alfattani**, and H. Yanikomeroglu, "Optimization of quantized phase shifts for reconfigurable smart surfaces assisted communications", *IEEE Consumer Communications & Networking Conference (CCNC)*, Las Vegas, NV, USA, Jan. 2022, pp. 1-4.

S. Alfattani, A. Yadav, H. Yanikomeroglu, and A. Yongacoglu, "Beyond-Cell Communications via HAPS-RIS", *IEEE Global Communications Conference (Globecom)*, 04–08 December 2022, Rio de Janeiro, Brazil.

S. Alfattani, A. Yadav, H. Yanikomeroglu, and A. Yongacoglu, "Resource-efficient HAPS-RIS enabled beyond-cell communications", under review in *IEEE Wireless Communications Letters*, (submission: 20 Jul 2022, 1st results: 16 Sep 2022, 2nd submission: 27 Oct 2022).

S. Alfattani, W. Jaafar, H. Yanikomeroglu, and A. Yongacoglu, "Multi-mode high altitude platform stations (HAPS) for next generation wireless networks", under review in *IEEE Vehicular Technology Magazine*, (submission: 17 Sep 2022).

S. Alfattani, W. Jaafar, H. Yanikomeroglu, and A. Yongacoglu, "Multi-mode high altitude platform stations (HAPS) for next generation wireless networks", in *Young Scholars Competition on Non-Terrestrial Networks for B5G and 6G*, by *IEEE Future Networks Initiative,* (Selected as the best work and awarded the grand prize of the competition in "*Connecting the World from the Skies*" forum, Riyadh, Saudi Arabia 8-10 Nov. 2022).

Chapter 1

Introduction

The evolution of the wireless communications in the last few decades has a major contribution to the witnessed socio-technical development in the world. Wireless networks were evolved from solely voice calling in the first generation (1G) to support Internet applications and video streaming in the fourth generation (4G). In the past four generations of wireless networks, the developments were primarily focused on achieving higher data rates. However, given the rapid increasing of mobile subscribers, and the continuous evolving roles and applications of wireless networks in our life, the fifth generation and beyond (5G/B5G) will be a paradigm shift in wireless technologies. In addition to supporting the traditional communication services, future generations of wireless networks will support various new use cases and applications. Examples of such applications include autonomous cars, virtual and augmented reality applications, smart grid, e-health[1], emergency response and intelligent transportation systems. This vision of wide range applications requires reliable and ubiquitous connectivity for massive number of connected devices. Indeed, among the main capabilities and requirements of future wireless networks, defined by the International Telecommunication Union (ITU), are enhanced mobile broadband (eMBB) and massive machine type communications (mMTC) [1]. According to Cisco forecasts [2], the number of connected devices will be 29.3 billion by 2023, and the average broadband speeds will be 110 Mbps.

To support these connectivity demands and the envisioned novel use cases, researchers in the wireless community are continuously investigating new technologies and approaches

[1] E-health refers to health services and information delivered or enhanced through the Internet and the applications of information and communications technologies.

to enhance different aspects of future wireless networks. These efforts include seeking for techniques and technologies to enhance the radio access networks (RAN), the energy efficiency of the communication systems, and the scalability of connected devices. Our focus in this thesis on three of the enabling technologies introduced for future wireless networks: *aerial and stratospheric platforms*, *Internet of Things (IoT) networks* and *reconfigurable intelligent surfaces (RIS)*.

Aerial and stratospheric platforms are considered as an essential part of the ecosystems of future generations wireless networks. Aerial platforms include unmanned aerial vehicles (UAVs), which are typically small sizes platforms deployed at altitudes around 100 m. On the other hand, stratospheric platforms refer specifically to high altitude platform stations (HAPS), which are generally large platforms deployed at altitudes around 20 km. Several researchers studied different aspects regarding the utilization of aerial platforms in 5G/B5G networks [3, 4, 5, 6]. Moreover, the Third Generation Partnership Project (3GPP) issued several standards and studies regarding the deployment scenarios of aerial and stratospheric platforms, the details of their channel models and related system parameters such as antenna architecture, altitude, etc. [7, 8, 9]. In general, this interest in utilizing aerial and stratospheric platforms is due to their unique characteristics, which include wide service coverage capabilities, preferred communication channels and flexible deployment. Thus, aerial and stratospheric platforms has the potential to roll out the sixth generation (6G) services in un-served or underserved areas and reinforce the reliability and the scalability of terrestrial netwroks.

IoT networks, which consist of large number of devices connected to the internet, are considered as one of the main trends in future networks and a prime enabler for mMTC use cases [1]. IoT sensors are an essential part of IoT networks. They consist of low-cost and low-complexity devices that have the ability to detect or measure various physical phenomena such as temperature, pressure, light and speed. Thus, the deployment of IoT networks will be the base driver for future novel applications such as driverless cars, smart grid and intelligent transportation systems. It is projected that about 50% (14.7 billion) of total global devices will be IoT based devices [2]. IoT sensors are expected to be deployed in wide and hard ot reach areas to provide industrial, agricultural and environmental solutions. They can be utilized to predict equipment failure, weather patterns, crop rotation, yield predictions and various other impacts on agriculture and the food industry.

While the previous two enabler technologies enhance the scalability and the radio access of future networks, *Reconfigurable intelligent surfaces (RIS)* technology improves the energy efficiency of wireless communications. RIS are low-cost, thin and lightweight metasurface integrated with passive electronic components or switches to provide a customized interaction and controlled manipulation of the wireless signals. They can alter the amplitude of the impinging signal, adjust its phase, and direct it to a target in a nearly passive way. Due to the intrinsic features of RIS, they can be integrated in walls, ceilings, surfaces and facades of buildings. Recently, there has been a significant growing interest from both academia and industry to utilize the RIS technology and enhance different aspects of wireless communications performance, such as capacity, reliability and security. Indeed, due to the passive nature of RIS technology, it is considered as one of the energy-efficient promising technologies for future wireless networks [10, 11, 12].

1.1 Thesis Objective

The potentials and advantages of the aforementioned technologies for future wireless networks are well addressed and demonstrated in the literature. However, instead of looking to these technologies as standalone technologies, more benefits and capabilities can be attained when these technologies are working cooperatively or in an integrated manner. We envision that careful integration of multiple technologies will be an essential key enabler for novel use cases and scenarios in future wireless networks. Also, unique characteristics and distinctive features are expected of such integration. In addition, numerous benefits can be realized by integrating these enabling technologies. The integration is expected to provide better radio access network and easily scalable networks. Also, it is expected to improve the spectral and the energy efficiencies of wireless networks. However, this integration poses several challenges and issues that need to be studied and analyzed.

Our goal in this dissertation is to investigate several problems associated to different kinds of integration of these aforementioned technologies. In particular, we study the utilization of unmanned aerial vehicles (UAVs) for data collection in IoT networks. We proposed a cost-effective IoT network deployment and an energy-efficient UAVs trajectory planing. To provide an agile and an energy-efficient network, we propose the integration of RIS technology on aerial and stratospheric platforms. Then, the potentials of such integration for different applications including wireless communication and IoT data collection will be analyzed and demonstrated in this thesis. In addition, related problems of such integration for system performance optimization will be studied and investigated.

1.2 Thesis Outline and Organization

In Chapter 2, we introduced a cost-effective data collection framework for wireless sensor networks (WSNs) using muliple UAVs. We aimed in this Chapter to deploy minimum number of cluster heads (CHs) in WSNs, and optimize the trajectories of the UAVs in terms of the traveled distances. Also, we investigated the effects of the environment and the altitude of the UAVs to the data collection performance. In addition, the importance of fairness in UAVs trajectory planning is highlighted.

The framework presented in Chapter 2 was extended in Chapter 3 to large-scale IoT systems, while taking into account the limited energy of UAVs and the time deadlines of IoT sensors. The system considers multiple UAVs deployed to collect sensed data with different time deadlines. In this chapter, we proposed an algorithm that outperform benchmark approaches for deploying minimum number of CHs in IoT networks. Furthermore, by utilizing different heuristic algorithms, we optimize the trajectories of multiple UAVs. The impact of the UAVs' battery capacities and the IoT sensors' time deadlines on the data collection performance and the associated energy consumption were also discussed.

Given the limited energy issues of UAVs demonstrated in Chapter 3, we proposed in Chapter 4 a new technology for the communication payload of aerial and stratospheric platforms that offer energy-efficient communications. In particular, in Chapter 4, we presented our vision for integrating RIS on different aerial platforms including high altitude platform stations (HAPS), UAVs, tethered balloons. Also, we presented the proposed control architecture workflow for communication, mobility, and sensing for RIS-equipped aerial platforms. Furthermore, we discussed in details the potential use cases and the attendant benefits of such integration compared to traditional technologies. We concluded Chapter 4 by highlighting main research challenges associated with this integration.

To support our vision presented in Chapter 4, we analyzed in Chapter 5 the link budget of RIS-equipped aerial platform communication systems under both specular and scattering reflection paradigms. Furthermore, we derived the optimal platform location and feasible maximum number of RIS reflectors onboard of each platform. Also, we utilized the 3GPP standards for the communication models to derive the link budget expressions for realistic communication conditions. We concluded the chapter by providing some design guidelines regarding the utilization of RIS on aerial and stratospheric platforms.

Based on the findings in Chapter 5, where HAPS equipped with RIS (HAPS-RIS) have shown significant potentials and performance gain compared to other alternatives, we studied in Chapter 6 the utilization of HAPS-RIS for beyond-cell communications. Particularly, we proposed using HAPS-RIS connected to a control station (CS) to support unserved users in terrestrial networks. Based on different network operating objectives, several optimization problems to design the CS power and RIS unit allocation strategies were investigated. The objectives include throughput maximization, worst user rate maximization, and RIS units minimization. Furthermore, for a large density of users and limited CS power and HAPS-RIS size, a novel resource-efficient optimization problem is formulated, which simultaneously maximizes the percentage of connected UEs using minimal CS power and RIS units. Through the results of Chapter 6, we showed the capability of *beyond-cell* communications via HAPS-RIS to support a larger number of users with limited number of terrestrial base stations (BSs). Furthermore, the results showed the superiority of the proposed approach over benchmark and conventional solutions. Also, the results demonstrated the trade-off between different solutions in terms of average rate performance and fairness between users. Finally, the impacts of the HAPS size and different QoS requirements on the percentage of connected UEs and the efficiency of the system were discussed.

Given the various options, capabilities and energy requirements of HAPS communication payload (including HAPS super macro base station (HAPS-SMBS), HAPS relay station (HAPS-RS) and HAPS-RIS), we envision in Chapter 7 a novel multi-mode HAPS payload that can deceptively switch between multiple modes. This multi-mode HAPS is expected to increase the HAPS capabilities while minimizing the energy consumption and extending the loitering time. We discussed in this chapter the mechanism for mode selection, the advantages and the related challenges of this multi-mode HAPS. Finally, through a case study the performance differences between these modes were analyzed and the conditions for modes selection were identified.

In Chapter 8, we provided a summary of the conducted work in this dissertation. Also, a brief description of some future research directions is presented.

Chapter 2

Multi-UAV Data Collection Framework for Wireless Sensor Networks

2.1 Introduction

In wireless sensor networks (WSNs), a large number of sensor nodes (SNs) is usually deployed to detect physical phenomena, e.g., pressure, temperature, etc. As part of the Internet of Things (IoT), WSNs are everywhere today, enabling new applications including smart grids, water networks, and intelligent transportation. In these systems, SNs are low-power devices with typically short transmission ranges. Current IoT SNs are based on IEEE 802.15/802.11af and they have a maximum communication range of few hundred meters. In such systems, data sensed by SNs needs to be transmitted to a network manager. Typical WSNs deploy sinks (gateways) to collect SNs data and forward it to the Internet. However, due to the limited range of SNs, large numbers of sinks are deployed, which raise capital and operating expenses.

To extend the lifetime of WSNs, the utilization of static or mobile distributed relay nodes within WSNs is proposed in [13]. Recently, low altitude platforms based on unmanned aerial vehicles (UAVs) have been presented as a promising technology to enable several wireless applications such as coverage extension, disaster/emergency situation man-

This work mainly has been published in IEEE Globecom 2019 proceedings: **S. Alfattani**, W. Jaafar, H. Yanikomeroglu, and A. Yongacoglu, "Multi-UAV data collection framework for wireless sensor networks", *IEEE Global Communications Conference* (Globecom), Waikoloa, Hawaii, USA, Dec. 2019, pp. 1-6.

agement, etc. [14, 15]. In the context of WSNs, UAVs can act as relay nodes or as data collectors from SNs. In [16], with SNs partitioned into clusters, UAVs were used to collect data from them. However, this work was limited to static networks and one type of environment. Also, optimal deployment of UAVs has not been investigated. Authors in [17, 18] investigated the deployment and trajectory of a single UAV supporting downlink wireless communications only. These works are limited since they focused only on downlink communications using one UAV. In [19], a single UAV was used to communicate with ground nodes. The UAV's trajectory was optimized to minimize power consumption. However, multiple UAVs were not considered. Authors of [20] proposed clustering to find optimal hovering locations for UAVs that minimize the power consumption of IoT devices. Nevertheless, the required number of UAVs or clusters for a cost-effective deployment was not considered in this work. Also, the effects of the environment type and the UAV altitude on the data collection process was not investigated.

Most of the previous studies investigated single UAV deployments and ignored multi-UAV cases. Moreover, communications with low-power SNs is impractical, and hence deploying cluster heads (CHs) with higher power capabilities, in conjunction with UAVs, is considered as an energy-efficient approach [21]. Also, most state-of-the-art research considered perfect Line-of-Sight (LoS) channels between UAVs and SNs. This is not true in urban environments, where Non-LoS (NLoS) links exist. Being conscious of these limitations, we address in this chapter the problem of designing an efficient multi-UAV data collection framework in WSNs that reduces the number of clusters of SNs and minimizes the UAVs total flight time.

The main contributions in this Chapter is summarized as follows: we propose a cost-effective WSN framework where the number of CHs and their locations, and UAVs and their trajectories are optimized to collect WSN data in the shortest possible time. First, using k-means clustering, the number and locations of CHs are optimized, such that each SN can communicate reliably with its associated CH. Then, by leveraging several heuristic solutions of the multiple Travelling Salesman Problem (mTSP) and TSP with neighborhoods (TSPN), we find trajectories of UAVs guaranteeing both reliable data collection and the shortest total flight times. These heuristic solutions include the genetic algorithm (GA) and the nearest neighbor (NN) approach. The results include guidelines for WSN data collection design: The proposed k-means-based clustering algorithm provides optimal numbers of CHs to deploy. The adopted GA approach for designing the UAVs trajectories significantly outperform the NN algorithm. Also, it is found that GA is near-optimal in

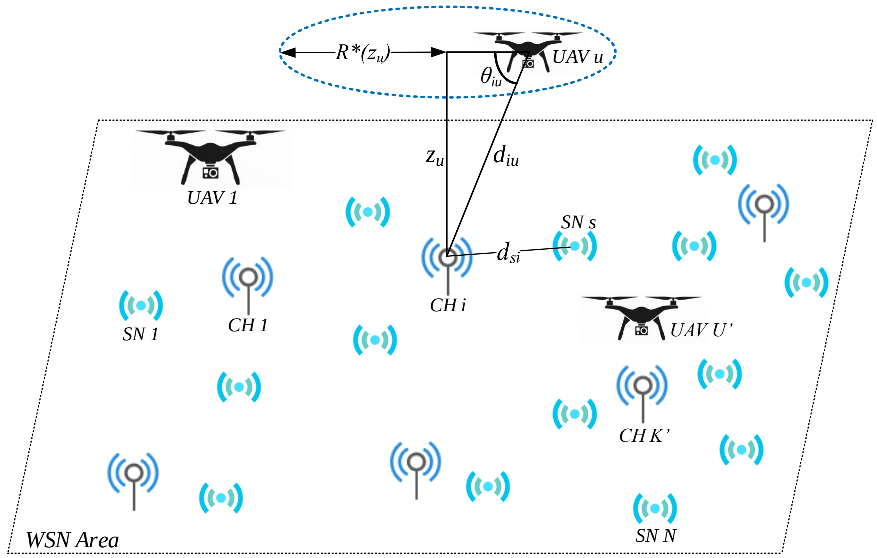

Figure 2.1: System model.

determining trajectories of UAVs, with less than 3.5% degradation to the optimal solution, optained through Matlab solver. By utilizing the coverage area of each CH to hover within that range, significantly improves the UAV's flight time. Moreover, the environment type and the UAV's altitude impact data collection time. Finally, integrating trajectory fairness in multi-UAV large WSNs improves the data collection performance.

2.2 System Model

We assume a WSN network, where a set of $\mathcal{N} = \{1, \ldots, N\}$ SNs are randomly located. SNs sense different kinds of data that they need to transmit to the network. We assume that several UAVs are deployed to collect SNs' data, as depicted in Fig. 2.1. SNs are typically low power devices that cannot communicate directly with UAVs, hence a set $\mathcal{K} = \{1, \ldots, K\}$ of CHs are deployed to collect data and send it to UAVs. We assume that a SN transmits its data to its associated CH using power P_{SN}, while a CH communicates with a UAV with power $P_{\text{CH}} > P_{\text{SN}}$. Moreover, all communications are assumed to be orthogonal, i.e., no interference is occurring. Collection of data occurs as follows. After association with CH c, SN s transmits its data. The received signal-to-noise ratio (SNR) at CH c, γ_{sc}, can be written as

$$\gamma_{sc} = \frac{P_{\mathrm{SN}} d_{sc}^{-\alpha}}{\sigma^2}, \ \ \forall s \in \mathcal{N}, \ \forall c \in \mathcal{K}, \tag{2.1}$$

where $d_{sc} = ||\mathbf{q}_s - \mathbf{q}_c||$ is the distance between IoT sensor s and CH c, $\mathbf{q}_i = [x_i, y_i, z_i]$ is the 3D location of node i ($i = s$ or c), α is the path-loss exponent, and σ^2 is the noise power. This communication link is considered successful if $\gamma_{sc} \geq \gamma_{\mathrm{th}}$, where γ_{th} is a chosen SNR threshold. Consequently, a maximum communication range for SN s can be defined by

$$d_{sc} \leq d_s^{\mathrm{th}} = \left(\frac{P_{\mathrm{SN}}}{\sigma^2 \gamma_{\mathrm{th}}}\right)^{1/\alpha}, \ \ \forall s \in \mathcal{A}_c, \ c \in \mathcal{K} \tag{2.2}$$

where $\mathcal{A}_c = \{\mathrm{SN}\ s \mid d_{sc} \leq d_s^{\mathrm{th}}\}$ is the set of sensors associated with CH c, $\forall c = 1, \ldots, K'$[1].

Once data is received, CH c waits for UAV u to hover above its position to send it Q_c data packets of size S_p bits each. Let $\mathcal{U} = \{1, \ldots, U\}$ be the set of available UAVs for CHs data collection. The air-to-ground channel between UAV u and CH c can be expressed using the probabilistic path loss model given by [23]

$$\Lambda_{cu} = \mathbb{P}_{cu}^{\mathrm{LoS}} \ l_{cu}^{\mathrm{LoS}} + \mathbb{P}_{cu}^{\mathrm{NLoS}} \ l_{cu}^{\mathrm{NLoS}}, \ \forall c \in \mathcal{K}, \ \forall u \in \mathcal{U}, \tag{2.3}$$

where Λ_{cu} is the average path-loss between CH c and UAV u, $\mathbb{P}_{cu}^{\mathrm{LoS}}$ is the LoS probability, $\mathbb{P}_{cu}^{\mathrm{NLoS}} = 1 - \mathbb{P}_{cu}^{\mathrm{LoS}}$ is the NLoS probability, and l_{cu}^{LoS} and l_{cu}^{NLoS} are the LoS and NLoS path-losses. They are written as [23]

$$\mathbb{P}_{cu}^{\mathrm{LoS}} = 1/\left(1 + a\ e^{-b(\frac{180}{\pi}\theta_{cu} - a)}\right), \tag{2.4}$$

$$l_{cu}^{m} = L_{\mathrm{FS}}(f_c) + 20 \log\left(d_{cu}\right) + \beta_m, \ \forall m \in \{\mathrm{LoS}, \mathrm{NLoS}\} \tag{2.5}$$

where a and b are constants dictated by the environment (rural, urban, etc.), d_{cu} and θ_{cu} are the distance (in m) and angle (in rad) between CH c and UAV u respectively, depicted in Fig. 3.2. $L_{\mathrm{FS}}(f_c) = 20 \log\left(4\pi f_c/V\right)$, with f_c is the carrier frequency and V the light's velocity, and β_m is the excessive path-loss coefficient. Using Friis formula, received power at UAV u from CH c in (dBm) is expressed by [23]

$$P_{cu}^{\mathrm{UAV}} = P_{\mathrm{CH}} - \Lambda_{cu} \geq P_{\mathrm{th}}, \ \ \forall c \in \mathcal{K}, \ \forall u \in \mathcal{U}, \tag{2.6}$$

[1] Since one of the main characteristics of different SNs types is the communication range, a distant-based model is utilized for SN-CH communication. However, a probabilistic 3D model can be also utilized to account for different environments [22].

where P_{th} is the UAV's receiver sensitivity, i.e., above it, the communication between CH c and UAV u is successful.

In the next section, we formulate the joint problem of deploying an optimal number of CHs and UAVs to collect data in the shortest time possible, while respecting budget (i.e., maximum number of deployable CHs and UAVs) and power constraints.

2.3 Problem Formulation

First, let $K' \leq K$ and $U' \leq U$ be the effective number of CHs and UAVs that are going to be deployed. Then, we define by $\mathcal{C}_u = \{\text{CH } c \mid P_{cu}^{\text{UAV}} \geq P_{\text{th}}\}$ the set of CHs associated with UAV u, $\forall u = 1, \ldots, U'$. The problem can be expressed as follows

$$\min_{\substack{\mathcal{A}_c, \mathcal{C}_u, \mathcal{W}_u, \mathcal{H}_u \\ c=1,\ldots,K' \\ u=1,\ldots,U'}} \quad \frac{1}{U'} \sum_{u=1}^{U'} \sum_{c \in \mathcal{C}_u} \|\mathbf{w}_{u,c+1} - \mathbf{w}_{u,c}\| / v_u \tag{P1}$$

$$\text{s.t.} \quad K' \leq K, \; U' \leq U, \tag{P1.a}$$

$$d_{sc} \leq d_s^{\text{th}}, \; \forall c = 1, \ldots, K', \; s \in \mathcal{A}_c \tag{P1.b}$$

$$P_{cu}^{\text{UAV}} \geq P_{\text{th}}, \; \forall u = 1, \ldots, U', \; \forall c \in \mathcal{C}_u, \tag{P1.c}$$

$$| \cup_{u=1}^{U'} \mathcal{C}_u | = K', \; \cap_{u=1}^{U'} \mathcal{C}_u = \emptyset, \tag{P1.d}$$

$$| \cup_{c=1}^{K'} \mathcal{A}_c | = N, \; \cap_{c=1}^{K'} \mathcal{A}_c = \emptyset, \tag{P1.e}$$

where $\mathcal{W}_u = \{\mathbf{w}_u = [x_{u,c}, y_{u,c}, z_{u,c}] \mid \forall c \in \mathcal{C}_u\}$ is the set of ordered locations to visit by UAV u (route) to collect data from its CHs, and $\mathbf{w}_u$ is the location in the Cartesian coordinates system. Similarly, $\mathcal{H}_u = \{\mathbf{h}_c = [x_c, y_c, z_c] \mid \forall c \in \mathcal{C}_u\}$ is the set of ordered locations of CHs to visit by UAV u. Moreover, $\mathbf{w}_{u,0} = \mathbf{w}_{u,|\mathcal{C}_u|+1}$ is UAV u's dockstation, and v_u is UAV u's average flight speed. Finally $|.|$ and $\|.\|$ are the Cardinality and Euclidean norm operators, respectively. The objective function minimizes the average data collection time, where we assume that communication time is fixed and long enough to collect all data from the CH successfully, hence ignored in this expression. Constraints (P1.a) are the budget limitations in terms of number of CHs and UAVs. Whereas, (P1.b)-(P1.c) and (P1.d)-(P1.e) guarantee successful communications and unique associations between the CHs–SNs and UAVs–CHs, respectively.

The formulated problem is NP-hard. Indeed, in the special case of one UAV and already deployed CHs with respect to (P1.d), the problem is reduced to finding the shortest UAV route. The latter can be comprehended as the TSP. In TSP, a salesman needs to visit a number of cities, while minimizing the traveled distance. Logically, the salesman and cities are assimilated by UAV and CHs respectively. Since TSP is NP-hard, then by restriction, our problem is also NP-hard.

2.4 Proposed Solution

Solving problem (P1) directly is very difficult. Hence, we opt for a two-step approach as follows: 1) For given K' and U', we find the locations of CHs to satisfy (P1.b), (P1.e), i.e., sets $\mathcal{A}_c$ ($c = 1, \ldots, K'$) and $\mathcal{H} = \cup_{u=1}^{U'} \mathcal{H}_u$. This step is the WSN nodes clustering. 2) Then, for each UAV, the associated CHs, the trajectory and exact aerial locations to visit are determined, i.e., $\mathcal{C}_u$, $\mathcal{H}_u$ and $\mathcal{W}_u$, $\forall u = 1, \ldots, U'$. This step is the trajectory planning. It is to be noted that the proposed approach yields a sub-optimal solution compared to the joint optimization of clustering and UAVs trajectory design. Nevertheless, it presents interesting implementation characteristics such as simplicity and full control of parameters.

2.4.1 WSN Nodes Clustering

Clustering SNs and deploying CHs to collect data is a widely used technique, as it is considered energy-efficient. Indeed, low-power SNs either cannot communicate directly with the collector (e.g., UAV) or the latter has to get very close to SNs to collect data, which is energy wasting. Also, using CHs permits the centralization and filtering of data before transmitting it to the network. By doing so, CHs are able to process huge amounts of data and guarantee the scalability of the WSN. Moreover, clustering tolerates failures and malfunctions through filtering, backup CHs, and re-clustering. Finally, by adequately deploying CHs, data loads can be balanced among CHs, in order to extend their availability in the WSN [21]. In the literature, several approaches exist, such as k-means [24], Mean-Shift, Density-Based Spatial clustering, etc. Due to the flexibility of k-means in terms of determining the number of CHs, we opt in this chapter for utilizing k-means to cluster SNs and place dedicated CHs. Hence, the associated clustering problem is

$$\min_{\mathcal{H},\mathcal{A}_c} \quad \sum_{c=1}^{K'} \sum_{s \in \mathcal{A}_c} \|\mathbf{g}_s - \mathbf{h}_c\|^2 \tag{P2}$$

$$\text{s.t.} \quad \text{(P1.a), (P1.b), (P1.e)}$$

where $\mathbf{g}_s = [x_s, y_s, z_s]$ is the location of SN s, $\forall s = 1, \ldots, N$. This problem is known to be NP-hard. k-means solves (P2) iteratively by updating the locations of CHs, as the averaged locations among SNs in the same cluster. The k-means method is inspired from [24]. However, to be adapted to our system, i.e. to satisfy additional constraints (P1.b) and (P1.e), we integrate it into proposed Algorithm 1. It is worth noting that the solution provided by k-means is usually a local optimal solution. To improve the solution to be global optimal or near optimal, several random initialization points for CHs locations are considered, and the best solution is selected.

Algorithm 1 Determining the number and locations of CHs

```
Initialize K' = 1
Initialize d_s^th using (2.2)
Run k-means [24], get H and A_1
Calculate d_max = max_{s∈C_1} ||g_s − h_1||
while d_max > d_s^th and K' < K do
    K' = K' + 1
    Run k-means [24], get H and A_c (i = c, ..., K')
    Calculate d_max = max_{s∈A_i, c=1,...,K'} ||g_s − h_c||
end while
Return H and A_c (c = 1, ..., K')
```

2.4.2 Trajectory Planning

With the minimum number of CHs deployed, (P1) is reduced to associating CHs to UAVs and finding best trajectories to collect data. Each UAV travels from its dockstation to associated CHs, hovers to collect data, and returns to its dockstation once all CHs have been visited. This problem is known as the mTSP. Despite its NP-hardness, several algorithms have been proposed in the literature [25]. First, we investigate trajectory optimization when UAVs hover exactly above CHs. Then, the case where UAVs hover within a range of CHs will be studied. The latter is known as TSPN [26].

2.4.2.1 UAVs hover exactly above CHs

For simplicity's sake, we assume that a UAV hovers at the same altitude for the whole trajectory, and that it hovers exactly above its associated CHs, such that constraints (P1.c and P1.d) are respected. Moreover, we assume that hovering time is fixed and long enough to collect all data from the CH successfully, and that UAVs have the same average flying speed $v_u = v_{avg}$, $\forall u = 1, \ldots, U'$. Hence, the trajectory planning problem can be written as [27]

$$\min_{\mathcal{X}} \quad \sum_{u=1}^{U'} \sum_{c=0}^{K'} \sum_{\substack{j=0 \\ j \neq c}}^{K'} \|\mathbf{h}_c - \mathbf{h}_j\| x_{cj}^u \tag{P3}$$

$$\text{s.t.} \quad \sum_{u=1}^{U'} \sum_{c=0}^{K'} x_{cj}^u = 1, \ \forall j = 0, \ldots, K', \ j \neq c \tag{P3.a}$$

$$\sum_{c=1}^{K'} x_{cp}^u - \sum_{j=1}^{K'} x_{pj}^u = 0, \ \forall p = 1, \ldots, K', \ \forall u \in \mathcal{U} \tag{P3.b}$$

$$\sum_{j=1}^{K'} x_{0j}^u = 1, \ \forall u = 1, \ldots, U' \tag{P3.c}$$

$$n_c - n_j + K' \sum_{u=1}^{U'} x_{ij}^u \leq K' - 1 \tag{P3.d}$$

$$x_{cj}^u \in \{0, 1\}, \tag{P3.d}$$

where $\|\mathbf{h}_c - \mathbf{h}_j\|$ is the distance between CHs c and j, $\mathbf{h}_0 = \mathbf{w}_0 = \mathbf{w}_{u,0}$ is the initial and same dockstation for all UAVs, $\mathcal{X} = \{x_{cj}^u \mid c = 1, \ldots, K', \ j = 1, \ldots, K', \ u = 1, \ldots, U'\}$ with x_{cj}^u is a binary indicator of UAV u traveling from CH c to CH j, $x_{cj}^u = 1$ if path is included in UAV u's trajectory, otherwise, $x_{cj}^u = 0$. Also, n_c and n_j are non-negative integers [27]. (P3.a) state that each CH is visited exactly once. (P3.b) are the flow conservation constraints, i.e., when a UAV visits a CH, then it must depart from the same CH. (P3.c) ensures that a UAV is used exactly once, and (P3.d) are the MTZ-based subtour elimination constraints, where degenerate tours not connected to the dockstation are omitted.

Since we assume that the visited locations of the UAVs are directly above the CHs, then a decided UAV location along the trajectory can be written as $\mathbf{w}_u = [x_c, y_c, z_u]$, where the UAV is above CH c, and z_u is the UAV's flying altitude. Using the obtained solution $\mathcal{X}$, $\mathcal{C}_u$ and $\mathcal{W}_u$ can then be deduced.

Brute-force search explores all combinations of routes and it is the most direct solution. However, it is computationally expensive and its complexity is high. The latter is given by

$$\mathcal{O}\left(\sum_{k_1=0}^{K'} \mathbb{C}_{K'}^{k_1}\, k_1! \sum_{k_2=0}^{K'} \cdots \sum_{k_{U'}=0}^{K'} \left(\prod_{c=2}^{U'} \mathbb{C}^{k_c}_{K'-\sum\limits_{j=1}^{U'-1} k_j}\, k_c!\right)\right), \tag{2.10}$$

where $\mathbb{C}_c^j$ is the combination operation. Also, other proposed exact algorithms are time consuming and impractical for small computers and micro-controllers [25]. Nonetheless, approximate and heuristic algorithms are interesting alternatives, especially if resulting routes are near-optimal. Consequently, we adopt in this chapter two approximate trajectory planning approaches, namely the nearest neighbor (NN) and genetic algorithm (GA).

- Using NN algorithm, a UAV starts by selecting the closest CH as its first destination. In the next steps, the closest CH not yet visited will be selected until all CHs are visited by the UAV. NN obtains routes quickly; however, their quality depends on initial locations . Its complexity for our problem is $\mathcal{O}\left((K'+1)^2\right)$.

- Genetic algorithms are introduced to solve combinatorial optimization problems. Several papers have used them to obtain the shortest paths in TSPs [28]. For our problem, the GA pseudo-algorithm is presented in Algorithm 2. GA population is a set of trajectories for all UAVs, i.e., combinations of $\{\mathcal{C}_1, \ldots, \mathcal{C}_{U'}\}$ (and $\{\mathcal{W}_1, \ldots, \mathcal{W}_{U'}\}$). A gene is a CH to be visited. An individual is the U' trajectories satisfying (P3.a)-(P3.d). The parents are combined solutions. The mating pool is a collection of parents to create the next generation. Fitness tells how short the sum of all trajectories is. Mutations introduce variations in the population by randomly swapping CHs in a given trajectory. Finally, elitism carries the best individuals to the next generation. GA's complexity can be given by $\mathcal{O}(\zeta\Upsilon)$, where ζ is the population size and Υ the maximum number of generations. These parameters can be controlled with respect to the solution execution time trade-off, i.e., large (ζ, Υ) gets near-optimal solutions at the expense of longer execution times, versus small (ζ, Υ) for sub-optimal solutions, but in short execution times.

Algorithm 2 GA Pseudo-Algorithm

1: Create population (i.e., combinations of $\{\mathcal{C}_1, \ldots, \mathcal{C}_{U'}\}$)
2: Determine fitness $\sum_{u=1}^{U'} \sum_{i \in \mathcal{C}_u \cup \{0\}} \|\mathbf{w}_{u,c+1} - \mathbf{w}_{u,c}\|$
3: Select mating pool (new combinations of $\{\mathcal{C}_1, \ldots, \mathcal{C}_{U'}\}$)
4: Create next generation using ordered crossover and elitism
5: Use swap mutation to introduce new combinations
6: Repeat steps 1-5 until convergence
7: Return $\{\mathcal{C}_1, \ldots, \mathcal{C}_{U'}\}$ and associated $\{\mathcal{W}_1, \ldots, \mathcal{W}_{U'}\}$

2.4.2.2 UAVs hover within a range of CHs

A UAV can settle for a further location, but close enough to collect data. This can be seen as the CH having an aerial coverage area, in which communication to UAVs is successful. In order to determine the maximum radius of this coverage area for a given UAV altitude, we solve $P_{cu}^{\text{UAV}} = P_c - \Lambda_{cu}$.

Lemma 1. *Given the altitude z of a UAV, the maximum coverage radius of a CH is expressed by*

$$R^*(z) = \frac{z}{\tan\left[f^{-1}\left[P_c - P_{\text{th}} - 20\ \log\left(z\right) - L_{\text{FS}}\left(f_c\right)\right]\right]}, \tag{2.11}$$

where $\tan(.)$ *is the tangent function, and f^{-1} is the inverse function of f defined as*

$$f(\theta) = \frac{\nu_{\text{LoS}} + \nu_{\text{NLoS}}\ a\ e^{-b(\theta-a)}}{1 + a\ e^{-b(\theta-a)}} - 20\log\left(\sin(\theta)\right),\ \theta \in [0, \pi]. \tag{2.12}$$

Proof. For clarity, the designations Λ_{cu}, d_{cu}, θ_{cu} and z_u are simplified into Λ, d, θ and z respectively. Using (2.3)-(2.5), and $d = \frac{z}{\sin(\theta)}$, we obtain after some mathematical manipulations

$$\begin{aligned}
\Lambda &= P_c - P_{\text{th}} \Leftrightarrow \\
20\ \log(z) - 20\ \log(\sin(\theta)) &+ \frac{\nu_{\text{LoS}} + \nu_{\text{NLoS}}\ a\ e^{-b(\theta-a)}}{1 + a\ e^{-b(\theta-a)}} \\
&+ L_{\text{FS}}(f_c) = P_c - P_{\text{th}} \Leftrightarrow \\
\frac{\nu_{\text{LoS}} + \nu_{\text{NLoS}}\ a\ e^{-b(\theta-a)}}{1 + a\ e^{-b(\theta-a)}} &- 20\ \log(\sin(\theta)) = \mathrm{P_c} - \mathrm{P_{th}} \\
&- L_{\text{FS}}(f_c) - 20\ \log(z).
\end{aligned} \tag{2.13}$$

Let the function $f(\theta)$ be the left side of the equality (2.13), hence the value of θ that achieves equality is given by

$$\theta = f^{-1}\left(P_c - P_{\text{th}} - L_{\text{FS}}(f_c) - 20\text{log}(z)\right). \tag{2.14}$$

It is to be noted that due to the complexity of $f(\theta)$, the value θ in (2.14) needs to be determined numerically. Since $\tan(\theta) = \frac{z}{R}$, where R is the coverage radius, (2.11) can be then obtained. $\square$

Now, given the maximum coverage radius of each CH, UAVs can optimize their trajectories by visiting the edges of CHs' coverage areas. This problem is identified as multiple-TSPN (mTSPN). To solve this problem, we propose a modification to the original mTSP solution. Indeed, after obtaining the trajectory among CHs to be visited as previously, we modify the hovering locations by adjusting them as the closest points on the coverage area edges. For instance, we assume that UAV u is at coordinates $\mathbf{w}_u = [x_u, y_u, z_u]$ and that the projection of the next CH to visit on the UAV's plane has coordinates $\bar{\mathbf{w}}_c = [x_c, y_c, z_u]$. The associated CH's coverage perimeter can be expressed by the function

$$(y - y_c)^2 + (x - x_c)^2 = (R^*(z_u))^2. \tag{2.15}$$

Since the UAV flies in the direction of the CH to be visited, then the closest point on the edge of the coverage area is the first intersecting point between the line drawn through locations $\mathbf{w}_u$ and $\bar{\mathbf{w}}_c$ and the coverage perimeter.

Lemma 2. *Let $y = p_1\, x + p_2$ be the line's function, where $p_1 = \frac{y_u - y_c}{x_u - x_c}$ and $p_2 = y_u - p_1\, x_u$. Then, the coordinates of the hovering location $\boldsymbol{w}'_u$ can be given by*

$$\boldsymbol{w}'_u = \begin{cases} \boldsymbol{w}^0_u = [x_0, y_0, z_u], & \text{if } \|\boldsymbol{w}^0_u - \boldsymbol{w}_u\| \leq \|\boldsymbol{w}^1_u - \boldsymbol{w}_u\| \\ \boldsymbol{w}^1_u = [x_1, y_1, z_u], & \text{otherwise} \end{cases} \tag{2.16}$$

where $x_0 = \frac{-q_2 + \sqrt{q_2^2 - q_1\, q_3}}{q_1}$, $x_1 = -\frac{q_2 + \sqrt{q_2^2 - q_1\, q_3}}{q_1}$, $y_0 = p_1\, x_0 + p_2$, $y_1 = p_1\, x_1 + p_2$, $q_1 = {p_1}^2 + 1$, $q_2 = p_1(p_2 - y_c) - x_c$ and $q_3 = x_c^2 - (R^*(z_u))^2$.

Proof. The intersection points between the line drawn through $\mathbf{w}_u$ and $\bar{\mathbf{w}}_c$ and the coverage perimeter satisfy both (2.15) and $y = p_1\, x + p_2$. Hence, by substituting y of the line's equation into (2.15), we get after some manipulations

$$\begin{aligned} & (p_1 x + (p_2 - y_c))^2 + (x - x_c)^2 = (R^*(z_u))^2 \\ \Leftrightarrow\quad & x^2 \underbrace{(p_1^2 + 1)}_{=q_1} + 2x \underbrace{(p_1(p_2 - y_c) - x_c)}_{=q_2} + \underbrace{x_c^2 - (R^*(z_u))^2}_{=q_3} = 0. \end{aligned} \tag{2.17}$$

Thus, (2.17) is a polynomial that can be solved as in (2.16). $\square$

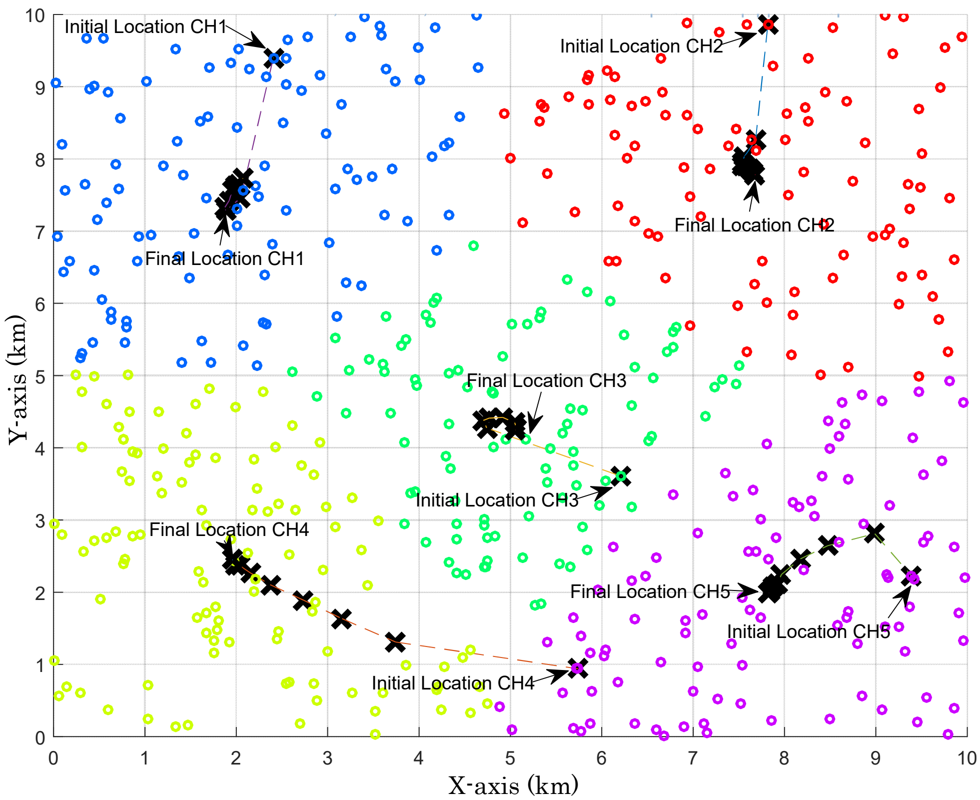

Figure 2.2: Convergence of k-means (10 iterations).

2.5 Simulation Results

We assume an area of 10×10 km^2, populated with $N = 500$ SNs. We fix the following parameters $\gamma_{\text{th}} = 10^{-4}$, $f_c = 2$ GHz, $c = 3.10^8$ m/s, $P_c = 20$ dBm and $P_{\text{th}} = -100$ dBm. Moreover, we assume that $d_s^{\text{th}} \in [100, 2900]$ meters and $\alpha \in [2, 5]$, hence $\frac{P_s}{\sigma^2} = \left(d_s^{\text{th}}\right)^{\alpha} \cdot \gamma_{\text{th}}$. Also, we consider for GA $\zeta = 500$ and $\Upsilon = 1000$. Unless otherwise stated, the flying altitude of UAVs is 200 m and the environment parameters are for the urban one $(a, b) = (9.6117, 0.739)$ [23].

In Fig. 2.2, we show how k-means clustering is processed to find the locations of CHs, such as (P1.b) is satisfied. Given $K' = 5$, the locations of CHs are updated in every iteration until the final locations are obtained. Identically colored SNs (circles) are associated with the CH in their region.

Due to initialization randomness, k-means converges often to sub-optimal solutions. In order to evaluate its influence on our system, we run Algorithm 1 for several times (x100) and for different communication ranges $d_s^{\text{th}} \in [100, 2900]$. The results are plotted

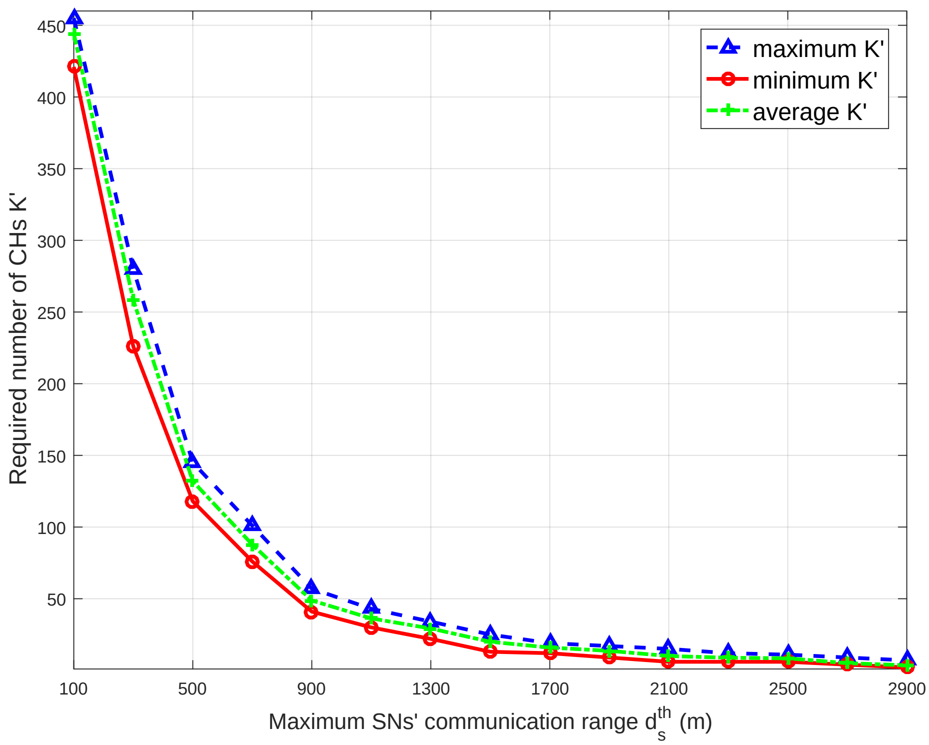

Figure 2.3: Required number of CHs vs. communication range of SNs.

in Fig. 2.3. As shown, with d_s^{th} increasing, a smaller number of CHs is needed. However, for $d_s^{\mathrm{th}} < 1000$ m, it is critical to have a very large number of CHs in order to guarantee communications to all SNs. Also, for a given d_s^{th}, K' can be different depending on the obtained locations of CHs. For instance, K' has to be between 22-34 CHs for $d_s^{\mathrm{th}} = 1700$m, to associate all SNs with CHs. In general, d_s^{th} is based on the type of the sensors and their capability, which will impact the required number of CHs, and consequently affect the deployment costs. Given the SNs capabilities in terms of the communication ranges, the green curve in Fig. 2.3 indicates the average required number of CHs.

Given $U' = 1$, we compare in Fig. 2.4 the performances of the optimal solution (obtained using Matlab solver), proposed GA algorithm, and NN algorithm, in terms of the UAV's traveled distance, versus the number of CHs to visit. We assume here that the UAV hovers exactly above each CH. As K' grows, distance traveled increases for all approaches. This is expected since visiting more CHs inevitably implies traveling longer distances. Moreover, Matlab solver achieves the shortest traveled distance, while GA follows closely with only 0% to 3.5% degradation. NN approach presents the worst performance with a degradation with K' up to 12%. Since GA achieves near-optimal performances, it will be used in the following simulations.

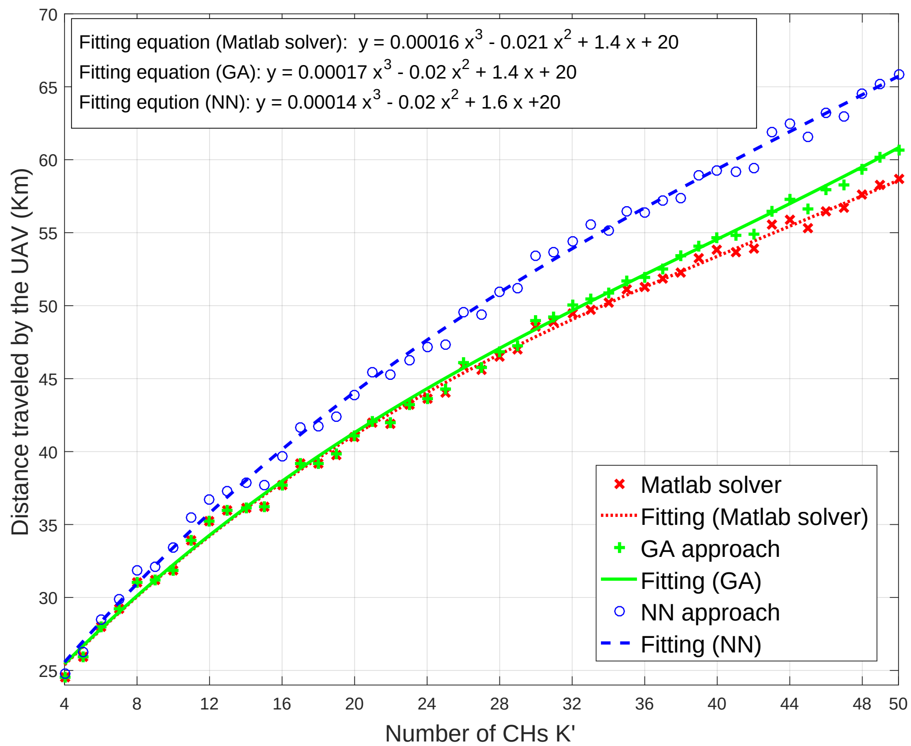

Figure 2.4: Distance traveled by the UAV vs. number of CHs.

In Fig. 2.5, we compare the distances traveled by UAVs when the latter hover either exactly above (TSP), or within a range of 1 km from each CH (TSPN). Let d_{TSP} and d_{TSPN} be the associated UAV's trajectory lengths respectively. As illustrated, TSPN achieves a shorter distance trajectory, while guaranteeing data collection from all 10 CHs. The traveled distance gain, defined by $\rho = 1 - \frac{d_{\text{TSPN}}}{d_{\text{TSP}}}$, can be calculated as $\rho = 15.27\%$ in this scenario. That means, hovering within a distance of each CH is advantageous in shortening the distance traveled, and thus the data collection mission time.

In Fig. 2.6, we illustrate the relation between the UAV altitude z and the traveled distance gain ρ for different environment types. The scenario has 20 CHs, and the environment parameters (a, b), as defined in (2.4), are given within the figure. Moreover, (2.11) and (2.16) are used to calculate the maximum coverage radius and the TSPN trajectory, respectively. As z increases, ρ increases at first until reaching a maximum value. The latter corresponds to the optimal UAV altitude, where CH-UAV communications satisfy the required P_{th}. Beyond it, ρ degrades rapidly as z increases. Indeed, a higher altitude degrades the CH-UAV communication link. The intersection point between any curve and the X-axis presents the maximum altitude at which the UAV needs to hover exactly above the CH to collect data ($\rho = 0$). Above it, transmissions would fail. Also, the traveled

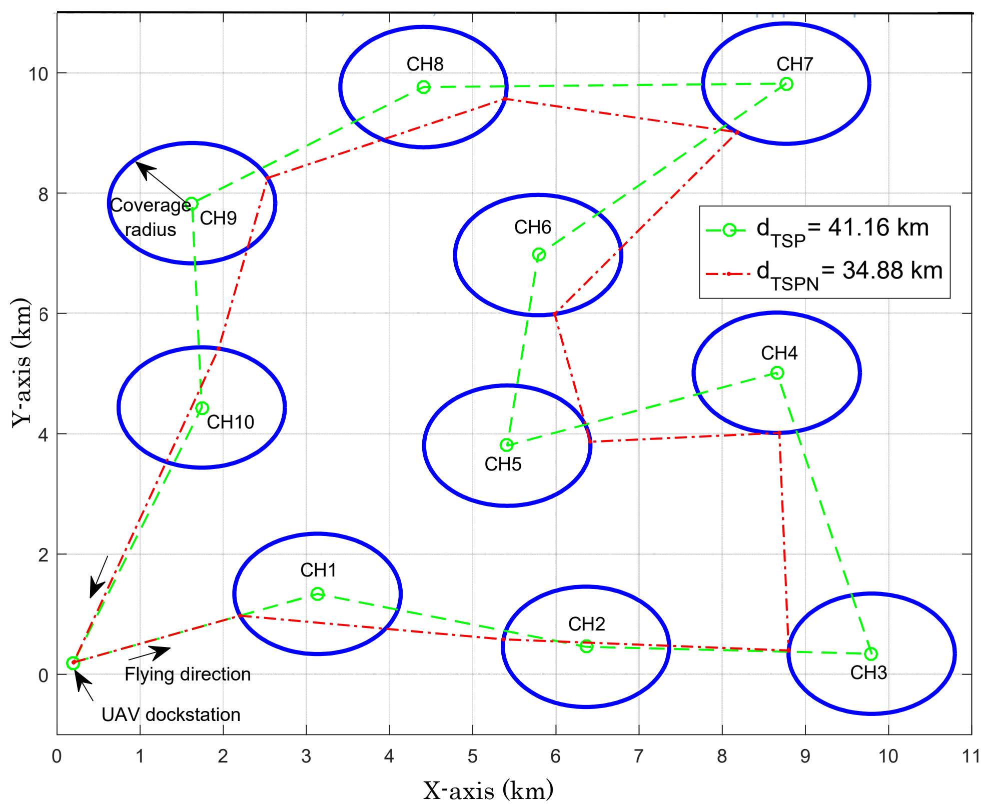

Figure 2.5: Trajectories of UAVs.

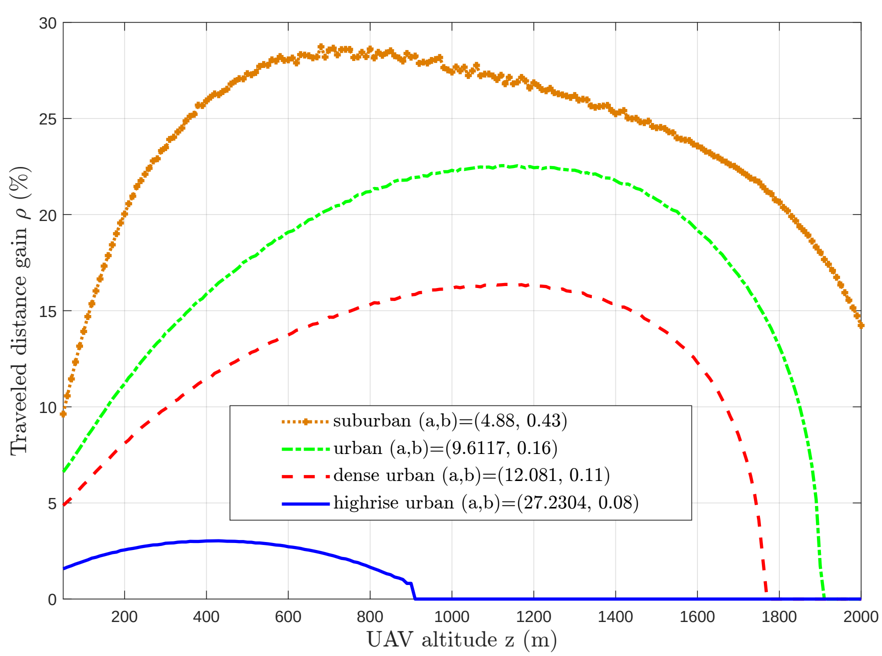

Figure 2.6: Average traveled distance gain vs. UAV altitude.

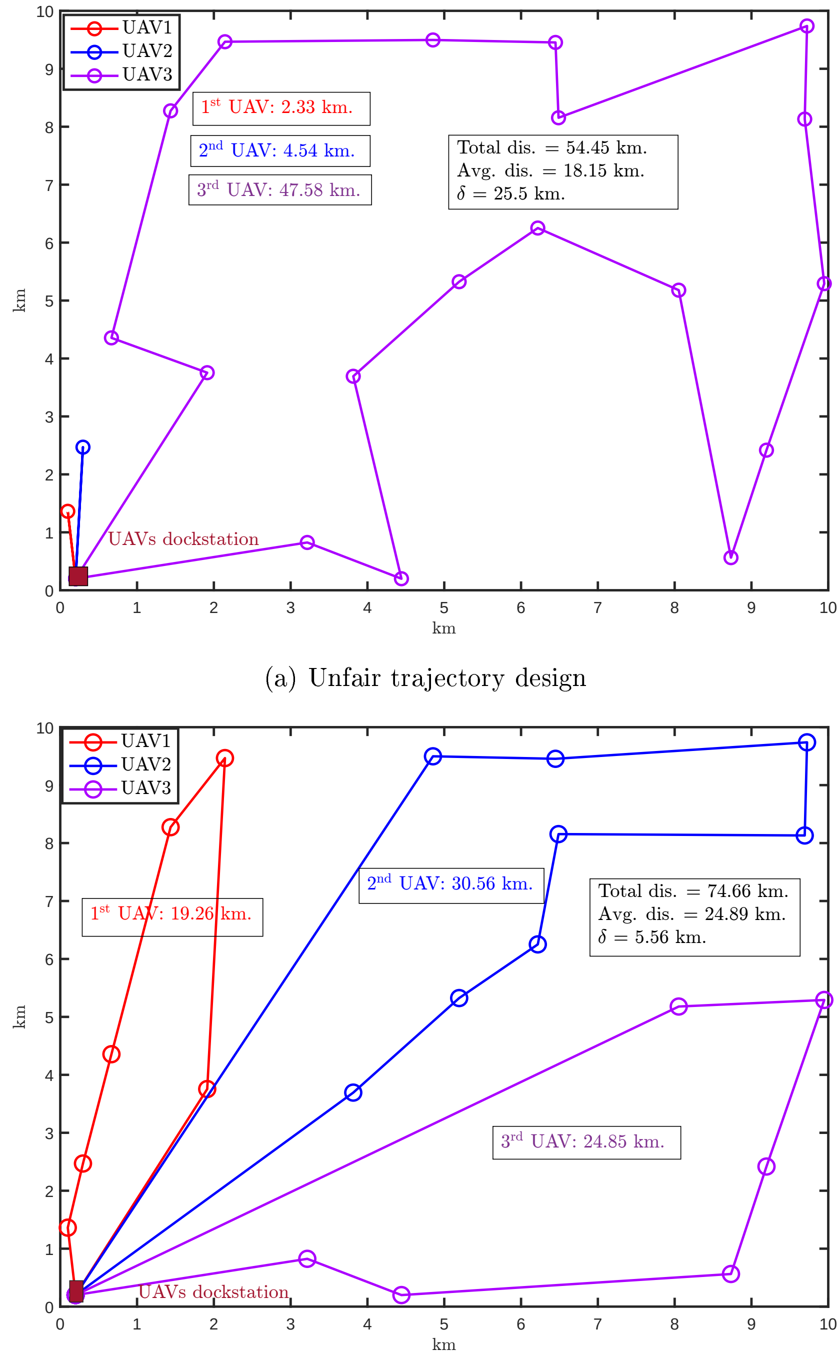

(a) Unfair trajectory design

(b) Fair trajectory design

Figure 2.7: An example of unfair and fair trajectory optimizations with 3 UAVs and 20 CHs.

distance gain ρ is more significant as the environment becomes less urbanized. Indeed, with better LoS links, communications are tolerated on wider coverage areas. Thus, better ρ is acheived.

For the multi-UAV trajectory optimization, considering solely the minimization of the total traveled distance/time for all UAVs may result in unfair trajectory planing. Thus, some UAVs will be assigned much more CHs for data collection, and their traveled distance will be significantly larger than others. Therefore, a practical and cost-effective trajectory design should ensure both fair trajectory planing and minimum total traveled distance. In order to leverage fairness among multi-UAV trajectories, we propose to utilize the the standard deviation for traveled distances by all UAV as a fairness metric. Accordingly, we limit the standard deviation by a threshold $\delta_{\mathrm{th}} = 10$ km for fair trajectory selection in the GA algorithm. An example of both fair and unfair optimized trajectory planing is shown in Fig. 2.7 with their associated distances. Although Fig. 2.7(a) has lower total average distance than Fig. 2.7(b), the trajectory design might not be a feasible solution, since most of data collection tasks are conducted by one of the deployed UAVs.

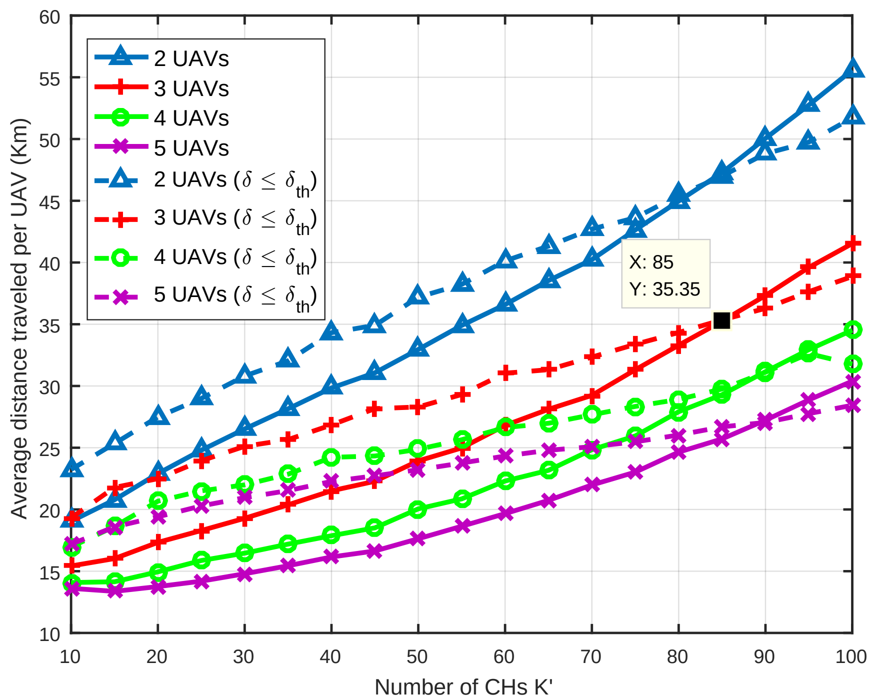

Figure 2.8: Average distance traveled per UAV vs. number of CHs.

In Figs. 2.8-2.9, we investigate the performance of the multi-UAV system in terms of average distance traveled per UAV versus the number of CHs K', and we compare the associated standard deviation of the trajectories (δ). As shown in Fig. 2.8, the average distance traveled increases with K'. Moreover, as the number of UAVs U' grows, the average distance traveled decreases significantly at first, then slowly. This means that adding a UAV to a system using initially a small number of UAVs is more beneficial than

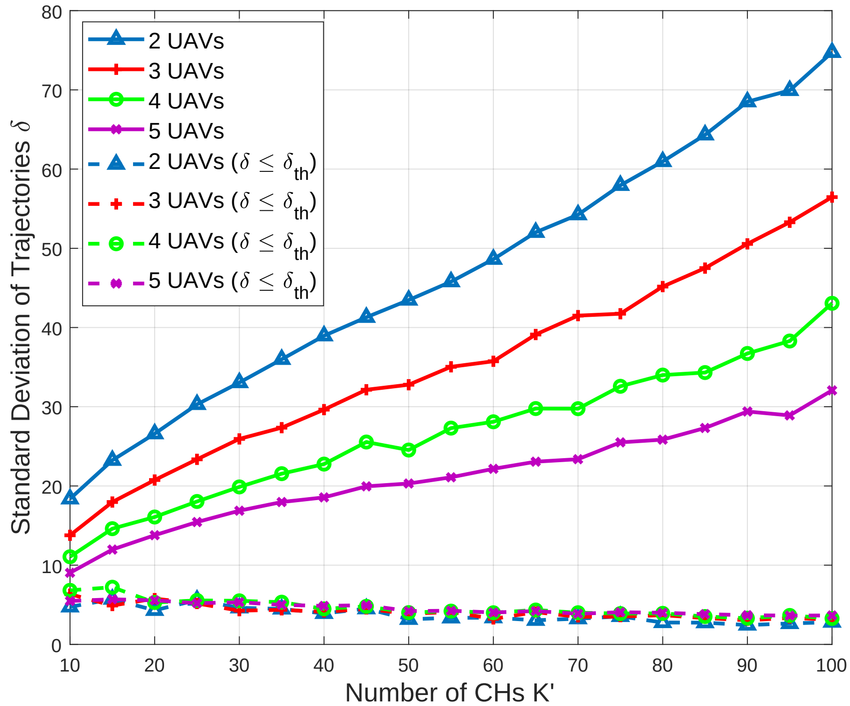

Figure 2.9: Standard deviation of trajectories vs. number of CHs.

to a system using already a large number of UAVs. We notice in Fig. 2.9 that the standard deviation (solid lines) decreases when U' increases, i.e., a system with a higher number of UAVs would achieve fairer trajectories among UAVs.

Nevertheless, UAVs are usually constrained by their flight time (alternatively, their flight distance), consequently, an optimal but unfair (in terms of trajectory lengths) solution may not be adequate. Given the fairness limit $\delta_{\text{th}} = 10$, the performance of fair trajectories are illustrated in Figs. 2.8-2.9 by the dashed lines. According to Fig. 2.8, average traveled distance for $\delta \leq \delta_{\text{th}}$ (fair) is higher than in the first case (solid lines), for K' lower than a certain value (e.g., $K' = 85$ for 3 UAVs). However, above it, the fair solution outperforms the first one. Indeed, since GA's parameters (ζ, Υ) are fixed and K' is increasing, Algorithm 2 can only provide sub-optimal solutions. Meanwhile, the condition $\delta \leq \delta_{\text{th}}$ allows exploring other solutions that turn out to be more efficient. In Fig. 2.9, we validate $\delta \leq \delta_{\text{th}}$ in all scenarios (dashed lines).

2.6 Conclusion

In this chapter, we proposed a framework for UAV-based WSNs, which aimed to collect data in the shortest time frame and at the lowest cost, in terms of deployed cluster heads and UAVs. Specifically, we used clustering to optimize the number and locations of cluster heads. Then, we leveraged heuristic solutions to mTSP and TSPN to obtain optimized number and trajectories of UAVs. Simulation results provide guidelines for data collection design in WSNs: the selection of the number of CHs and their clustering has to be carefully processed. The heuristic GA used to deploy and plan trajectories of UAVs was shown to be near-optimal with only 3.5% degradation. Data collection times can be minimized by hovering within a range of visited CHs. Also, the data collection time is affected by the environment and flight altitude. Finally, the integration of trajectory fairness is beneficial in large WSNs. In the following chapter, we will improve the data collection framework for a heterogeneous IoT network with different priorities and time deadlines while taking into account the limited onboard energy of the UAVs.

Chapter 3

Energy-Efficient Multi-UAV Data Collection for IoT Networks with Time Deadlines

3.1 Introduction

The vision of future wireless technologies with numerous smart applications and services has emerged with the Internet of Things (IoT), connecting millions of devices and people. IoT sensor networks are a key enabler for novel applications, including smart cities, connected cars, smart grids, and intelligent transportation. Indeed, the Third Generation Partnership Project (3GPP) has issued recently several standardization documents to support IoT in 5G systems (e.g., TR 23.700-20 and TR 23.700-24). Typically, IoT sensors are low-cost and limited-energy devices with short transmission ranges. In large-scale IoT systems, the deployment of super-sensors or cluster heads (CHs) to aggregate data from neighboring sensors is a practical solution to reduce communication overhead and save sensors' energy. However, even CHs may have a limited communication range, and therefore, a large number of CHs/relay nodes are needed to expand the network connectivity.

This work mainly has been published in IEEE Globecom 2020 proceedings: O. Ghdiri, W. Jaafar, **S. Alfattani**, J. Ben Abderrazak and H. Yanikomeroglu, "Energy-Efficient Multi-UAV Data Collection for IoT Networks with Time Deadlines", *IEEE Global Communications Conference* (Globecom), Taipei, Taiwan, Dec. 2020, pp. 1-6.

To tackle this issue given the lifetime constrains of the relay nodes/CHs, a deployment strategy is proposed in [29]. In this strategy, the minimum number of relay nodes is determined. Then, the placements of relay nodes/CH are optimized to maximize the network connectivity within the lifetime constraint.

However, relaying only on a static relay nodes or always maintaining the connection between CHs and the network center might not be feasible in certain environments even with optimized deployment strategy of CHs. Therefore, a mobile data collector needs to be deployed to gather sensed data and sends it to the control center. In that matter, UAVs can be deployed as data collectors [30], as discussed in the previous chapter. Indeed, UAVs have been presented as an efficient tool to solve several wireless communication challenges [15]. Accordingly, recent 3GPP standards were issued to regulate different aspects of UAV support in 5G (TR 22.829 and TS 22.125). Due to the agility, strong Line-of-Sight (LoS), and fast deployment of UAVs, the latter are a relevant option for data collection in IoT systems [30]. Nevertheless, UAVs have a limited onboard energy and are sensitive to blockages. Hence, accurate communication channel and power consumption models should be considered when designing data collection missions. On the other hand, large-scale IoT networks practically encompass sensors with different priorities, criticality levels, and time-sensitive usefulness. Consequently, energy-efficient data collection needs an accurate UAV deployment and trajectory planning to meet time-sensitive constraints, e.g., time deadlines for data collection.

Several works proposed UAV-based sensors' data collection. In our previous work [30], presented in the previous chapter, we proposed collecting data from a clustered wireless sensor network using one or several UAVs, aiming to minimize the mission costs in terms of number of clusters and traveled distance by UAVs, while guaranteeing data is collected from all clusters. In this setting, sensor nodes (SNs) were clustered using a k-means-based algorithm, and UAV trajectories designed with different approaches, including genetic algorithm and nearest-neighbor. In [31], the problem of minimizing data collecting time from IoT time-constrained sensors is investigated, where the trajectory of a single collecting UAV and radio resource allocation are optimized. Moreover, the authors of [32] proposed joint optimization of wakeup schedule of SNs and a single UAV's trajectory to minimize the total consumed energy by SNs, while guaranteeing complete data collection from all of them. Finally, authors in [33] presented a data collection framework, where multiple UAVs are deployed to collect data from clustered SNs, aiming to minimize the number of deployed UAVs and their flight times and distances, with respect to a mission deadline.

The optimal solution is obtained, which outperforms a benchmark greedy approach. Nevertheless, these works have several limitations. Authors in [30, 31] did not consider energy restrictions of UAVs, while [32] focused only on single UAV trajectory planning. Finally, [33] did not account for energy limitations and air-to-ground accurate channel modeling.

Motivated by the aforementioned points, we propose in this chapter a practical data collection approach for large-scale IoT systems, where multiple UAVs collect sensed data with different time deadlines. The proposed solution follows a two-step approach. First, the minimum number of CHs and their locations are determined to guarantee that data from all SNs is aggregated at the CHs. Then, the number of collecting UAVs and their trajectories are optimized to minimize the total consumed energy. Finally, the impact of key parameters, e.g., UAV's battery capacity and data time deadlines, is investigated.

3.2 System Model

In this section, we present, the network and channel models, the data collection model and the UAV energy model.

3.2.1 Network and Channel Models

Following the system model presented in the previous Chapter, we consider an IoT sensor network consisting of a set $\mathcal{N} = \{1, \ldots, N\}$ of SNs, uniformly randomly located in a large area and constantly collecting time-sensitive data. In addition, we assume that SNs are heterogeneous, i.e., sensed data by SNs are of different kind, having different importance in time. Indeed, some sensed data are more critical and need to be collected faster than other less-critical data. Due to the limited energy and communication capability of typical IoT sensors, we assume that a set of $\mathcal{K} = \{1, \ldots, K\}$ cluster heads (CHs) can be deployed to collect, aggregate, and transmit sensed data to the data collector. The data collection tasks are operated by multiple UAVs, which fly and hover above/close to CHs for a sufficient time to collect the aggregated data. Fig. 3.1 illustrate the important aspects of the considered system model.

For modeling the communications between SNs and CHs, we adopt the same models described by equations (2.1)–(2.2). Similarly, for the channel model between CHs and UAVs, we utilized the same probabilistic channel model presented in the previous Chapter,

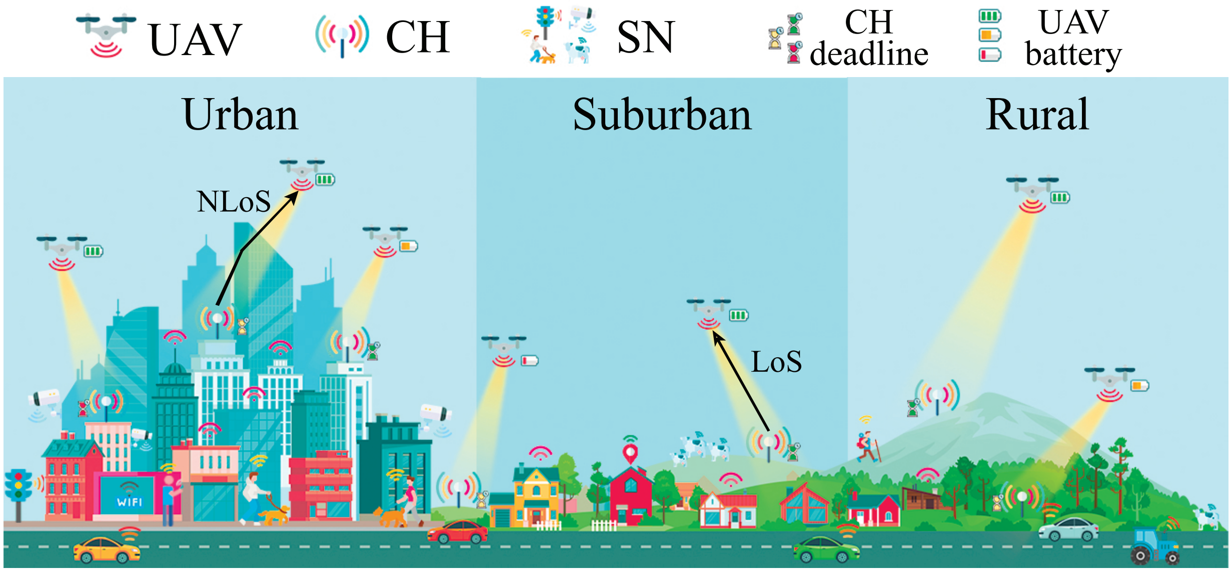

Figure 3.1: System model of UAV-based data collection in clustered IoT networks with time deadlines.

which is applicable to different environments. The communication model is described by equations (2.3)–(2.6).

3.2.2 UAV Data Collection Model

We assume that the mission time, i.e., the maximum time for UAVs to collect data from CHs and return to their dockstation, is T_F and divided into M time slots (TSs). Thus, TSs are equal and are of length $\delta = \frac{T_F}{M}$. We define the 3D location of UAV u in time slot t as $\mathbf{q}_u^t = [x_u^t, y_u^t, H]$. Since the UAV's speed is limited by $v_{\max}$, its traveled distance in one TS is constrained by

$$||\mathbf{q}_u^{t+1} - \mathbf{q}_u^t|| = \sqrt{(x_u^{t+1} - x_u^t)^2 + (y_u^{t+1} - y_u^t)^2} \leq v_{\max}\delta. \tag{3.1}$$

In our system, each CH c uploads its data to its associated UAV u at rate R_{cu} in bits/second (bps), determined using the Shannon equation as follows:

$$R_{cu} \leq W \log_2(1 + \gamma_{cu}), \ \forall c \in \mathcal{K}_u, \ \forall u \in \mathcal{U}, \tag{3.2}$$

where W is the total bandwidth of the channel and $\gamma_{cu} = \frac{\bar{P}_{cu}}{\sigma^2}$ is the SNR, where $\bar{P}_{cu} = 10^{\frac{P_{cu}}{10}}$ is the linear value of P_{cu}. Accordingly, the required number of TSs to upload one packet to the UAV can be expressed by

$$T_{1,cu} \approx \left\lceil \frac{S_p}{R_{cu}\delta} \right\rceil, \ \forall c \in \mathcal{K}_u, \ \forall u \in \mathcal{U}, \tag{3.3}$$

where S_p is the size of the packet in bits and $\lceil \cdot \rceil$ is the ceiling function. Given Q_c data packets to be transmitted by CH c, then the required data collection time (in TSs) by UAV u is

$$T_{cu} = Q_c T_{1,cu} \ \forall c \in \mathcal{K}_u, \ \forall u \in \mathcal{U}. \tag{3.4}$$

Due to the different priorities of collected data at each CH, we define by $T_{d,c}$ the time deadline of data stored in CH c, i.e., if not totally collected within this deadline, the data in the CH becomes outdated and it is dropped. Hence, data collection has to respect the following constraint, assuming that all packets in one CH are collected by only one UAV

$$\sum_{m=1}^{\phi_u(c)} \left[T_{mu} + T_{f,u}(m-1,m)\right] \leq T_{d,c}, \ \forall c \in \mathcal{K}_u, \tag{3.5}$$

where $\phi_u(c)$ designates the rank (i.e. index) of CH c in $\mathcal{K}_u$, T_{mu} is the data collection time of CH ranked m in $\mathcal{K}_u$, and $T_{f,u}(m-1,m)$ is the flight time (in TSs) from the hovering location to collect data from CH ranked $(m-1)$ to that associated to the CH ranked m in $\mathcal{K}_u$, with $m = 0$ designating the dockstation. The flight time of UAV u between two locations $\mathbf{q}_{u,i}$ and $\mathbf{q}_{u,i'}$, where i and i' are two CHs ranks in the UAV path, can be calculated as follows:

$$T_{f,u}(i,i') = \frac{||\mathbf{q}_{u,i'} - \mathbf{q}_{u,i}||}{v_u \ \delta}, \tag{3.6}$$

with $v_u \leq v_{\max}$ is the flying speed of the UAV (in m/sec).

3.2.3 UAV Energy Model

The UAV is energy-constrained due to limited onboard battery. The battery lifetime depends on several factors, e.g., UAV's energy source, type, weight, speed, etc. Typically, the UAV's energy consumption consists of the propulsion energy and the communication energy. Without loss of generality, communication energy is several orders of magnitude smaller than propulsion energy. Hence, it is neglected in the considered energy model. For the propulsion energy, we adopt the propulsion-power model for rotary-wing UAVs in [19]

$$\begin{aligned} P_{\text{prop,u}}(v_u) = {} & \zeta_I \left(\sqrt{1 + \frac{v_u^4}{4v_0^4}} - \frac{v_u^2}{2v_0^2} \right)^{1/2} \\ & + \zeta_B \left(1 + \frac{3v_u^2}{U_{\text{tip}}^2}\right) + \frac{1}{2} d_0 \psi r A v_u^3, \end{aligned} \tag{3.7}$$

where ζ_B and ζ_I are the blade profile power and induced power, respectively. U_{tip} is the tip speed of the rotor blade, v_0 is the mean rotor induced velocity, ψ is the air density, d_0 is the fuselage drag ratio, r is the rotor solidity, and A denotes the rotor disc area. In order to obtain the power consumption for hovering, we use the same equation above, but with null flying speed $v_u = 0$, thus, we get

$$P_{\text{hov,u}} = P_{\text{prop,u}}(v_u = 0) = \zeta_B + \zeta_I. \tag{3.8}$$

Using (3.7)–(3.8), the consumed energy of UAV u during a time period T can be given by

$$E_u(v, T) = \begin{cases} P_{\text{prop,u}}(v) \times T, & \text{if } v > 0 \\ P_{\text{hov,u}} \times T, & \text{if } v = 0. \end{cases} \tag{3.9}$$

Hence, the related battery status at TS t, denoted $S_u(t)$, can be expressed by

$$S_u(t) = S_u(t-1) - E_u(v, \delta),\ \forall t > 1, \tag{3.10}$$

where $S_u(t-1)$ is the battery's status at the end of TS $(t-1)$, and $S_u(0)$ is the initial battery capacity. The latter is expressed as $S_u(0) = S_{\text{ini}} + S_{\min}$, where S_{ini} is the battery capacity dedicated for the mission, while $S_{\min}$ is a safety capacity, reserved for emergency pull back to the dockstation. Hence, $S_u(t) \in [S_{\min}, S_u(0)]$.

3.3 Problem Formulation

In this section, we formulate our optimization problem aiming to minimize the total consumed energy for data collection, by optimizing the deployment of CHs, the number of required UAVs, and their trajectories. Let $K_u = |\mathcal{K}_u|$ be the cardinality of the set $\mathcal{K}_u$, $\forall u \in \mathcal{U}$. Then, using (3.9), the consumed energy by UAV u during the mission is given by

$$E_u(\mathcal{K}_u) = \sum_{m=1}^{K_u+1} \left[E_u(0, T_{mu}\ \delta) + E_u(v_u, T_{f,u}(m-1, m)\ \delta) \right], \tag{3.11}$$

where $T_{f,u}(K_u, K_u+1) = \|\mathbf{q}_{u,K_u} - \mathbf{q}^0\|/v_u\delta$, and $\mathbf{q}^0$ is the initial location of all UAVs, i.e., the dockstation. Therefore, the optimization problem can be formulated as follows:

$$\begin{aligned}
&\min_{\substack{\mathcal{K},\mathcal{L},\{\mathcal{A}_c\}_{c\in\mathcal{K}}\\ \mathcal{U},\{\mathcal{K}_u,\mathcal{L}_u\}_{u\in\mathcal{U}}}} \quad \sum_{u=1}^{U} E_u(\mathcal{K}_u) && \text{(P1)}\\
&\text{s.t.}\quad d_{sc} \leq d_{\text{th}},\ \forall s \in \mathcal{A}_c, \forall c \in \mathcal{K}, && \text{(P1.a)}\\
&\qquad S_u(t) \geq S_{\min},\ \forall u \in \mathcal{U}, \forall 1 \leq t \leq T_u,\ \forall u \in \mathcal{U} && \text{(P1.b)}\\
&\qquad \sum_{m=0}^{\phi_u(c)} \left(T_{mu} + T_{f,u}(m-1,m)\right) \leq T_{d,c}, && \text{(P1.c)}\\
&\qquad \|\mathbf{q}_u^t - \mathbf{q}_{u'}^t\| \geq d_{\text{safe}}, \forall t \geq 1, \forall (u,u') \in \mathcal{U}^2,\ u \neq u' && \text{(P1.d)}\\
&\qquad \|\mathbf{q}_u^{t+1} - \mathbf{q}_u^t\| \leq v_{max}\delta,\ \forall 1 \leq t \leq T_u,\ \forall u \in \mathcal{U}, && \text{(P1.e)}
\end{aligned}$$

where $T_u \leq N$ is the effective mission completion time for UAV u (in TSs), $\mathcal{L} = \{\mathbf{q}_c\}_{c\in\mathcal{K}}$ is the set of selected locations for CHs, and $\mathcal{L}_u = \{\mathbf{q}_{u,i}\}_{i\in\mathcal{K}_u}$ is the set of ordered UAV hovering locations to collect data from its associated CHs.

The objective function is to minimize the total consumed energy by all UAVs, given their trajectories $\mathcal{L}_u$ associated to their sets of CHs $\mathcal{K}_u$. (P1.a) ensures the successful communication between SNs in $\mathcal{A}_c$ and their associated CH c. (P1.b) guarantees that enough energy is available in the battery to complete the mission at any TS t, while (P1.c) satisfies the time deadline condition when a UAV collects data from CHs. Also, (P1.d) imposes a safety distance (d_{safe}) between UAVs to ensures no collisions occur, and finally, (P1.e) limits the flying distance, for a given $v_{\max}$.

Problem (P1) is NP-hard. Indeed, in the special case of already deployed CHs, the problem becomes finding the best routes for UAVs, while respecting the energy and time deadlines conditions. The latter can be seen as the capacitated vehicle routing problem with time windows (CVRPTW) [34]. The CVRPTW can be described as selecting the routes for a number of vehicles, aiming to serve a group of customers within time windows. Each vehicle has a limited capacity, which is used to depart from a depot point, serve a number of customers along its route, then return to the same depot point. The objective of the CVRPTW is to minimize the total transport costs. Logically, the vehicles, customers, and transport costs, can be assimilated by the UAVs, CHs, and energy consumption, respectively. Since the CVRPTW is known to be NP-hard [34], then by restriction, (P1) is NP-hard.

3.4 Solution Approach

In (P1), we notice that the optimization of parameters $\mathcal{U}$ and $\{\mathcal{K}_u, \mathcal{L}_u\}_{u\in\mathcal{U}}$ directly depends on the selected parameters $\mathcal{K}, \{\mathcal{A}_c\}_{c\in\mathcal{K}}$ and $\mathcal{L}$. Moreover, since their associated constraints are independent, problem (P1) can be divided into two cascaded problems as follows:

1. First, a problem of sensors clustering and CHs placement, where only $\mathcal{K}$, $\mathcal{L}$, and $\{\mathcal{A}_c\}_{c\in\mathcal{K}}$ are optimized, aiming to minimize the number of deployed CHs is formulated.[1]

2. Then, given $\mathcal{K}$, $\mathcal{L}$ and $\{\mathcal{A}_c\}_{c\in\mathcal{K}}$, a second problem of UAV trajectory planning is formulated in order to minimize the total consumed energy, through the optimization of $\mathcal{U}$ and $\{\mathcal{K}_u, \mathcal{L}_u\}_{u\in\mathcal{U}}$.

Hence, we present next the two described problems and propose efficient approaches to solve them.

3.4.1 IoT Sensors Clustering

As previously discussed, clustering and deployment of CHs is an energy-efficient way for large IoT sensors network. It will facilitate the scalability of the network and save the energy of sensor nodes. Several state-of-the-art clustering techniques exist, e.g., k-means [24], density-based spatial clustering, and hierarchical cluster analysis (HCA) [35]. In Chapter 2, Algorithm 1 based on k-means clustering was proposed to obtain minimal deployment of CHs. Here, we introduce an improvement for Algorithm 1. The associated

[1] This objective has a direct impact on the consumed energy of data collection since a lower number of CHs would reduce the mission time and energy consumption of UAVs.

clustering problem can be written as

$$\min_{\substack{\mathcal{K},\mathcal{L},\\ \{\mathcal{A}_c\}_{c\in\mathcal{K}}}} \quad \sum_{c=1}^{K}\sum_{s=1}^{M} a_{sc}\, d_{sc}^2 \tag{P2}$$

$$\text{s.t.} \quad d_{sc} \leq d_{\text{th}}, \forall s \in \mathcal{A}_c, \forall c \in \mathcal{K} \tag{P2.a}$$

$$|\mathcal{A}_c| \leq F, \quad \forall c \in \mathcal{K}, \tag{P2.b}$$

where $a_{sc} \in \{0, 1\}$ is a binary variable indicating whether SN s is associated with CH c or not, $\forall s \in \mathcal{A}_c$. Constraint (P2.b) guarantees fairness in associating SNs with CHs, where F is the maximum number of SNs associated with one CH. Finally, $|\mathcal{A}_c|$ is the cardinality of the set $\mathcal{A}_c$.

Conventionally, k-means clustering requires a predefined number of CHs. Hence, in [30], Algorithm 1 solves (P2) without any constraint, then re-executed it iteratively until (P2.a) is met. Such method is time consuming and inaccurate, as the clustering performance may vary with the algorithm initialization. Therefore, an improvement to Algorithm 1 is introduced here, by integrating both constraints (P2.a)–(P2.b) into the clustering process. The proposed approach is presented in Algorithm 3, and described as follows. First, locations of $K = N/F$ CHs are randomly initialized. Then, each SN is assigned to the closest CH with respect to (P2.a)–(P2.b). Next, the locations of CHs are updated by calculating the resulting mean location of associated SNs for each CH. This procedure is repeated until convergence, i.e., the calculated locations remain unchanged. Since we aim to deploy the minimal number of CHs, we execute the aforementioned steps for an increasing number of CHs until a solution to (P2) is obtained, i.e., optimal K is determined.

Although the calculated CHs locations are an adequate solution for (P2), this may not be the case for the main problem (P1). In this context, we propose further improvement to the locations of CHs by making them closer to the dockstation. Indeed, CH c has a mobility margin if its furthest associated SN, denoted s_0, respects (P2.a) loosely, i.e., $d_{s_0c} < d_{\text{th}}$. Hence, making the CHs closer to the dockstation would increase the probability to respect data collection deadlines, shorten the mission time, and improve the energy consumption of UAVs. This procedure is in lines 32-34 of Algorithm 3.

3.4.2 Multi-UAV Trajectory Planning

Given $\mathcal{K}$, $\mathcal{L}$, and $\mathcal{A}_c$, $\forall c \in \mathcal{K}$, the trajectory planning problem can be formulated as

$$\begin{aligned} \min_{\mathcal{U}, \{\mathcal{L}_u, \mathcal{K}_u\}_{u \in \mathcal{U}}} \quad & \sum_{u=1}^{U} E_u(\mathcal{K}_u) \\ \text{s.t.} \quad & \text{(P1.b)} - \text{(P1.e)}. \end{aligned} \tag{P3}$$

As discussed previously, this problem is NP-hard, and can be assimilated to a CVRPTW problem. In order to solve it, we model our system as a graph, described as follows. Let $G = (\mathcal{D}, \mathcal{E})$ be a complete graph, where $\mathcal{D} = \{0, 1, \ldots, K\}$ is a set of vertices (nodes) representing the dockstation (node 0) and K CHs, and $\mathcal{E}$ is the set of directed edges connecting the nodes. A directed edge from node i to node j, denoted e_{ij}, represents the UAV's flying operation from i to j and the hovering operation at j. A cost associated to the edge e_{ij}, called $\chi_u(e_{ij}) = E_u(v_u, \mu_1(e_{ij})) + E_u(0, \mu_2(e_{ij}))$, is expressed as the sum of the UAV's flying and hovering energy, where $\mu_1(e_{ij}) = T_{f,u}(i,j)\delta$ and $\mu_2(e_{ij}) = T_{ju}\delta$ respectively, $\forall u \in \mathcal{U}$.[2] Moreover, the time deadlines at CHs are represented in the graph by a time window $\omega_c = [o_c, v_c]$, where o_c and v_c are the minimum and maximum instants for data collection, for each node $c \in \mathcal{D}$. This time window defines when data collection at node c can begin and end. Finally, trajectory of UAV u in $\mathcal{G}$ can be defined by $\mathcal{K}_u$, where each element of $\mathcal{K}_u$ is the ordered node to visit. Accordingly, (P3) can be reformulated as problem (P4) detailed below:

$$\min_{\substack{\mathcal{U}, \{\mathcal{K}_u, \\ \mathcal{L}_u\}_{u \in \mathcal{U}}}} \quad \sum_{u \in \mathcal{U}} \sum_{i \in \mathcal{D}} \sum_{j \in \mathcal{D}} \chi_u(e_{ij})\, b_{u,ij} \tag{P4}$$

$$\text{s.t.} \quad \sum_{u=1}^{U} \sum_{i \in \mathcal{D}} b_{u,ij} \leq 1, \quad \forall j \in \mathcal{D} \tag{P4.a}$$

$$\sum_{j \in \mathcal{D}} b_{u,0j} = \sum_{i \in \mathcal{D}} b_{u,i0} = 1, \quad \forall u \in \mathcal{U} \tag{P4.b}$$

$$\sum_{i=1}^{j-1} \mu_1(e_{i(i+1)}) + \mu_2(e_{i(i+1)}) \in [o_c, v_c],\ \forall j \in \mathcal{K}_u \tag{P4.c}$$

$$\sum_{i \in \mathcal{D}} \sum_{j \in \mathcal{D}} \chi_u(e_{ij}) b_{u,ij} \leq S_u(0) - S_{\min},\ \forall u \in \mathcal{U}, \tag{P4.d}$$

[2]This is valid assuming that all UAVs are of the same type, i.e., having the same mechanical and communication characteristics.

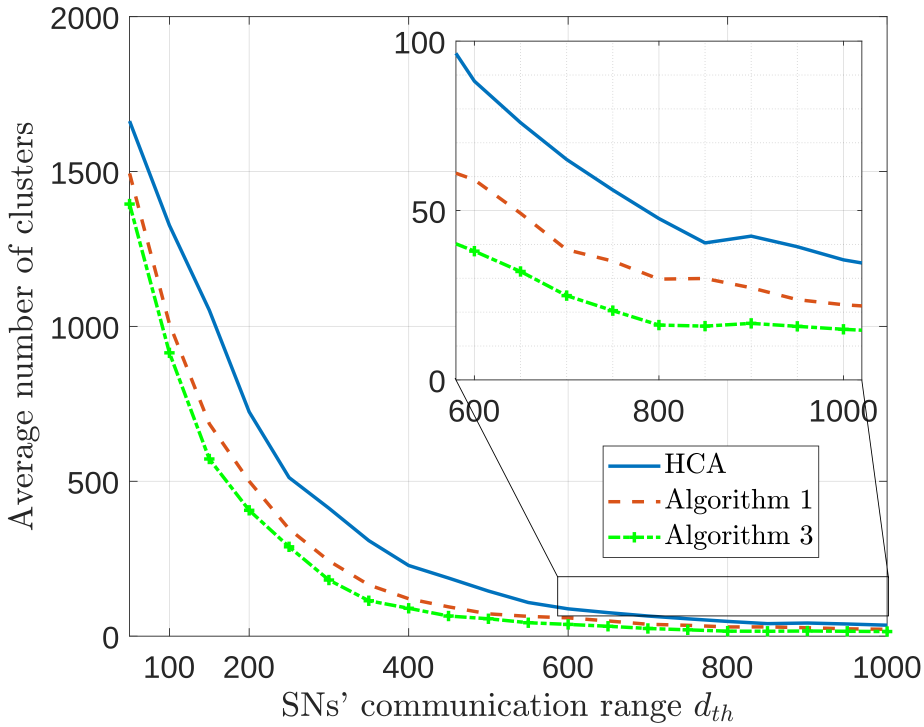

Figure 3.2: Average number of CH vs. d_{th}.

where $b_{u,ij}$ is the binary variable indicating the selection of the edge $i-j$ within UAV u's trajectory. Constraint (P4.a) ensures that each CH is visited at most once by exactly one UAV. (P4.b) guarantees that each UAV departs and returns to the dockstation. Condition (P4.c) emphasizes that the data collection time cannot exceed the time deadline. Finally, (P4.d) guarantees that the consumed energy by any UAV respects the battery capacity. Subsequently, problem (P4) can be solved using any of the available CVRPTW heuristic or metaheuristic approaches, such as gradient descent, simulated annealing, Tabu search, etc. [36].

3.5 Numerical Results

We assume M=2000 IoT sensors randomly and uniformly distributed within a geographical area of 5×5 km^2. Unless otherwise specified, we use the simulation parameters listed in Table 3.1.

Fig. 3.2 presents the clustering performance of several algorithms, expressed by the average number of clusters as a function of communication range, d_{th} (averaging over 100 scenarios of SNs). We consider three clustering algorithms, namely Algorithm 1 [30],

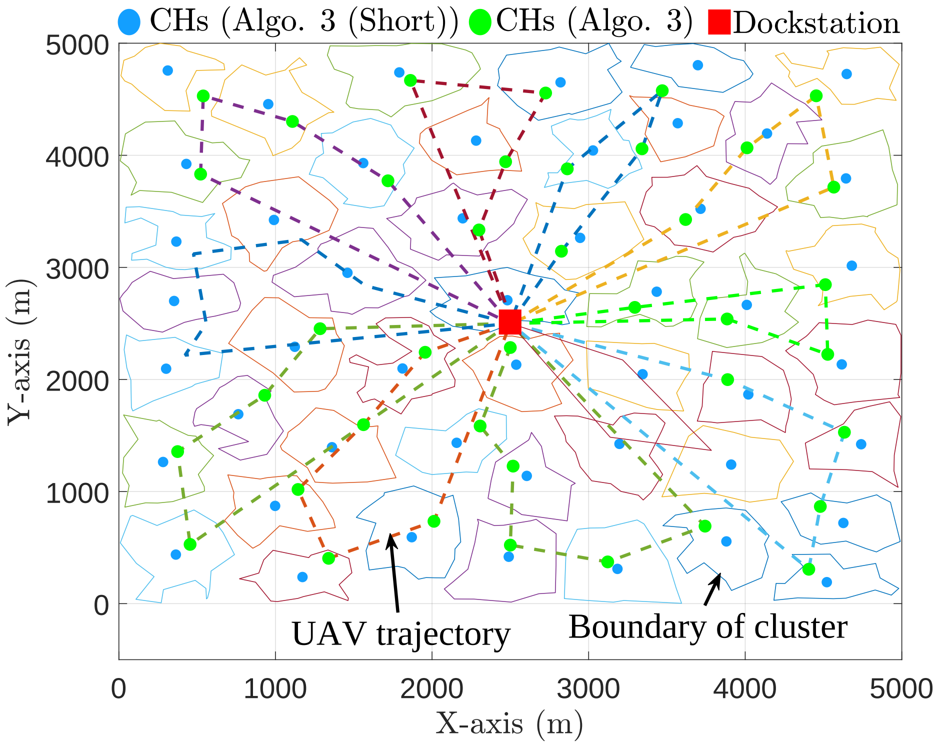

Figure 3.3: An example of CHs locations and UAV trajectories (48 CHs and 11 UAVs).

HCA-based clustering approach [35] and the improved customized k-means-based algorithm Algorithm 3. As d_{th} increases, a smaller number of CHs is needed, as the latter can be reached by a higher number of SNs. Moreover, Algorithm 3 achieves the best clustering performance. Indeed, unlike the other algorithms, Algorithm 3 is capable of adjusting the clusters to constraints (P2.a)–(P2.b) on-the-fly, i.e., while processing the SNs.

In Fig. 3.3, we depict a scenario where Algorithm 3 is used to group 2000 SNs into 48 clusters, from which data is collected using 11 UAVs. We distinguish two variations, Algo. 3 as is, and "Algo. 3 (Short)", where lines 32–34 are omitted. It is obvious that Algo. 3 would result in a more energy-efficient data collection, since UAVs would fly for less time, assuming that they hover directly above each CH to collect data.

For the clustering design of Fig. 3.3, Figs. 3.4–3.5 compare the consumed energy (in kilojoule), number of visited CHs, and number of deployed UAVs performances, as functions of the battery capacity, for different UAV trajectory planning approaches, namely Tabu search (Tabu), simulated annealing (SA), and guided local search (GLS). Performances of these methods are almost similar, with a preference for Tabu. Indeed, Tabu consumes less or equal energy to SA and GLS. Also, as the battery capacity increases (above 2250

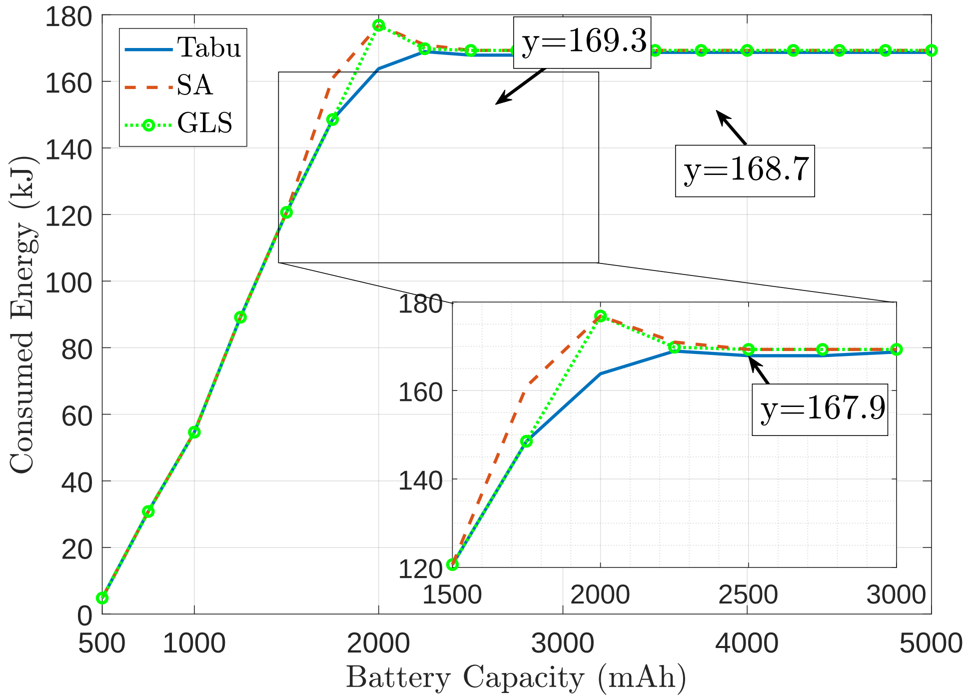

Figure 3.4: Energy vs. battery capacity.

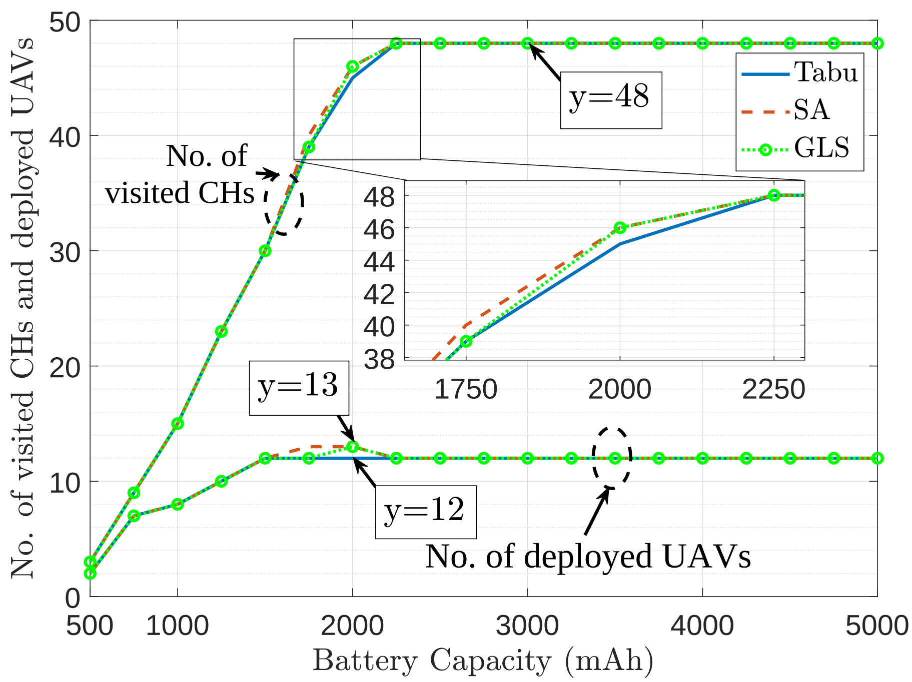

Figure 3.5: No. of CHs and UAVs vs. battery capacity.

mAh), the performance saturates, guaranteeing that data is collected from all CHs. Finally, the optimal battery capacity of 2500 mAh is provided by Tabu, where minimum energy

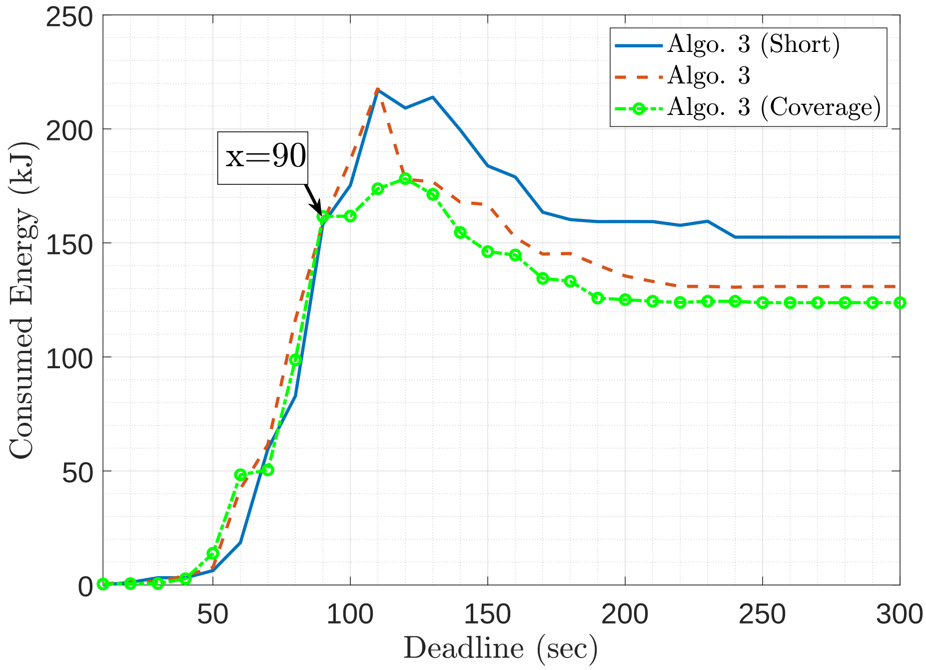

Figure 3.6: Energy vs. deadline.

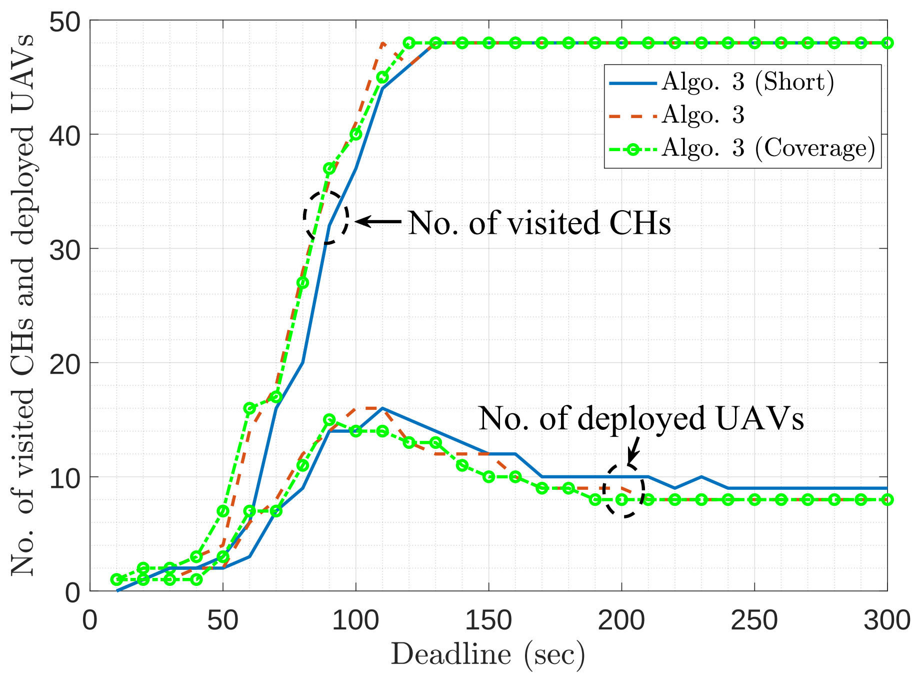

Figure 3.7: No. of CHs and UAVs vs. deadline.

(=167.9 kJ) and number of UAVs (=12) are achieved.

In Figs. 3.6–3.7, Tabu algorithm performances are depicted as functions of the time deadline for variations of Algorithm 3. These include "Algo. 3 (Short)"'and "Algo. 3

(Coverage)", where in the latter, UAVs do not hover directly above CHs, but rather within a covreage range of 180 m from the initial UAV locations defined in Algorithm 3. For all approaches, as the deadline increases, the consumed energy reaches a peak then decreases. Below this peak, the deadline is very small such that it prevents collecting data from all CHs as the latter will be outdated, hence, a small number of UAVs is deployed, which consumes low energy due to short trajectories. In contrast, beyond the peak point, the deadline is long enough to deploy few UAVs that visit all CHs. The peak point corresponds to the critical deadline for which the maximum number of UAVs is deployed to collect data from the CHs. "Algo. 3 (Coverage)" presents the best energy consumption for deadlines above 90 sec, while visiting and deploying similar numbers of CHs and UAVs as Algo. 3. Indeed, "Algo. 3 (Coverage)" compensates for the prolonged data collecting time and energy (due to longer distances to CHs) by shorter flying time and energy. For deadlines below 90 sec, Algo. 3 performs either better or similarly to "Algo. 3 (Coverage)", in terms of energy and number of visited CHs, since hovering exactly above CHs improves the data transmission and thus respects the deadline. Finally, "Algo. 3 (Short)" presents the worst performances as it spends more energy to reach CHs at distant locations, or in contrast, abandon them due to their data becoming outdated.

Table 3.1: Simulation parameters

UAV altitude	H=100 m	Bandwidth	W=10 MHz
UAV speed	v_u=30 m/sec	Speed of light	V=3.10^8 m/sec
Distance threshold	d_{th}=600 m	Mission time	T_f=4 min
Carrier frequency	f_c=2 GHz	Environment parameters	a= 9.61 b=0.16
Time deadline	$T_{d,c}$=140 sec	Max SNs per cluster	F=120
Noise power	σ^2=–109 dBm	Packet size	S_p= 1 Kbyte
TS length	δ=100 msec	Path loss	α=2.7
Battery capacity	$S_u(0)$=3500 mAh	Number of packets	Q_c=50000

3.6 Conclusion

In this Chapter, we investigated the multi-UAV data collection problem in clustered IoT networks, where sensed data have time deadlines. Aiming to optimize the data collection deployment costs in terms of energy consumption, we propose a two-step solution. In the first step, we proposed an algorithm based on k-means clustering to optimize the number and locations of CHs, which gather data from associated IoT sensors. Subsequently, an energy-efficient data collection framework which uses the minimal number of UAVs is presented; in this framework, the UAV trajectories are defined with respect to time deadlines of collected data and energy constraints. Simulation results show the efficiency of the proposed customized k-means clustering which outperform baseline approaches. Also, moving CHs closer to the dockstation provided a significant energy gain. On the other hand, it is shown that Tabu search achieves the best UAV trajectory design, compared to other methods. Finally, the impact of the battery capacity and time deadline is studied in terms of energy consumption, number of visited CHs, and number of deployed UAVs. In the following chapter, we will discuss the integration of a new technology on the communication payload of aerial and stratospheric platforms that will provide energy-efficient communications on several applications including data collection, backhauling and supporting terrestrial and aerial users.

Algorithm 3 IoT sensors clustering algorithm

Input: $\mathcal{N}$, $\{\mathbf{q}_s\}_{s\in\mathcal{N}}$, and $\max_{\text{it}}$ %$\max_{\text{it}}$ is the max. number of CHs
Output: Optimal $\mathcal{K}$, $\mathcal{L}$, and $\{\mathcal{A}_c\}_{c\in\mathcal{K}}$
Set $k = (|\mathcal{N}| \div F)$
for k **to** $\max_{\text{it}}$ **do**
    Set $\mathcal{L}$ randomly %Initial locations of CHs
    Set $\mathcal{L}_{old}$ %Set of zeros
    Set $\mathcal{A}_c = \emptyset$, $\forall c = 1, \ldots, k$ %c indicates the rank of
    CH in $\mathcal{L}$
    Set $error = dist(\mathcal{L}, \mathcal{L}_{old})$ %Convergence parameter
    while $error \neq 0$ **do**
        for $s \in \mathcal{N}$ **do**
            Calculate d_{sc}, $\forall c = 1, \ldots, k$
            Find $c_0 = \arg(\min(d_{sc}))$
            if $d_{sc_0} \leq d_{\text{th}}$ & $|\mathcal{A}_{c_0} \cup \{s\}| \leq F$ **then**
                $\mathcal{A}_{c_0} = \mathcal{A}_{c_0} \cup \{s\}$ %Associate SN s with
                CH c_0
            else
                $\mathcal{A}_{k+1} = \mathcal{A}_{k+1} \cup \{s\}$ %Put c in set of no
                association
            end if
        end for
        Set $\mathcal{L}_{old} = \mathcal{L}$
        Calculate $\mathcal{L}$ as the mean location of the associated
        SNs in $\mathcal{A}_c$, $\forall c = 1, \ldots, k$
        Calculate $error = dist(\mathcal{L}, \mathcal{L}_{old})$
    end while
    if $\mathcal{A}_{k+1} = \emptyset$ **then**
        $\mathcal{K} = \{1, \ldots, k\}$
        Break
    end if
end for
while $\max(d_{sc}) < d_{\text{th}}$, $\forall s \in \mathcal{A}_c$ **do**
    Get $\mathcal{L}$ closer to the dockstation
end while

Chapter 4

Aerial Platforms with Reconfigurable Intelligent Surfaces for Beyond 5G

4.1 Introduction

As the world steps into the deployment of 5G, researchers continue addressing the challenges of ubiquitous connectivity. The role of aerial platforms for wireless networks is an increasingly important one for meeting the communication requirements of 5G/B5G. Indeed, the Third Generation Partnership Project (3GPP) has considered aerial platforms to be a new radio access for 5G (TR 38.811, TR 22.829, and TS 22.125), and several projects have been initiated to provide ubiquitous Internet services, such as HAPSMobile and Thales Stratobus. Due to their 3D-mobility, flexibility, and adaptable altitude,

This work mainly has been published in IEEE Communications Magazine: **S. Alfattani**, W. Jaafar, Y. Hmamouche, H. Yanikomeroglu, A. Yongacoglu, N. Đào and P. Zhu "Aerial Platforms with Reconfigurable Smart Surfaces for 5G and Beyond", *IEEE Communications Magazine* vol. 59, no. 1, pp. 96–102, Jan. 2021.

The term "*Smart*" is used in the title of the aforementioned paper, since there wasn't a unified name, and several names were introduced by the researchers. They include: Large intelligent surface (LIS), reconfigurable intelligent surface (RIS), intelligent reflecting surface (IRS), reconfigurable meta-surfaces, Intelligent Reflectors (IR), Programmable metasurface, Digital coding metasurface, HyperSurfaces etc. The term *"Reconfigurable"* stands for the ability of these surfaces to be controlled to give customized behavior. The term *"Smart"* is selected in the title of that paper in accordance with previous 3GPP standards for similar technologies (e.g., TR 22.867, TR 25.842, TR 22.890, TR 36.848). However, most of the researchers as well as the developing standards recently adopt the term "Intelligent" or the abbreviation "RIS" for this technology. Thus, we switched to this term.

aerial platforms can efficiently support the connectivity of terrestrial and aerial users by enhancing their capacity and coverage, or even providing backhaul links. Based on their operation altitudes, we distinguish two main types of aerial platforms, Unmanned Aerial Vehicles (UAVs) and High Altitude Platform Stations (HAPS). UAVs operate at low altitudes of few hundred meters and act as flexible and agile relays or base stations (UxNB) (TR 22.829). Their use is generally time-limited, ranging from a few minutes to a few hours due to limited onboard energy. Alternatively, tethered UAVs can fly for much longer owing to the continuous supply of power from the tether. By contrast, HAPS operate at higher altitudes of 8 to 50 km above ground (TR 38.811), with current HAPS projects focusing on the 20 km altitude. They allow wider coverage areas and longer flight times compared to UAVs (e.g., Google Loon's flight record is 223 days). To further reduce costs and make aerial platforms more attractive for B5G networks, researchers are constantly searching for new horizons of improvements, including fuselage materials, battery, fuel, and solar-cell technologies, as well as enhancing trade-offs in energy efficiency (EE) and communication performance.

From the communication perspective, passive reconfigurable intelligent surface (RIS) has emerged as a potential substitute for active communication components [10]. RIS is a thin and flexible metasurface equipped with programmable passive circuits to "reflect" received signals in a controlled way. An RIS can then positively exploit the propagation environment to enhance the quality of a communication link between a transmitter and a receiver, known as *RIS-assisted communication*, or to transmit signals more effectively, identified as *RIS-initiated communication*. Efforts have been made to evaluate and explore the benefits of RIS. For instance, NTT DOCOMO collaborated with Metawave and demonstrated an increase in data rate of approximately ten times using RIS at 28 GHz [37]. Other notable initiatives include the VisoSurf consortium for RIS prototyping [38], and Greenerwave, which is already marketing RIS that operate at frequencies up to 100 GHz.

Considering the opportunities presented by RIS technology, we discuss in this Chapter a novel paradigm where RIS is deployed in aerial platforms, and propose a control architecture workflow for communication, mobility, and sensing. We then describe potential use cases where RIS-equipped HAPS and UAVs aim to achieve communication objectives, such as backhauling, coverage extension, low-cost network densification and WSN/IoT data collection. Finally, related challenges are presented. To the best of our knowledge, this is the first work that presents an in-depth discussion of the use of RIS-equipped aerial platforms, their control architecture, as well as their potential applications and challenges.

4.2 Overview of RIS in Communications

4.2.1 Background

Researchers have traditionally focused on improvements in hardware and transmission techniques to enhance link quality between a transmitter and a receiver. This research stream has sought ways of mitigating the impact of environmental objects on the quality of wireless signals. However, a different approach has emerged whereby the environment between transmitters and receivers can be managed to initiate or support wireless communications. For initiated communications, various ambient energy sources, (RF, solar, etc.), can power ultralow-power electronics to enable sensing functions and backscatter communications through different environmental objects (see [39] and references therein). For assisted communications, the idea of controlling surfaces and objects in wireless propagation environments was proposed earlier, around two decades ago. The objective was to mitigate undesired interference and improve the desired signal through the use of frequency selective surfaces (FSS)[1]. These FSS resemble bandpass or bandstop filters, and they can be integrated into indoor walls. Also, they can be equipped with sensors and diode switches for flexibly controlled response.

While FSS's key function has been to filter signals and alleviate interference, another vision of utilizing the propagation environment is to combine the scatters of the desired signals and direct them to the targeted users. In this context, passive reflectors (a.k.a., mirrors) consisting of metallic sheets or high conductivity materials have been designed for indoor and outdoor environments, aiming to enhance the received power. For outdoor environments, authors in [41] suggested using passive reflectors on top of buildings to focus reflected signals from ground base station (gBSs) toward users. Compared to conventional coverage enhancement approaches, such as relaying and gBSs densification, passive reflectors made of low-cost elements offer flexible deployment, easy maintenance, and improved EE. Nevertheless, passive reflectors are constrained by Snell's law of reflection, and once designed, they have a fixed response. Hence, they are inherently unable to accommodate the dynamics of wireless environments. Alternatively, to capture the wireless environment dynamicity, "active" surface technologies were proposed in [42], where the

[1]See a commercial example of FSS in [40].

walls consist of a massive number of electromagnetically radiating and sensing elements working as large smart antennas, and regarded as an extension to the massive multiple-input multiple-output (MIMO) concept. While passive reflectors utilize material properties to direct electromagnetic waves, active surfaces require integrating electronics, antennas and communication circuits in walls to work as full transceivers. Although they might have better performances, the circuit complexity, material costs, and energy consumption are higher than for passive surfaces.

Inspired by recent advances in the physics of metasurfaces and meta-materials, passive RIS technology has been presented as an interesting add-on to various applications in wireless communications [10]. Metasurfaces are distinct man-made 2D meta-materials, consisting of thin layers of metallic/dielectric inclusions. Metasurface units can be arranged in arrays and designed to have peculiar electromagnetic (EM) features with customizable interactions with the EM waves. Indeed, these units can realize abrupt phase shifts and anomalous reflections and refractions, where the phase of the wavefronts can be altered, a process known as phase discontinuity [43]. Moreover, the reflected and refracted EM waves can have an arbitrary direction beyond Snell's law, subject to *"the generalized laws of reflection and refraction"* [43]. To bypass the fixed response of metasurfaces, digital meta-materials were proposed in [44], where the manipulations of the EM waves were reconfigurable by digitally controlling the metasurface units, i.e., switching between different meta-material responses using biased diodes. Subsequently, an advanced layout is proposed in [10], wherein a programmable metasurface layer was integrated with an IoT gateway and a control layer to form a thin film, called "HyperSurface tile", coating surfaces and environmental objects. Hence, the interaction of the surfaces with the EM waves can be programmed and controlled remotely via software.

4.2.2 Types of Communications with RIS

Given the capabilities demonstrated in physics for controlling and reconfiguring EM waves with meta-materials, wireless communication researchers have started investigating the use of RIS in different ways, particularly for *RIS-assisted communications* and *RIS-initiated communications.*

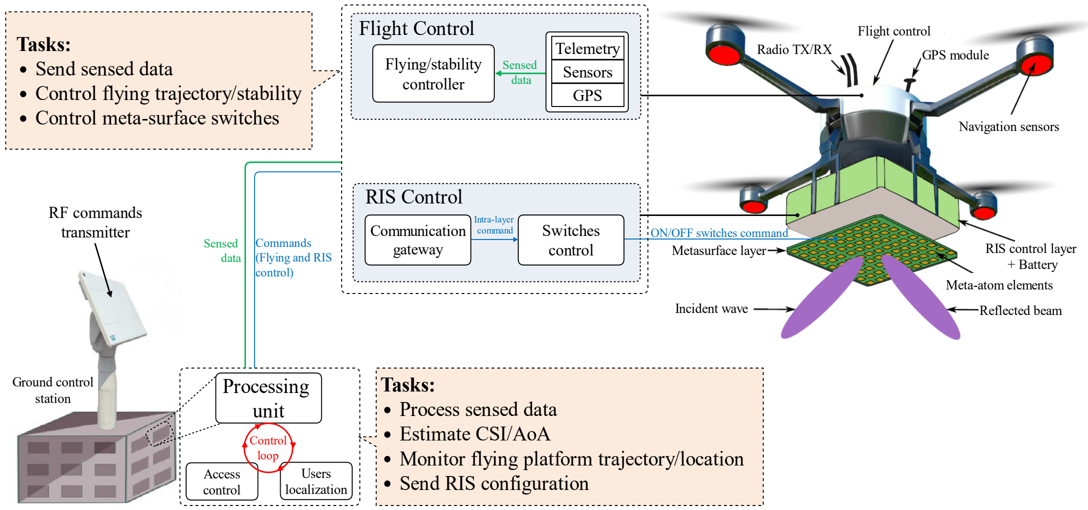

Figure 4.1: Control architecture of RIS-equipped aerial platforms.

4.2.2.1 RIS-Assisted Communications

Aiming for efficient delivery of transmitted signals, most research has focused on using RIS as a relay to enhance the received signal at end-users. Different objectives have been considered, such as maximizing data rates or spectral efficiency, extending the coverage area, mitigating interference, and minimizing consumed energy. For instance, the authors of [45] showed that by optimizing the RIS phase shifts, quadratic increase in the signal-to-noise ratio (SNR) is realized, and better spectral efficiency than relays can be achieved. To practically substantiate the advantages of RIS-assisted communications, an experimental testbed was implemented in [46] demonstrating that RIS can solve the coverage-hole problem caused by obstacles in millimeter-wave (mmWave) networks. Additionally, motivated by the EE potential of RIS, researchers have focused on supporting energy-constrained communications. For instance, authors in [47] demonstrated that, even with low-resolution phase shifters in RIS-assisted communications, EE can be improved by 40% compared to conventional relaying systems.

4.2.2.2 RIS-Initiated Communications

In contrast to previous works, RIS is being tested as an energy-efficient and low-complex transmitter. The idea is to connect the RIS with a nearby RF source and, through phase shifting, data can be encoded and transmitted. While the reliability of RIS-initiated communications were analyzed in [11], authors of [48] validated through experiments the design of a high order modulation RIS-based transmitter, where a digital video file was modulated and transmitted through the RIS without requiring filters, mixers, or power amplifiers.

4.3 Aerial Platforms with RIS: Integration and Control Architecture

Most of current research works on RIS are focused on its use in terrestrial environments, e.g., RIS equipping buildings facades. However, motivated by the numerous aforementioned RIS capabilities, and the advanced features of aerial platforms, we envision that the usage of RIS in aerial platforms will offer great flexibility and support for wireless networks. Integrating RIS on aerial platforms can be done in several ways depending on the platform's shape. For instance, the RIS can coat the outer surface of a balloon or an aircraft, or it can be installed as a separate horizontal surface at the bottom of a UAV, as shown in Fig. 4.1. The reconfiguration of such surfaces can be realized through lumped elements embedded in the reflector units or via the distributed control of some material properties. Examples of lumped elements include PIN diodes [49], varactor (or varicap) diodes [50], and radio frequency micro-electro-mechanical systems (RF-MEMS) [51, 52]. By tuning the lumped elements, the resonant frequency of the reflectors can be changed, hence achieving the desired wave manipulation and phase shift. To manage high frequency signals, e.g., mmWave and free-space optical (FSO) communication, tunable materials such as liquid crystal [53] and graphene [54, 55] are used to design the metasurface reflector units.

In order for the RIS-equipped aerial platforms to perform communication functions properly, the channel information needs to be acquired and the RIS should be accurately configured. The control can be managed at two levels: Ground control station and aerial platform, as illustrated in Fig. 4.1.

4.3.1 Ground Control Station

This controller consists mainly of a processing unit that analyzes the sensed data from the aerial platform, and the access control and users localization conditions, acquired through information exchange with gBSs and/or gateways. Given a set of global policies (e.g., flying regulations, power, etc.) and objectives (e.g., coverage, SNR, EE, etc.), the processing unit ensures the joint management of the aerial platform's flying and communication functions.

Moreover, it estimates the channel state information (CSI) and angle of arrival (AoA) between users and the aerial platform to determine the best RIS configuration setup.

4.3.2 Onboard Aerial Platform Control

The onboard aerial platform's controller consists of two units, namely the *flight control unit*, and the *RIS control unit*. The former receives motion commands from the ground station, and ensures the platform's stabilization. By contrast, the *RIS control unit* receives the optimized RIS configuration, translates it into a switch control map, and applies it to the metasurface layer for directing incident signals to targeted directions.

4.4 Aerial Platforms with RIS: Potential Use Cases

To demonstrate the potential benefits of integrating RIS in aerial platforms, we detail here several novel integration use cases.

4.4.1 HAPS with RIS to Support Remote Areas

Connecting sparse users or sensors in remote areas via terrestrial networks is deemed to be expensive and unprofitable to operators due to the high costs of typical gBSs and wired backhauling infrastructure. Satellites have been proposed to serve remote areas; however, due to high deployment costs and large communication delays, satellites are considered as a last resort solution for remote users. Also, due the excessive path-loss, collecting data from remote low-powered IoT sensors might not be feasible. Alternatively, HAPS have been introduced as a cost-effective solution for remote users connection and data collection [56, 57].

HAPS are quasi-stationary platforms located in the stratosphere at a fixed point relative to the earth. Since the wind's speed in this region is weak, low power is required to stabilize the platform. Moreover, the coverage area of a HAPS is greater than that of a gBS. For instance, the International Telecommunication Union (ITU) suggested that the HAPS' coverage radius be up to 500 km (ITU-R F.1500); however, current HAPS projects have less than 100 km coverage radius to achieve high area throughputs.

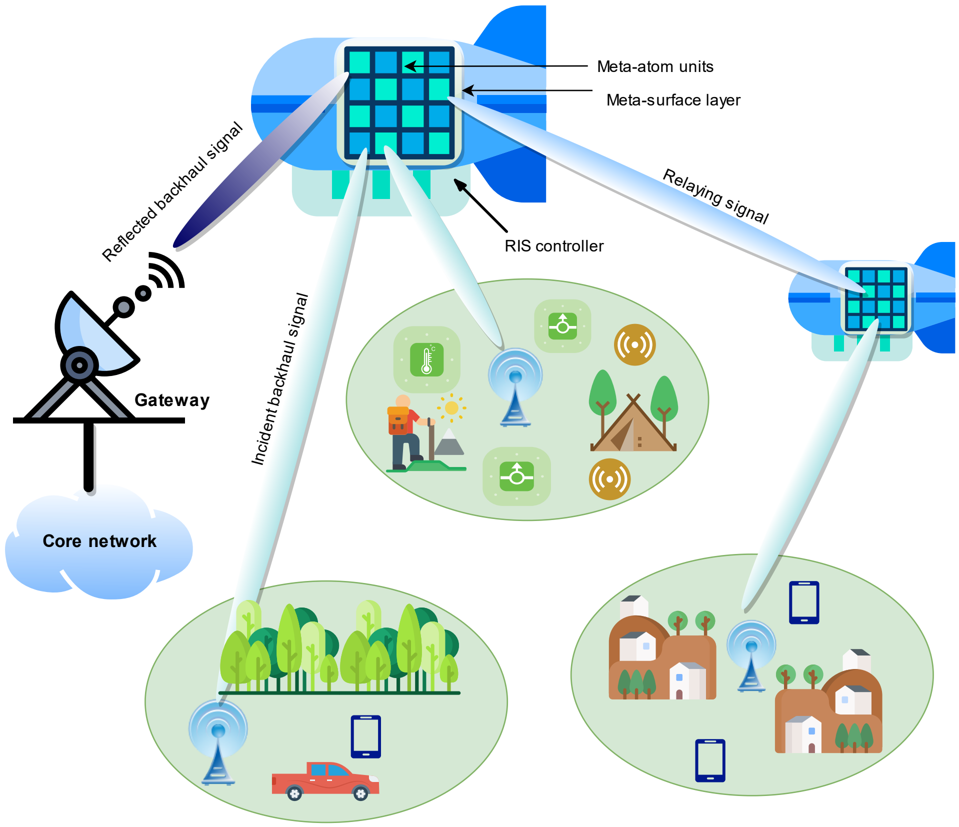

Figure 4.2: HAPS-RIS for backhauling remote gBSs, supporting IoT data collection and providing inter-HAPS communications.

HAPS are mostly powered by solar/fuel energy, and their flight duration may vary from several hours to a few years. The energy consumed by a HAPS is mainly for propulsion, stabilization, and communication operations. Typically, a HAPS is used in communications either as a BS (HAPS-BS) or as a relay station (HAPS-RS). Although a HAPS-BS has more capabilities than a HAPS-RS, it involves a higher cost, a heavier payload, and an increased energy consumption. When solar cells are used, the harvested energy may not be sufficient for operations. For this reason, other power sources are added to complement the solar energy. Nevertheless, the EE of HAPS is still an open problem, which directly impacts the flight duration.

In designing a HAPS deployment, low energy consumption, light payload, and reliable communication need to be achieved. To this end, motivated by the benefits of RIS, we propose using a HAPS equipped with RIS (HAPS-RIS) for wireless traffic backhauling from remote area BSs, and data collection from sparse remote IoT sensors. In addition, it can be used for inter-HAPS communications. The envisioned scenarios are depicted in Fig. 4.2, where BSs handle the traffic of a few clustered users and transmit the traffic to the HAPS. Also, these BSs can act as cluster heads, which collect the data of IoT sensors and send it to the HAPS. Through the HAPS' RIS, the received signals are smartly "reflected" toward a gateway station, which is connected to the core network. If a gateway station is not within the HAPS coverage range, the RIS can be configured to "reflect" the signals toward another HAPS and thereby reach the gateway station in a dual or multi-hop fashion.

Using HAPS-RIS has several advantages. First, it reduces the used power for communication functions, since directing signals can be realized in a nearly-passive way, without RF source or power amplifiers, and only minimum amount of power is required for the RIS control unit. Second, since RIS is made of thin and lightweight materials, the HAPS payload is lighter even if a large number of reflectors is deployed. Third, given the reduced communication components and payload, the required stabilization energy is minimized. The simplification in communication circuits and minimization of consumed energy yield to extended flight duration and reduced HAPS deployment costs.

The performance of RIS-assisted communications strongly depends on the number of reflectors. The dimensions of a metasurface reflector unit (a.k.a., meta-atom) are proportional to the wavelength [10]. Typically, a HAPS is a giant aircraft with a length between 30 and 200 m, which has the potential to accommodate a large number of reflectors, especially in high frequencies. The large number of reflectors would have a significant impact on the directivity gain, hence better SNR performance than HAPS-RS can be achieved [45]. In terms of energy consumption, the switches on the metasurface layer consume very low power. A recent experiment showed that each meta-atom consumes 0.33 mW when its switch diode is set to ON [58]. Thus, for a HAPS with 10,000 meta-atoms, the maximal power consumed by the metasurface layer when all switches are activated would be about 3.3 W, which constitutes a very promising result. Hence, HAPS-RIS is expected to achieve a better EE than HAPS-RS [47]. Finally, it is worth noting that RIS supports full-duplex communication [45]. Indeed, unlike relays experiencing high noise and residual loop-back self-interference, which are issued from active RF components, RIS bypasses these constraints by only exploiting the intrinsic properties of the reflecting material. Thus, HAPS-RIS would be more spectrally efficient than HAPS-RS. Table 4.1 summarizes the main differences between HAPS-RS and HAPS-RIS communications.

Table 4.1: Comparison between HAPS-RS and HAPS-RIS for communication

Aspect	HAPS-RS	HAPS-RIS
Energy Consumption	**Medium** (Process, amplify, and forward signals)	**Very low** (RIS control)
Payload	**Heavy** (Complex circuits: converters, mixers, amplifiers and antennas).	**Light** (RIS designed as a thin sheet film coating HAPS outer surface).
No. of Commun. Units	Limited by frequency and energy constraints, and by allocated space for communication circuits.	Limited by HAPS's size and used frequency band.
Performance (directivity gain)	Good performance; low EE.	High EE; performance depends on RIS size and reconfiguration capability.
Spectral efficiency	Good in full-duplex, but limited by noise and self-interference.	High, always full-duplex and no noise or interference.
Cost	**High** (Several active components; short flight duration)	**Low** (Low-cost RIS; extended flight duration)

4.4.2 UAVs with RIS to Support Terrestrial and IoT Networks

RIS can be combined with UAVs and their attendant benefits, namely, agility, flexibility, and rapid deployment, to assist terrestrial cellular networks in a cost-effective manner.

Typically, RIS can be carefully mounted on a swarm of UAVs (UxNB-RIS) to create an intermediate reflection layer between gBSs and isolated users, as illustrated in Fig. 4.3. In this way, the UxNB-RIS allows a smooth mechanical movement of the RIS layer, while the RIS enables digitally-tuned reflections of incident signals to improve service for isolated users. Hence, besides its low manufacturing cost, UxNB-RIS can be rapidly deployed to increase operators' revenue per user by filling coverage holes and meeting users' high-speed broadband needs.

Coverage holes or blind spots can occur for various reasons, such as disruption of some gBSs due to maintenance, failures, or natural disasters. Also, future communication networks are exploring the use of higher frequencies with wider spectrum bandwidths, such as mmWave and FSO, to tackle the increasing throughput demands and the spectrum scarcity problem. A major challenge hindering their widespread use is their vulnerability to blockages in the propagation environment, which requires perfect line-of-sight (LoS) links but may create coverage holes in regions with impenetrable blockages. In such a context, UxNB-RIS, which has a panoramic view of the environment, can provide full-angle 360° reflection and thus can reduce the number of reflections compared to terrestrial RIS [59]. This approach can also be adopted to deliver new signals to users served by a heavily loaded gBS, and thus help in balancing the traffic of congested cells.

Furthermore, as discussed previously in Chapters 1 and 2, UAVs can be effectively utilized for data collection. However, a serious challenge for UAVs utilization, is their limited on-board energy. To mitigate the energy consumption issue, UxNB-RIS can be utilized for energy-efficient data collection. Authors of [60] advocate the use of UxNB-RIS for IoT data collection for two reasons. First, to reduce the communication delay and to enhance the freshness of information, since UxNB-RIS requires one time slot while half-duplex relays on UAVs require two time slots. Second, to reduce the UAV energy consumption and extends its flight duration, due to the passive RIS elements compared to conventional active processing and relaying onboard equipment. From another perspective, authors of [61] studied the utilization of UxNB-RIS for secure data collection from IoT sensors, where the transmitted signals by the sensors will be reflected constructively toward the main legitimate receiver while destructively combined at the eavesdropper.

Moreover, in the absence of channel knowledge, UxNB-RIS can be used for spatial diversity to combat channel impairments (e.g., fading and path-loss). A typical user can actually receive several copies of the desired signal over different transmission paths generated by reflections through the swarm of UxNB-RIS, which enhances the reliability of the

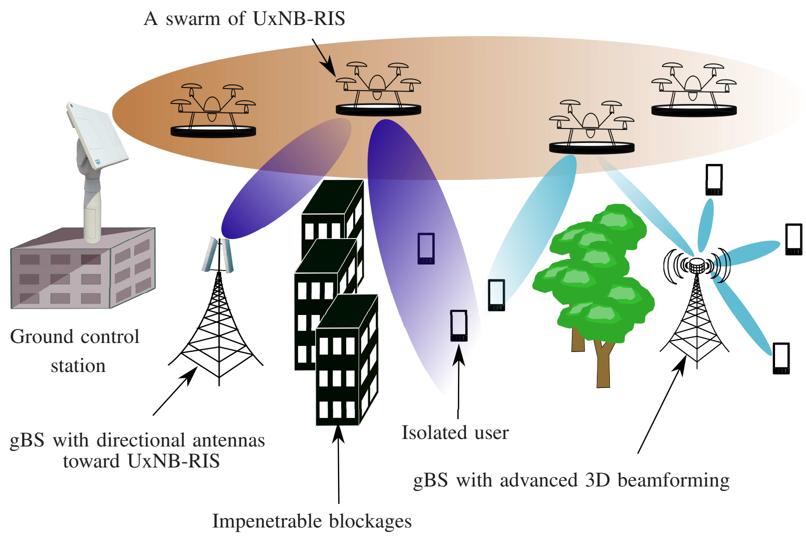

Figure 4.3: Communication support of terrestrial networks with blockages using UxNB-RIS.

reception. Alternatively, fading can be seen as a source to increase the degrees of freedom. A high-rate data stream can be divided into many lower-rate streams and transmitted over different transmission paths using the swarm of UxNB-RIS. Thus, the user can retrieve independent streams of information with sufficiently different spatial signatures, resulting in improved data throughput. It is also worth noting that RIS can absorb a certain amount of the impinging signals and leverage them to recharge the UxNB-RIS.

4.4.3 Tethered Balloons with RIS to Support Terrestrial/Aerial Users

UxNB has been viewed as a candidate solution for several wireless challenges, such as coverage and capacity extension. Although they have promising advantages, such as flexible placement and LoS communication links, there are also several limitations that militate against using UxNB. First, the limited onboard energy makes UxNB exclusively suitable for short-term deployments. Second, backhauling from a UxNB is typically through a wireless link, which has limited reliability and capacity compared to wired backhauling links. To bypass these limitations, a tethered UxNB has been recently introduced. The tether provides the UxNB with both data and power. Thus, longer flight times and reliable backhaul links are achieved. However, a tethered UxNB consumes a considerable amount of energy for flying, hovering and transmitting signals, which yield to increased deployment and operational costs. A more cost-effective alternative that we propose here is using a tethered balloon equipped with RIS (TBAL-RIS), as depicted in Fig. 4.4.

Inspired by recent works and prototypes that use RIS as transmitters [11, 48], we point out that TBAL-RIS can be used as a low-cost wireless access point to connect or enhance the capacity of urban users. By illuminating the outer surface of the TBAL-RIS with an RF feeder, the information provided by the tether data link can be encoded and transmitted. Thus, the RIS controller adjusts the phases of the reflected signals to generate different beam directions that can serve multiple users. Compared to a tethered UxNB, TBAL-RIS has several advantages. Unlike a small tethered UxNB, a TBAL is large and can accommodate a higher number of reflectors. Also, compared to typical gBSs, network densification with TBAL-RIS in urban environments is more feasible and cost-effective. Since TBAL-RIS provides near-field communications with strong LoS links to users, it is expected to provide better spectral efficiency than MIMO gBSs, considered as a far-field communication system with many NLoS links, high interference, and pilot contamination [62]. Furthermore, unlike down-tilted antennas in gBSs, the TBAL-RIS can sustain reliable connectivity to UAV users (UAV-UEs) such as delivery drones. Thus, both terrestrial and aerial users can be served simultaneously.

Moreover, a TBAL does not continuously drain power for lifting and hovering, as it uses lifting gases. Although the altitude of a TBAL is limited by the tether's length, some flexibility in its position is available by controlling the tether's direction to offer better coverage in certain spots. Besides, a backhaul fiber optic link along the tether can be installed to guarantee the TBAL's connectivity to the core network. A processing unit is also placed at the TBAL's launching point to control its movement, determine the targeted users, and send the optimum RIS configuration.

4.5 Related Research Challenges

As the research of RIS in wireless communications is still in its infancy, several challenges and open problems remain to be addressed. In the following, we discuss some key issues.

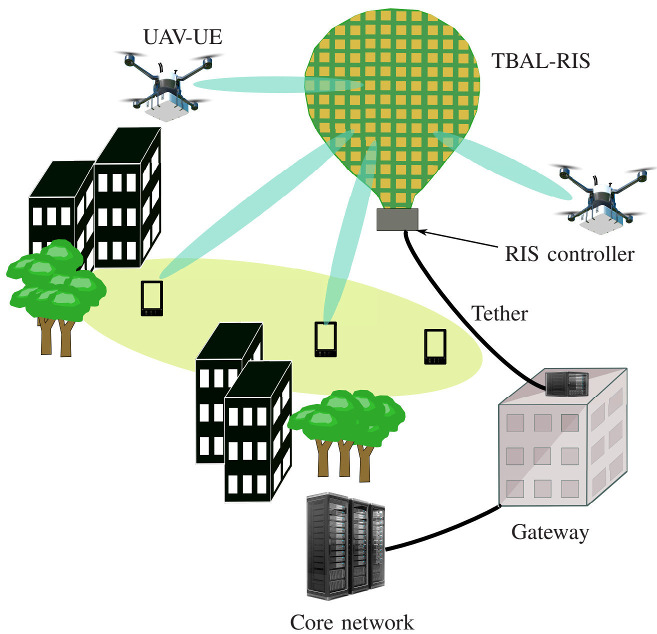

Figure 4.4: Communications support of terrestrial and aerial users using TBAL-RIS.

4.5.1 Accurate RIS and Aerial Channel Models

Most of the existing research works consider RIS with perfect manipulation of the EM wave and ideal phase shifts. However, there is a paramount need for practical RIS models that consider the configuration capabilities and the reliability with different communication frequencies and diverse numbers and sizes of RIS units.

Furthermore, although several air-to-ground channel models have been developed, integrating RIS in aerial platforms is a new direction that requires the investigation of new aerial models that consider RIS capabilities with aerial platforms properties. Some important factors that could affect path-loss models need to be analyzed, such as reflection loss, correlation between RIS units, and atmospheric attenuation. Moreover, the mobility of aerial platforms may cause fluctuations and beam misalignments which have to be considered, especially for HAPS and high frequency communications.

4.5.2 RIS Deployment on Aerial Platforms' Surfaces

Aerial platforms have different surface shapes and types. They might be flat, like the bottom of a UAV, or curved, like the outer surface of an aircraft or balloon. How such an RIS deployment may affect metasurface configuration and performance has not been investigated yet.

4.5.3 Benchmarking the Operations of RIS, Relays, and MIMO

Given the considerable differences that exist in the operations of RIS, relays, and MIMO, there is a compelling need to study from the system level viewpoint the trade-offs that exist for improved performance, flexibility and cost of deployment, and energy efficiency, of these three technologies when integrated with different types of aerial platforms.

4.5.4 Simulation Tools for RIS Behavior

To the best of our knowledge, there is no simulator that considers the complex structures of metasurfaces and simulates the RIS capabilities and behaviors. Current ray optics simulators consider conventional reflectors that adhere to Snell's law and cannot simulate the RIS ability of adjusting the phases and the reflection directions of the impinging signals. The existence of such simulators is important to validate the performance and energy efficiency gains when integrating RIS in aerial platforms.

4.5.5 Channel Estimation and RIS Control Update

One of the fundamental assumptions in most current RIS research is the availability of CSI, which is essential for performing perfect reflection. However, gaining such knowledge within the channel's coherence time in typical dynamic wireless environments with mobile platforms is still an open problem. One solution to this is by incorporating low-cost sensors in metasurfaces [39], which frequently sense the environment and send measurements to the controller. The latter computes and sends back the updated optimal RIS configuration. Alternatively, the reciprocity of the channel can be exploited to estimate the CSI for pre-determined phase shifting configurations, or machine learning techniques, such as supervised learning and reinforcement learning, can be leveraged to find the optimal RIS configuration. However, such techniques require large amounts of data and/or long training times. Hence, the delay impact due to distance and CSI estimation process merits further investigation.

4.6 Conclusion

In this Chapter, we discussed the potential integration of the recent RIS technology into aerial platforms as a novel B5G paradigm. First, we provided an overview of RIS technology, its operations, and types of communication. Then, we proposed a control architecture workflow for the integration of RIS in aerial platforms. Potential use cases were discussed where different types of aerial platforms, namely HAPS, UAVs and TBALs, were exploited. Integrating RIS in aerial platforms provides several advantages, including energy efficiency, lighter payload, and lower system complexity, which results in extended flight durations and more cost-effective deployment to support wireless networks. However, several issues need to be tackled for the smooth integration of this novel paradigm. In the next Chapter, we will study in detail the communication performance and the link budget for RIS integrated on aerial platforms.

Chapter 5

Link Budget Analysis for Reconfigurable Intelligent Surfaces in Aerial Platforms

5.1 Introduction

As the fifth generation (5G) of wireless systems are being actively deployed, researchers in the wireless community started investigating new technologies and innovative solutions to tackle the challenges and fulfill the demands of the next generation network (6G). One of the main challenges consists in energy-efficiently supporting ubiquitous connectivity with high data rates. With the inherent limitations of terrestrial environments, non-terrestrial networks are envisioned as an enabling technology for ubiquitous connectivity in future wireless communications. Indeed, non-terrestrial networks address several issues, including coverage holes and blind spots, sudden increase in throughput demands, and terrestrial networks failures [4]. Aerial platforms, such as unmanned aerial vehicles (UAVs), high altitude platform station (HAPS), and low earth orbit (LEO) satellites, are able to address these challenges due to their wider coverage footprints, strong line-of-sight (LoS) links, and flexible deployment compared to terrestrial networks [3, 6, 5]. Moreover, the standardization efforts of the Third Generation Partnership Project (3GPP) aiming to utilize aerial platforms for 5G and beyond has established a significant progress, as demonstrated by

This work mainly has been published in IEEE Open Journal of the Communications Society: **S. Alfattani**, W. Jaafar, Y. Hmamouche, H. Yanikomeroglu and A. Yongacoglu, "Link budget analysis for reconfigurable smart surfaces in aerial platforms", *IEEE Open Journal of the Communications Society,* , vol. 2, pp. 1980-1995, 2021.

the standardization documents TR 38.811 [7], TR 22.829 [8], and TS 22.125 [9]. Furthermore, several commercial projects are either in their initial phases of deployment or under development, which aim to design different types of aerial platforms capable of supporting wireless communications. Such projects include Starlink LEO constellation by SpaceX [63], the Stratobus HAPS by Thales [64], and the Nokia Drone Networks [65]. Nevertheless, aerial platforms are not yet at their cutting edge technology, and their current size, weight, and power (SWAP) limitations need to be further improved.

On the other hand, reconfigurable intelligent surfaces (RIS) were recently introduced as an energy efficient enabling technology for next generation wireless networks [66]. The deployment and utilization of RIS in terrestrial networks has been extensively studied, and several research works and prototypes, as well as industrial experiments, demonstrated the potential of this technology, which were summarized in [67, 68].

Given the potential spectral and energy efficiencies of RIS-assisted communications, and the stringent energy requirements of communications through aerial platforms, equipping the latter with RIS becomes an attractive solution to the SWAP issue. Indeed, due to the low-cost and negligible energy consumption of RIS reflectors, their use in aerial platforms is expected to support low-cost wireless communications for extended flight duration. In our previous work [69], Chapter 4, we discussed the feasibility of integrating RIS into different types of aerial platforms. We proposed a platform's control architecture, detailed potential use cases, and exposed the associated challenges. Few other works appeared recently in the literature that study different aspects of integrating RIS on aerial platforms. In the context of UAVs only, the authors of [59] showed that using RIS in UAVs enables a panoramic view of the environment, which can provide full-angle 360° signal reflections compared to 180° reflections in RIS-assisted terrestrial networks. In [70], the authors presented potential use cases of RIS mounted over UAVs, then discussed the main related challenges and research opportunities. Similarly, [71] investigated the potential of RIS-equipped UAV swarms, where a use case was studied to demonstrate the achievable data rate performance of such systems. The authors of [60] investigated the wireless sensors data collection problem where sensors are assisted by an RIS mounted over a UAV to reach the collecting sink. The objective was to maintain data freshness through accurate optimization of the UAV's location and the RIS phase shifting configuration. Finally, in the context of LEO satellites, the authors of [72] investigated the utilization of RIS to support inter-satellite links in the terahertz (THz) band. The results demonstrate a significant performance improvement in terms of bit error rate, compared to non-RIS-assisted communications.

The previous works did not thoroughly investigate the RIS-enabled communication link, thus link budget analysis for RIS-assisted non-terrestrial networks is still missing. However, in the terrestrial counterpart, a number of works studied the path-loss model for RIS-assisted communications [11, 58, 73, 74, 75]. While most of these models are solely based on mathematical analysis using different approaches, some models are experimentally validated [58]. These studies revealed the existence of two regimes that govern the performance of RIS-assisted communication systems. The first one is the "specular reflection" paradigm, where the path-loss model is analyzed using geometrical optics and imaging theory, while the second is the "scattering" paradigm, which obeys to the plate scattering theory and radar cross section analysis. The factors that determine the governing regime of the RIS-assisted systems are the geometrical size of the RIS units, the communication frequency, and the distances separating the RIS from the transmitter and receiver. Typically, when the RIS is within relatively short distances from the transmitter and receiver or the RIS units are electrically large, e.g., their dimensions are 10 times larger than the wavelength denoted λ, the path-loss undergoes the specular reflection paradigm [11, 58, 76]. Otherwise, i.e, when the distances between the RIS and transmitter or receiver are very large or the RIS units dimensions are very small, then the RIS-assisted communication system follows the plate scattering reflection paradigm [77, 78]. To be noted that the scattering paradigm can be designated as the far-field, whereas the specular reflection is often known as the near-field.

Due to the specific design and environmental characteristics of aerial platforms compared to terrestrial systems, their link budget analysis, when equipped with RIS, is expected to be different. Nevertheless, this study is necessary to assess the benefits of RIS-enabled aerial platforms. Three major factors impact the feasibility of RIS-enabled aerial platforms, namely the operating frequency or wavelength, the platform's surface area reserved for RIS, and the operating altitude. Indeed, while higher frequency signals are preferable for larger capacity links and enabling the deployment of more RIS reflector units, they are more vulnerable to path-loss degradation issued mainly from the communication distance and atmospheric attenuation. Also, larger platform RIS size may lead to a higher reflection gain, which may not be realizable for practical platform sizes. Finally, although platforms operating at higher altitudes might be preferable, due to their larger coverage footprint, they suffer from excessive propagation losses that may not be compensated even with large RIS.

Following our vision of RIS integrated on aerial platforms and the attendant benefits presented in Chapter 4, we aim in this Chapter to provide the link budget analysis of RIS-enabled aerial platform communication systems under the specular and scattering reflection paradigms. The received power of the system, for different RIS-enabled platforms, is calculated while taking into account the signal strength losses due to the specific characteristics of each platform. To minimize signal losses, we derive the optimal platform location and feasible maximum number of RIS reflectors onboard of each platform. Link budget expressions are then derived for realistic communication conditions, as defined in the 3GPP standards. Finally, numerical results are provided to support the proposed link budget analysis. The main contributions of this chapter are highlighted as follows:

1. To the best of our knowledge, the performance parameters of RIS-enabled communications have been derived only for terrestrial networks, and not for non-terrestrial systems where different signal losses are experienced due to specific characteristics of aerial platforms and atmospheric phenomena. The impact of these factors is taken into account in this study.

2. For the first time, we investigate the link budget analysis for RIS-enabled aerial platform communications given different types of platforms, namely UAVs, HAPS, and LEO satellites. For optimal performance, we optimize both the platforms' locations and feasible maximum number of mounted RIS reflectors.

3. We extend the link budget analysis to more realistic channel conditions, as defined in the 3GPP standards. Related parameters evaluation and link budget analysis have been carried out by providing numerical results.

The remaining of the Chapter is organized as follows. Section 5.2 discusses the conditions of the reflection and scattering paradigms, then analyzes the link budget for RIS-assisted terrestrial networks. Next, Section 5.3 exposes the characteristics of aerial platforms, derives the optimal platform placement for RIS-assisted aerial communications, and investigates the related link budget under both reflection paradigm types. Numerical results for the terrestrial and non-terrestrial RIS-assisted systems are presented and elaborated in Section 5.4. Finally, main conclusions of this chapter are summarized in Section 5.5

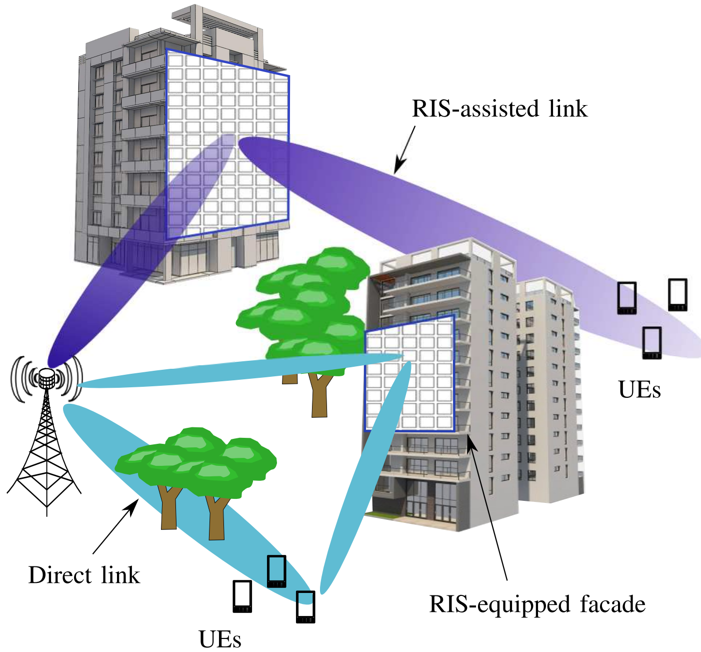

Figure 5.1: System model of RIS in a terrestrial environment.

5.2 Link Budget Analysis for RIS-Assisted Terrestrial Networks

In the following, we present the link budget analysis for RIS-enabled terrestrial communications, e.g., RIS mounted on a building. Given the identified specular and scattering reflection paradigms, we derive the related received power expressions.

Typically, terrestrial environments are characterized by several blockages, which result in high path loss, especially in dense-urban and urban environments. Accordingly, terrestrial network planning relies on cellular densification, where several base stations (BSs) are deployed in a relatively small area to ensure coverage of all users within the area, at the expense of additional costs and inter-cell interference. To alleviate such inconveniences, the RIS can be deployed on the facades of buildings and used to either extend the cellular coverage or improve the signal quality in poorly served areas. As shown in Fig. 5.1, the forwarded signal by the RIS, from the BS to the user-equipment (UE), can either substitute the direct link when the latter is absent, otherwise, be added constructively to the weak direct link in order to strengthen the received signal.

5.2.1 The Specular Reflection Paradigm

The relation that dictates the governing paradigm of the RIS-assisted communications has been defined in [58, 79] as follows:

$$d_{\mathrm{lim}} = \frac{2A_t}{\lambda}, \tag{5.1}$$

where d_{lim} denotes the maximum distance between the RIS and either the transmitter (Tx) or the receiver (Rx) in the specular reflection paradigm[1] , and A_t is the total RIS area.

When the length and width dimensions of the RIS units are large enough, i.e., above 10λ, and the distance separating the RIS from the Tx/Rx is less than d_{lim}, then the RIS can be considered in the near-field. In this paradigm, the impinging spherical wave forms a circular and divergent phase gradient on the RIS surface. Accordingly, the RIS acts as an anomalous mirror and the two-hop link acts as a one-hop path. Hence, the distance path-loss is affected by the summation of the traveled distances, i.e., Tx-RIS and RIS-Rx distances, which is known as the specular reflection paradigm [11, 58, 76].

For a Tx-RIS (resp. RIS-Rx) distance $D \leq d_{\mathrm{lim}}$ and a large-sized RIS (LRIS), i.e., reflector units having size $10\lambda \times 10\lambda$ m^2, the minimum required number of reflectors for specular reflection, denoted N_{min}, can be calculated as

$$D = \frac{2A_t}{\lambda} = \frac{2N_{\mathrm{min}}\,(10\lambda)^2}{\lambda} = 200\lambda N_{\mathrm{min}} \Leftrightarrow N_{\mathrm{min}} = \frac{D}{200\lambda}. \tag{5.2}$$

The defined N_{min} will be later used to assess the feasibility of the RIS using the specular reflection paradigm.

In order to conduct the link budget analysis in this paradigm, we assume the Tx-Rx communication assisted by a building-mounted LRIS. Let $x(t)$ be the transmitted signal by the Tx. Then, the received (noise-free) signal at the Rx, denoted $y(t)$, can be written as [11]

$$y(t) = a\,x(t), \tag{5.3}$$

where a is the wireless channel coefficient, expressed for the sake of simplicity with the log-distance path-loss model. The latter is given by

$$a = \sqrt{P_t G_t G_r}\left(\frac{\lambda}{4\pi d_0}\right)\left(\left(\frac{d_0}{d_l}\right)^{\gamma} + \sum_{i=1}^{N} \frac{d_0^{\gamma}\rho_i e^{-j(\theta_i+\phi_i)}}{(d_{ti}+d_{ir})^{\gamma}}\right), \tag{5.4}$$

where P_t, G_t, and G_r are the transmit power and the transmitter and receiver gains, respectively. Also, d_0 denotes the reference distance, d_l is the distance between Tx and

[1] An example of (Tx,Rx) in the terrestrial environment is (BS,UE).

Rx,[2] $2\gamma = \alpha$ is the path-loss exponent, and N is the total number of RIS reflector units. Finally, ρ_i, d_{ti}, d_{ir} represent the reflection loss of the i^{th} RIS reflector, the distance between Tx and RIS i^{th} reflector, and distance between the RIS i^{th} reflector and Rx, respectively. Also, θ_i and ϕ_i are the corresponding incident and reflection angles. Subsequently, the received power at Rx, denoted P_r, can be written as

$$P_r = P_t G_t G_r \left(\frac{\lambda\, d_0^{(\gamma-1)}}{4\pi} \right)^2 \left(\frac{1}{d_l^{\gamma}} + \sum_{i=1}^{N} \frac{\rho_i e^{-j(\theta_i+\phi_i)}}{(d_{ti}+d_{ir})^{\gamma}} \right)^2 . \tag{5.5}$$

For the sake of simplicity, we assume here that the LRIS has the capability to perfectly adjust the desired phase shifts, and reflectors are ideal without any reflection losses i.e.[3],

$$\theta_i + \phi_i = 0 \text{ and } \rho_i = 1,\ \forall i = 1, \ldots, N. \tag{5.6}$$

Moreover, assuming that the variation of d_{ti} and d_{ir} is negligible across the RIS, we have

$$d_{ti} + d_{ir} \approx 2d,\ \forall i = 1, \ldots, N, \tag{5.7}$$

where $d = d_l/2$. Hence, the received power can be rewritten as

$$P_r = P_t G_t G_r \left(\frac{\lambda}{4\pi} \right)^2 \left(\frac{d_0^{(\alpha-2)}}{(2d)^{\alpha}} \right) (1+N)^2 . \tag{5.8}$$

According to (5.8), the path-loss exponent is the dominant factor (e.g., $\alpha \geq 3$ in urban environments [83]). Thus, in typical terrestrial environments, although the received power enhances quadratically with the number of RIS reflectors, it degrades at a much higher rate with the propagation distance.

5.2.2 The Scattering Reflection Paradigm

Assuming that the Tx-RIS and RIS-Rx distances are large, i.e., higher than d_{lim}, and that tiny RIS reflector units are used, i.e., of dimensions between 0.1λ and 0.2λ, then, each reflector capturing the transmitted signal behaves as a new signal source that re-scatters

[2] We assume here that the direct link Tx-Rx is a weak link [80].

[3] In practice, RIS reflection loss is dependent on the configuration technology and building materials [81, 67]. Also, since continuous phase shift implementation is difficult, only a finite discrete set of phase shifts is typically designed. It is shown that near-optimal RIS performances can be realized using a small number of phase-shift levels [82, 47]. In any case, the few dB losses due to the material properties or sub-optimal RIS configuration is insignificant compared to the signal propagation loss [80].

the signal towards the UE. In this paradigm, known as the scattering reflection paradigm, the total effect on the transmitted signal is the resultant of the cascaded individual channels Tx-RIS and RIS-Rx [77, 78, 79].

Typically, RIS-assisted communications under the scattering paradigm is presented as an alternative path to the degraded direct link due to strong blockages [73]. Accordingly, the effect of the direct link is ignored and the effective received signal is only the one scattered by the RIS. Since in this paradigm, the use of tiny RIS reflector units is advocated, we name the RIS by small-sized RIS (SRIS).

To accurately assess the SRIS-assisted terrestrial communications, we present next the link budget analysis for two channel models, namely the log-distance and 3GPP based models[4]

5.2.2.1 Log-distance Channel Model

For the i^{th} reflector unit of the SRIS, the channel effect of the received signal, denoted a_i, is resulting from two cascaded channels, i.e., Tx-i^{th} reflector and i^{th} reflector-Rx [77, 78]. The channel coefficient is given by

$$a_i = \sqrt{P_t G_t G_r} h_{ti} g_{ir} \rho_i e^{-j\phi_i},\ i = 1, \ldots, N, \tag{5.9}$$

where ϕ_i is the adjusted phase shift of the reflector, while h_{ti} and g_{ir} are the complex-valued coefficients representing the links between the i^{th} reflector and both Tx and Rx. The latter are defined by

$$h_{ti} = \left(\frac{\lambda}{4\pi d_0}\right)\left(\frac{d_0}{d_{ti}}\right)^{\gamma} e^{j\theta_{ti}}, \text{ and } g_{ir} = \left(\frac{\lambda}{4\pi d_0}\right)\left(\frac{d_0}{d_{ir}}\right)^{\gamma} e^{j\theta_{ir}}, \tag{5.10}$$

with θ_{ti} and θ_{ir} denoting the transmit and receive channel phases, respectively. Following the generalization to the N reflectors, the received power can be expressed by

$$P_r = P_t G_t G_r \left(\frac{\lambda}{4\pi d_0}\right)^4 d_0^{(2\alpha)} \left(\sum_{i=1}^{N} \frac{\rho_i e^{-j(\phi_i - \theta_{ti} - \theta_{ir})}}{(d_{ti} d_{ir})^{\gamma}}\right)^2. \tag{5.11}$$

We assume lossless reflectors, i.e.,

$$\rho_i = 1, \forall i = 1, \ldots, N, \tag{5.12}$$

[4]Recently, several researchers raised practical concerns about the specular reflection paradigm and the use of LRIS [67, 84]. Subsequently, we adopt the practical 3GPP channel model under the scattering reflection paradigm only.

and that

$$d_t \approx d_{ti} \text{ and } d_r \approx d_{ir}, \forall i = 1, \dots, N, \tag{5.13}$$

where d_t and d_r are reference distances measured between the center of the SRIS and the Tx and Rx, respectively. Subsequently, the received power can be maximized by coherently combining the received signals through the N reflectors, i.e., $\phi_i = \theta_{ti} + \theta_{ir}$. Hence, the received power can be written as

$$P_r = P_t G_t G_r \left(\frac{\lambda}{4\pi}\right)^4 \left(\frac{d_0^{(2\alpha-4)}}{(d_t d_r)^\alpha}\right) N^2. \tag{5.14}$$

According to (5.14), P_r degrades faster with path-loss than in (5.8), due to the distances multiplication. Also, P_r is maximized when the RIS is the closest to either Tx or Rx.

5.2.2.2 3GPP Channel Model

RIS in terrestrial environments can be placed on facades of buildings to smartly reflect signals toward users. Since such smart buildings are expected to be available in modern urbanized environments, we assume in the following the urban scenario of the 3GPP standard model [85][5]. The total path-loss for the Tx-SRIS and SRIS-Rx links can be written as

$$PL = \mathcal{P}^{\text{LoS}} PL^{\text{LoS}} + \mathcal{P}^{\text{NLoS}} PL^{\text{NLoS}} + PL_e, \tag{5.15}$$

where $\mathcal{P}^{\text{LoS}}$ and $\mathcal{P}^{\text{NLoS}}$ are the LoS and NLoS probabilities, PL^{LoS} and PL^{NLoS} are the associated losses in the LoS and NLoS conditions, and PL_e accounts for the extra loss of indoor users. The latter exhibits a great variability with the building type, location within the building, and movement in the building. For PL_e accurate calculation, we refer the reader to [86]. Nevertheless, we focus in our system on outdoor users, hence, PL_e is ignored.

The LoS probability in a terrestrial environment between the SRIS and Tx or Rx, assuming that the heights of the RIS-equipped building and Rx are below 13 m, can be given by [85, Table 7.4.2-1]

$$\mathcal{P}^{\text{LoS}} = \begin{cases} 1 & \text{if } \mathrm{d_{2D}} \leq 18\text{m} \\ \frac{18}{d_{2D}} + \exp\left(-\frac{d_{2D}}{63}\right)\left(1 - \frac{18}{d_{2D}}\right) & \text{if } \mathrm{d_{2D}} > 18\text{m}, \end{cases} \tag{5.16}$$

[5]Practically, RIS is expected to be implemented where it would bring profit to service providers. Due to high density of customers in urban areas, it is more likely that RIS will be deployed massively in the urban environment, and may be rarely or never be used in rural environments.

where d_{2D} is the 2D separating distance (projected on the ground) between the SRIS and the Tx or Rx, whereas the path-loss for LoS and NLoS links are given as follows [85, Table 7.4.1-1]:

$$PL^{\mathrm{LoS}} = 28 + 22\log(d_{3D}) + 20\log(f) + X \tag{5.17}$$

and

$$PL^{\mathrm{NLoS}} = \max(PL^{\mathrm{LoS}}, \bar{PL}^{\mathrm{NLoS}}) \tag{5.18}$$

where

$$\begin{aligned}\bar{PL}^{\mathrm{NLoS}} &= 13.54 + 39.08\log(d_{3D}) + 20\log(f) \\ &- 0.6\,(H_x - 1.5) + X,\ x \in \{\mathrm{RIS}, \mathrm{Rx}\},\end{aligned} \tag{5.19}$$

d_{3D} is the 3D Tx-SRIS or SRIS-Rx separation distance in meters, f is the carrier frequency in GHz, X is a log-normal random variable denoting the shadow fading, with standard deviation $\sigma = 4$ dB and $\sigma = 7.8$ dB for LoS and NLoS links, respectively, and H_x denotes the SRIS/Rx height. Specifically, for the Tx-SRIS link, $H_x = H_{RIS}$, where H_{RIS} is the height of the building coated with the RIS, while for the SRIS-Rx link, $H_x = H_{Rx}$, with H_{Rx} is the Rx height.

Accordingly, the received power, in dBm, can be written as

$$P_r = P_t + G_t + G_r - PL_{Tx-SRIS} - PL_{SRIS-Rx} + 20\log(N), \tag{5.20}$$

where $PL_{Tx-SRIS}$ and $PL_{SRIS-Rx}$ are the path-losses for the Tx-SRIS and SRIS-Rx links, calculated using (5.15).

5.3 Link Budget Analysis for RIS-Assisted Non-Terrestrial Networks

In this section, we start by presenting the aerial platforms characteristics. Then, we derive the link budget analysis of RIS-enabled non-terrestrial communications, i.e., when RIS is mounted on an aerial platform, such as a UAV, a HAPS, or a LEO satellite. Given the identified specular and scattering reflection paradigms, we derive the related received power expressions.

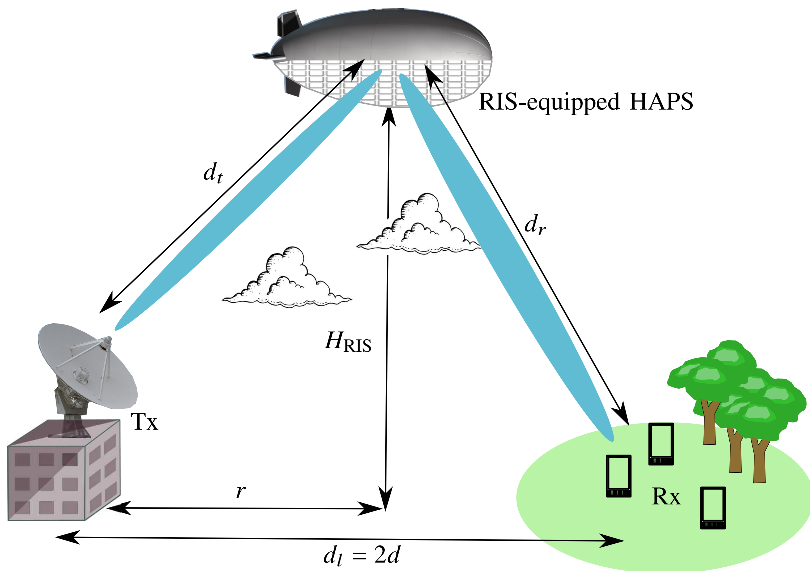

Figure 5.2: System model of an aerial platform equipped with RIS.

5.3.1 Aerial Platforms Characteristics

Three types of aerial platforms are advocated to host the RIS technology, namely, UAVs, HAPS and LEO satellites. These platforms are usually deployed at different altitudes and target different coverage areas. Specifically, UAVs are deployed around 100 m altitude (and can operate up to 300 m [87]), to serve an area below 5 km radius [15, 88]. On the other hand, HAPS are quasi-stationary platforms positioned in the stratosphere at an altitude between 17 and 50 km. However, most HAPS projects are targeting the 20 km altitude due to its preferred atmospheric characteristics for the platform stability and communication quality [3]. Thus, HAPS has a much wider footprint than UAVs, that spans from 40 to 100 km for high throughput [3, 89] and can go up to 500 km according to the International Telecommunications Union (ITU) [90]. Finally, LEO satellites orbit around the Earth at an altitude between 400 and 2000 km, with an orbital period between 88 and 127 minutes [7]. Accordingly, LEO satellites have the largest coverage footprint. Nevertheless, the coverage area significantly depends on the satellite's altitude, the elevation angle, and the coverage scheme, .i.e, whether it is using a spot or a wide communication beam. Consequently, the LEO satellite's footprint has a radius between hundreds and thousands of kilometers [91, 92, 93]. To communicate with UAVs and HAPS, a UE can use the same device as to communicate with the terrestrial BS. However, a different equipment is needed to communicate with LEO satellites, since it requires LEO tracking, either mechanically or electronically, in order to compensate for the satellite motion and achieve a reliable communication [7].

In addition to the aforementioned characteristics, the physical size of the aerial platform is crucial to enable hosting the RIS. UAVs have the smallest size, and hence can dedicate only a small area for RIS. On the other hand, two types of HAPS are identified, namely the aerostatic HAPS and the aerodynamic HAPS. Aerostatic airships are giant platforms and their length is typically between 100 and 200 m, whereas aerodynamic HAPS have a wingspan between 35 and 80 m [3]. Finally, the size of current LEO satellites is less than 10 m [94, 95]. Since HAPS and LEO satellites are typically equipped with arrays of solar panels, a part of the platform surface can be used to mount an RIS equipment.

5.3.2 The Specular Reflection Paradigm

When the Tx and Rx[6] are separated by a relatively long distance, an aerial platform equipped with a LRIS can be used to assist the communication. Specifically, the Tx transmits its signal to the LRIS-equipped aerial platform. Then, the LRIS smartly reflects the incident signal towards the Rx, as illustrated in Fig. 5.2. Hence, the received noise-free signal in the specular paradigm is identical to the one in (5.3), whereas the channel effect is expressed using the free-space path-loss formula as

$$a = \sqrt{P_t G_t G_r} \left(\frac{\lambda}{4\pi} \right) \sum_{i=1}^{N} \frac{\rho_i e^{-j(\theta_i + \phi_i)}}{d_{ti} + d_{ir}}, \tag{5.21}$$

where the LoS wireless link component is predominant, i.e., the path-loss exponent $\alpha = 2\gamma = 2$. By following the same assumptions as in (5.12)–(5.13) and adopting a similar phase shift configuration as in (5.6), the received power can be given by

$$P_r = P_t G_t G_r \left(\frac{\lambda}{4\pi} \right)^2 \frac{N^2}{(d_t + d_r)^2}. \tag{5.22}$$

Unlike (5.8), the parameters λ, N, and $(d_t + d_r)$ have the same scaling law for the received power improvement or degradation.

One of the distinct features of aerial platforms compared to terrestrial networks is their placement flexibility that allows to optimize the system's performance.

[6]Notice that Tx and Rx in the non-terrestrial communication context can be different according to the used aerial platform. For instance, (Tx, Rx) can be (BS, UE) for a UAV, or it can be (Gateway, UE) for a HAPS platform or a LEO satellite. A HAPS UE might be a mobile, vehicular or fixed cellular user device, whereas LEO has a fixed UE such as a household receiver [63].

Proposition 1. *Given that Tx and Rx are collinearly separated by distance* $d_l = 2d$, *and that the aerial platform is located at altitude* H_{RIS} *and horizontally separated from the Tx by a distance* r, *i.e.,* $d_t = \sqrt{H_{RIS}^2 + r^2}$ *and* $d_r = \sqrt{H_{RIS}^2 + (2d - r)^2}$, *then, the optimal placement of the aerial platform under specular reflection is given by*

$$r^* = d, \tag{5.23}$$

i.e., the platform is placed over the perpendicular bisector of the segment Tx-Rx at altitude H_{RIS}.

Proof. The specular equivalent path-loss distance, denoted d_{sp}, can be written as

$$d_{sp} = d_t + d_r = \sqrt{(H_{RIS}^2 + r^2)} + \sqrt{H_{RIS}^2 + (2d - r)^2}. \tag{5.24}$$

To maximize P_r, we need to minimize d_{sp} through nulling its first derivative, i.e,

$$\frac{\partial d_{sp}}{\partial r} = \frac{r}{\sqrt{r^2 + H_{RIS}^2}} - \frac{2d - r}{\sqrt{(2d - r)^2 + H_{RIS}^2}} = 0, \tag{5.25}$$

from which we obtain $r^* = d$. When substituting this solution in the second derivative of d_{sp}, $\frac{\partial^2 d_{sp}}{\partial r^2}$, we get

$$\begin{aligned} \frac{\partial^2 d_{sp}}{\partial r^2} &= \frac{H_{RIS}^2 \left((r^2 + H_{RIS}^2)^{\frac{3}{2}} + \left((2r - r)^2 + H_{RIS}^2 \right)^{\frac{3}{2}} \right)}{\left((2d - r)^2 + H_{RIS}^2 \right)^{\frac{3}{2}} (r^2 + H_{RIS}^2)^{\frac{3}{2}}} \\ &\overset{(r=d)}{=} \frac{2H_{RIS}^2}{(d^2 + H_{RIS}^2)^{\frac{3}{2}}}. \end{aligned} \tag{5.26}$$

Since $\frac{\partial^2 d_{sp}}{\partial r^2} > 0$, then $r^* = d$ is the optimal value that minimizes d_{sp}. □

Accordingly, the maximal received power can be calculated using (5.22) for $r^* = d$ as follows:

$$P_r^* = P_t G_t G_r \left(\frac{\lambda}{4\pi} \right)^2 \frac{N^2}{4(H_{RIS}^2 + d^2)}. \tag{5.27}$$

5.3.3 The Scattering Reflection Paradigm

Similarly to Section III, the scattering reflection paradigm is investigated for two channel models, namely the log-distance and the 3GPP models.

5.3.3.1 Log-distance Channel Model

Similarly to the SRIS-assisted terrestrial network, the received power at the Rx in the scattering paradigm can be expressed using (5.14) for $\alpha = 2$, i.e.,

$$P_r = P_t G_t G_r \left(\frac{\lambda}{4\pi}\right)^4 \left(\frac{N}{d_t d_r}\right)^2. \tag{5.28}$$

Unlike the specular paradigm where the optimum aerial platform location is over the perpendicular bisector of segment Tx-Rx, the best platform location under the scattering paradigm is expected to be different due to the cascaded channel effect.

Proposition 2. *Given that Tx and Rx are collineraly separated by distance $d_l = 2d$, and that the aerial platform is located at altitude H_{RIS} and horizontally separated from Tx by a distance r, then, the optimal placement of the aerial platform under scattering reflection is given by*

$$r^* = \begin{cases} d \pm \sqrt{d^2 - H_{RIS}^2} & \text{if } d \geq H_{RIS} \\ d & \text{otherwise.} \end{cases} \tag{5.29}$$

Proof. The scattering equivalent path-loss distance, denoted d_{sc}, can be expressed through

$$d_{sc}^2 = (d_t d_r)^2 = \left(H_{RIS}^2 + r^2\right)\left(H_{RIS}^2 + (2d - r)^2\right). \tag{5.30}$$

To maximize P_r, it is required to minimize d_{sc}^2 by nulling its first derivative as follows:

$$\frac{\partial d_{sc}^2}{\partial r} = 4r^3 - 12dr^2 + \left(8d^2 + 4H_{RIS}^2\right) r - 4dH_{RIS}^2 = 0. \tag{5.31}$$

By solving (5.31), we obtain the follwing roots:

$$r^* = \begin{cases} d + \sqrt{d^2 - H_{RIS}^2} \\ d - \sqrt{d^2 - H_{RIS}^2} \\ d. \end{cases} \tag{5.32}$$

The second derivative is given by

$$\frac{\partial^2 d_{sc}^2}{\partial r^2} = 12r^2 - 24dr + 8d^2 + 4H_{RIS}^2, \tag{5.33}$$

in which we substitute the roots of (5.32). Consequently, we find that (5.33) is positive only when $\{r = d \text{ and } d \leq H_{RIS}\}$ or $\{r = d \pm \sqrt{d^2 - H_{RIS}^2} \text{ and } d \geq H_{RIS}\}$. These (r, d) values dictate the best aerial platform locations that provide the maximal received power. □

Physically speaking, Proposition (2) implies that under the scattering reflection paradigm, when the height of a platform is larger than its designed coverage radius, the platform should be placed in the mid-point between the Tx and Rx. However, when the targeted coverage radius is larger than the platform's height, two optimal locations can be used, which are being close to either the Tx or the Rx.

By substituting the result of (5.32) in (5.30) then (5.28), the received power at Rx can be written as

$$P_r^* = P_t G_t G_r \left(\frac{\lambda}{4\pi}\right)^4 \frac{N^2}{(d_{sc}^*)^2}. \tag{5.34}$$

where d_{sc}^* is the equivalent path-loss distance for the optimal platform location, given by

$$d_{sc}^* = \begin{cases} H_{RIS}^2 + d^2 & \text{if } d \leq H_{RIS} \\ 2H_{RIS}d & \text{otherwise.} \end{cases} \tag{5.35}$$

Unlike (5.22), the impact of H, d, and λ, is more important than N in (5.34), due to the scattering effect.

5.3.3.2 3GPP Channel Model

For a fair comparison with RIS-assisted terrestrial communications, we investigate here the link budget analysis for RIS-enabled aerial platforms with realistic 3GPP channel models. In what follows, given that platforms operate at different altitudes and thus may experience different attenuation phenomena, we study separately the link budget for RIS-equipped UAV, and for RIS-equipped HAPS or LEO satellite.

- **The UAV-based Model:**

The RIS-enabled UAV is envisioned to cooperate with terrestrial BSs to support terrestrial users. It can tackle the coverage holes problem or increase the capacity of terrestrial users by reflecting the BSs' signals towards users [69]. In such context, it is acceptable to consider the 3GPP channel model between terrestrial BSs and UAVs [87]. Due to the relatively low altitude of UAVs, the latter are generally assumed in full LoS conditions. Consequently, the path-loss in rural and urban environments[7] can be given by [87, Table

[7] In contrast to RIS-assisted terrestrial communications where RIS deployment is expected to be concentrated in urban areas, RIS-equipped aerial platforms have the necessary flexibility to be utilized in both urban and rural areas.

B-2]

$$
\begin{aligned}
PL^{\text{rural}} &= \max\left[23.9 - 1.8\log_{10}(H_x), 20\right]\log_{10}(d_{3D}) \\
&+ 20\log_{10}(\frac{40\pi f}{3}) + X, \;\; x \in \{\text{UAV}, \text{UE}\}
\end{aligned} \tag{5.36}
$$

and

$$
PL^{\text{urban}} = 28 + 22\log_{10}(d_{3D}) + 20\log_{10}(f) + X, \tag{5.37}
$$

where H_x, d_{3D}, f, and X are defined as in (5.17)–(5.19), except that X has a log-normal distribution with standard deviation given by

$$
\sigma = \begin{cases} 4.2\ e^{(-0.0046\ H_x)} & \text{in rural environment,} \\ 4.64\ e^{(-0.0066\ H_x)} & \text{in urban environment.} \end{cases} \tag{5.38}
$$

Subsequently, the received power in dBm can be expressed by

$$
P_r = P_t + G_t + G_r - PL_{Tx-UAV} - PL_{UAV-Rx} + 20\log(N), \tag{5.39}
$$

where PL_{Tx-UAV} and PL_{UAV-Rx} are the path-losses for the Tx-UAV and UAV-Rx links, calculated using either (5.36) or (5.37), depending on the considered environment.

- **The HAPS/LEO based Model:**

The support of future wireless networks through HAPS and LEO satellites is envisioned for both rural and urban areas [3, 6]. To assess the performance under these different environments, the LoS probability is required. Based on the elevation angle of the aerial platform regarding the terrestrial Tx or Rx, denoted ϑ, the LoS probability can be estimated for different environments using [7, Table 6.6.1-1]. For the sake of simplicity and convenience, we propose to substitute [7, Table 6.6.1-1] by a LoS probability function, defined as

$$
\mathcal{P}^{LoS} = b_1\vartheta^{b_2} + b_3, \tag{5.40}
$$

where b_i, $i = \{1, 2, 3\}$ are parameters that depend on the environment, and are determined in Table 5.1. The accuracy of (5.40) is validated in Fig. 5.3, where it is shown to agree with the results of [7, Table 6.6.1-1]. Subsequently, the path loss in LoS and NLoS conditions, denoted PL, can be written as

$$
PL = \mathcal{P}^{\text{LoS}} PL^{\text{LOS}} + \mathcal{P}^{\text{NLoS}} PL^{\text{NLOS}}, \tag{5.41}
$$

Table 5.1: Parameters of HAPS/LEO LoS probability model (5.40)

Parameter	Dense Urban	Urban	Rural
b_1	0.04235	9.668	-99.95
b_2	1.644	0.547	-0.5895
b_3	27.32	-10.58	104.1

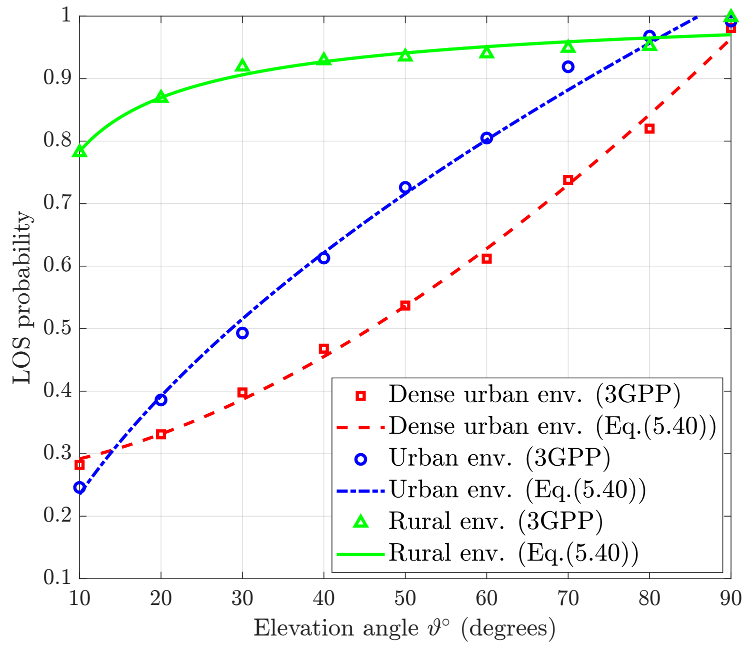

Figure 5.3: LoS probability of HAPS/LEO vs. elevation angle (different environments).

where $\mathcal{P}^y$ and PL^y, $y \in \{\mathrm{LoS}, \mathrm{NLoS}\}$, are defined as in (5.15). The signal path between a HAPS/LEO and a terrestrial Tx or Rx undergoes several stages of propagation and attenuation. Specifically, the path losses PL^y, $y \in \{\mathrm{LoS}, \mathrm{NLoS}\}$, are composed as follows [7]:

$$PL^y = PL_b^y + PL_g + PL_s + PL_e, y \in \{\mathrm{LoS}, \mathrm{NLoS}\}, \tag{5.42}$$

where PL_b^y is the basic path loss, PL_g is the attenuation due to atmospheric gasses, PL_s is the attenuation due to either ionospheric or tropospheric scintillation, and PL_e is the building entry loss, expressed in dB.

PL_b^y accounts for the signal's free-space propagation ($FSPL$), clutter loss (CL^y), and shadow fading (X^y), i.e.,

$$PL_b^y = FSPL + CL^y + X^y,\ y \in \{\mathrm{LoS}, \mathrm{NLoS}\}, \tag{5.43}$$

Table 5.2: Average clutter loss and shadow fading standard deviation in the Ka-band

Parameter	Dense Urban	Urban	Rural
CL^{NLoS}	38.6	38.6	23.15
σ^{LoS}	1.75	4	1.15
σ^{NLoS}	14.7	6	10.75

where

$$FSPL = 32.45 + 20\log_{10}(f) + 20\log_{10}(d_{3D}), \tag{5.44}$$

with d_{3D} is the 3D distance between the HAPS/LEO and the terrestrial Tx or Rx, expressed as a function of the HAPS/LEO altitude H_z, $z \in \{\text{HAPS}, \text{LEO}\}$ and the platform's elevation angle ϑ as follows:

$$d_{3D} = \sqrt{R_E^2 \sin^2(\vartheta) + H_z^2 + 2H_z R_E} - R_E \sin(\vartheta), \tag{5.45}$$

where R_E denotes the Earth radius. The clutter loss, CL^y, represents the attenuation caused by buildings and environmental objects. Its value depends on ϑ, f, and the environment type. In LoS conditions, $CL^{\text{LoS}} = 0$, while for NLoS, the CL^{NLoS} values of [7, Tables 6.6.2-1 to 6.6.2-3] can be used for the typical Ka spectrum band, i.e., between 26.5 and 40 GHz. Finally, X^y is a log-normal distribution with standard deviation σ^y, $y \in \{\text{LoS}, \text{NLoS}\}$, which values are determined in [7, Tables 6.6.2-1 to 6.6.2-3]. For the sake of simplicity, we present the average parameters values in Table 5.2.

PL_g is the attenuation caused by absorption due to atmospheric gases. Its value depends mainly on f, ϑ, and d_{3D}. According to [7], the atmospheric gases effect is negligible for $f \leq 10$ GHz. However, for higher frequency bands that are suitable for the RIS operation with a large number of reflectors, the selection of frequency windows with minimum atmospheric effect is important. In addition to the aforementioned factors, PL_g depends on the dry air pressure p, water-vapour density ξ, and temperature T [96]. An illustrative example is shown in Fig. 5.4 for different Tx-Rx link lengths, selected for typical distances between HAPS and Tx or Rx (20 and 100 km) and between a LEO satellite and Tx or Rx (1000 km). The related parameters (p, ξ and T) are selected based on the mean annual global reference atmosphere, i.e., $p = 101300$ Pa, $\xi = 7.5 g/m^3$, and $T = 15°$C [97]. The PL_g calculation is carried out using the steps detailed in [96].

Finally, the scintillation loss PL_s is caused by rapid fluctuations of the received signal amplitude and phase. There are two types of scintillation losses, namely the ionospheric

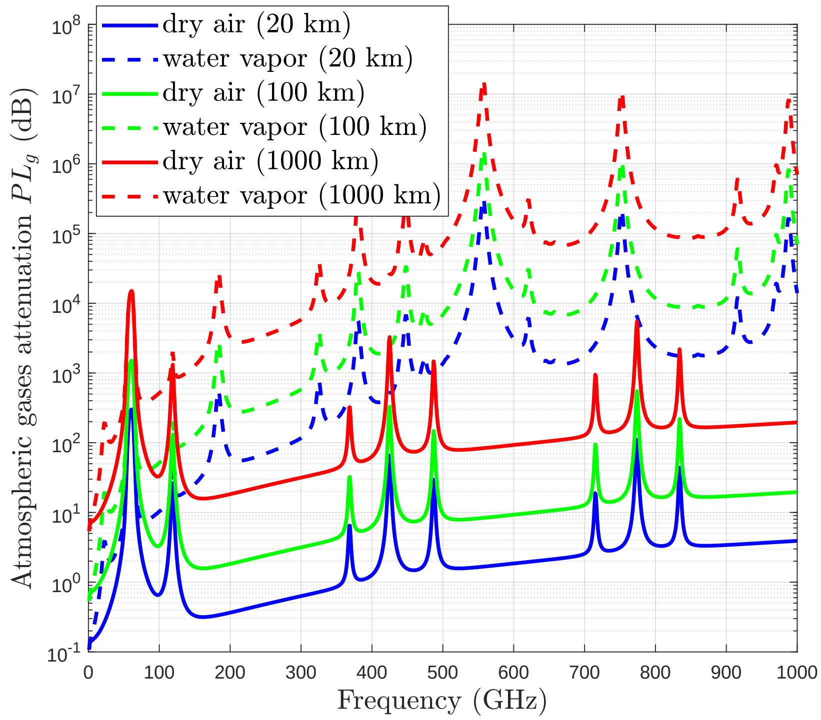

Figure 5.4: Attenuation due to atmospheric gases PL_g vs. frequency (different path lengths).

scintillation and the tropospheric scintillation. The former has only significant disruptions for signals at frequencies below 6 GHz, whereas the latter affects only signals in frequencies above 6 GHz. The impact of the ionospheric scintillation is only significant for latitudes ranging in $[-20^{\circ}, 20^{\circ}]$, and ignored elsewhere [7]. It can be calculated as detailed in [98]. Specifically, the ionospheric scintillation is derived from the measured peak-to-peak fluctuation as follows:

$$PL_s = \frac{PF}{\sqrt{2}}, \tag{5.46}$$

where PF is the peak-to-peak fluctuation, equal to 1.1 dB for $f = 4$ GHz, and calculated by the following equation for $f \leq 6$ GHz:

$$PF_{(f \leq 6 \text{ GHz})} = PF_{(f=4 \text{ GHz})} \cdot (f/4)^{-1.5}. \tag{5.47}$$

Since high frequency bands are advocated for the RIS-enabled HAPS/LEO platforms, tropospheric scintillation is taken into account in the path-loss model. Specifically, the wireless signal fluctuations are due to sudden changes in the refractive index caused by temperature, water vapor content, and barometric pressure variations. Also, low elevation angles (especially below 5°) are significantly affected by the scintillation loss, due to the

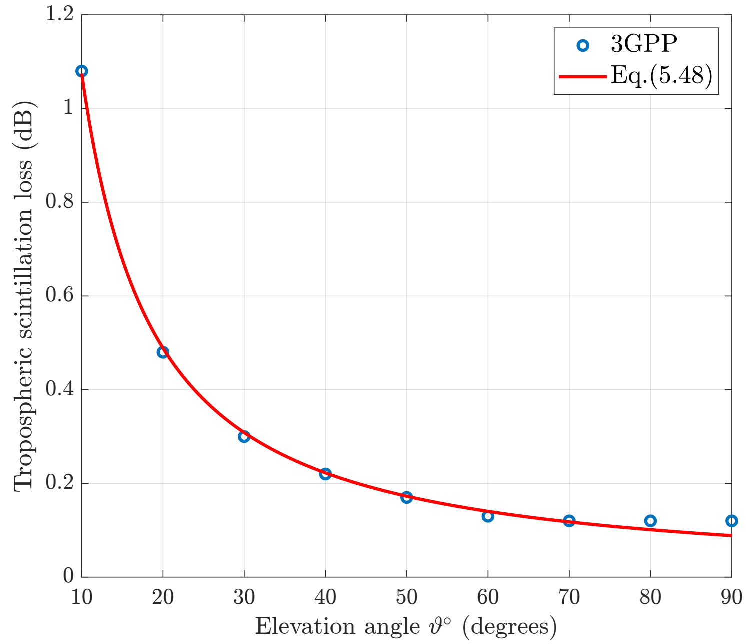

Figure 5.5: Scintillation loss PL_s vs. elevation angle.

longer path of the signal and wider beam width. The value of the tropospheric scintillation loss is seasonal and regional dependent. We refer the reader to [99] for the detailed calculation steps. As an illustrative example of typical power attenuation level, the tropospheric attenuation with 99% probability at 20 GHz in Toulouse, France is tabulated in [7, Table 6.6.6.2.1-1] for different elevation angles. For the sake of simplicity, we model the related tropospheric scintillation loss by

$$PL_s = 14.7\,\vartheta^{(-1.136)},\ \vartheta \in [0^\circ, 90^\circ], \tag{5.48}$$

which is a valid approximation of [7, Table 6.6.6.2.1-1] as shown in Fig. 5.5.

Subsequently, the received power in dBm at Rx can be expressed by

$$\begin{aligned} P_r &= P_t + G_t + G_r - PL_{Tx-H_L} - PL_{H_L-Rx} \\ &+ 20\log(N),\ H_L \in \{HAPS, LEO\}, \end{aligned} \tag{5.49}$$

where PL_{Tx-H_L} and PL_{H_L-Rx} are calculated using (5.41).

The link budget analysis of Section III is summarized in Table 5.3 below.

Table 5.3: Link Budget Summary

Scenario	Size of RIS reflector	Channel Model	Link Budget	Dominant parameter(s)
LRIS-assisted terrestrial communication (Specular paradigm)	$10\lambda \times 10\lambda$	Log-distance	Eq. (5.8)	d, λ and N (for $\alpha = 2$) d (for $\alpha > 2$)
SRIS-assisted terrestrial communication (Scattering paradigm)	$[0.1\lambda \times 0.1\lambda, 0.2\lambda \times 0.2\lambda]$	Log-distance	Eq. (5.14)	λ (for $\alpha < 4$) λ, d_t, and d_r (for $\alpha = 4$)
		3GPP	Eq. (5.20)	f
LRIS-assisted non-terrestrial communication (Specular paradigm)	$10\lambda \times 10\lambda$	Log-distance	Eq. (5.27)	λ, N, H_{RIS} and d
SRIS-assisted non-terrestrial communication (Scattering paradigm)	$[0.1\lambda \times 0.1\lambda, 0.2\lambda \times 0.2\lambda]$	Log-distance	Eq. (5.34)	λ
		3GPP (UAV)	Eq. (5.39)	f
		3GPP (HAPS/LEO)	Eq. (5.49)	f

Table 5.4: Typical parameters of different types of platforms.

Platform	**Altitude** (H_{RIS})	**Coverage radius** (d)	**RIS area** (A_t)
Terrestrial	5 m	0.5 km	5×10 m^2
UAV	200 m	2 km	0.25×0.25 m^2
HAPS	20 km	50 km	40×20 m^2
LEO	500 km	500 km	5×10 m^2

5.4 Results and Discussion

In this section, we evaluate the received power for different RIS-mounted platforms, and the impact of several parameters is investigated. Based on the unique features of each platform, as discussed in Sections II and III, we assume typical values of altitude, coverage radius, and RIS area for each platform, as shown in Table 5.4. Moreover, we consider the height of the terrestrial Tx $H_{\text{Tx}} = 25$ m, while the receiver's height is $H_{\text{Rx}} = 1.5$ m.

5.4.1 Impact of the Number of Reflectors and Environment Type

Given the selected platform, the type of mounted RIS reflectors is of great concern, since different communication paradigms can be followed, with different costs. According to [78], the cost is expected to be approximately proportional to the RIS size and number of RIS reflector units. Consequently, larger reflectors, with dimensions above $10\lambda \times 10\lambda$ and operating in the specular reflection paradigm, are more expensive than small reflectors, i.e., with dimensions lower than $0.2\lambda \times 0.2\lambda$, thus operate in the scattering reflection paradigm. Hence, the maximal number of reflectors to install on a platform, denoted $N_{\max}$, is limited by the reserved area on the platform for the RIS A_t and the reflector's size $A_r = c_1\lambda \times c_2\lambda$, where $c_1\lambda > 0$ and $c_2\lambda > 0$ are the length and width of a reflector unit, respectively. Their relation is defined by

$$N_{\max} = \frac{A_t}{A_r} = \frac{A_t}{c_1 c_2 \lambda^2}. \tag{5.50}$$

In order to emphasize the potential gains of using RIS-equipped platforms, we consider that a communication between a terrestrial Tx and a terrestrial Rx is assisted by an RIS-equipped platform, namely a building facade, a UAV, a HAPS, or a LEO satellite, characterized as in Table 5.4. For the sake of simplicity, we assume that Tx and Rx are located at the edges of the platform's coverage footprint, i.e., within a distance $2d$. Moreover, due to the flexibility of aerial platforms, we assume that they are placed at the optimal location according to the considered reflection paradigm, while the terrestrial RIS is assumed at the middle point between Tx and Rx[8]. The operating frequency $f = \lambda/c = 30$ GHz (Ka-band), where c is the light's velocity in m/s, the receive antenna gain $G_r = 1$ (i.e., 0 dBi), and the path-loss $\alpha = 4$ for the terrestrial communication. Finally, the following transmit/receive parameters are set as follows for the log-distance channel model: Transmit power $P_t = 40$ dBm and transmit antenna gain $G_t = 1$ (i.e., 0 dBi). For the 3GPP model, P_t and G_t are fixed according to the related standards. Specifically, for the terrestrial and UAV systems, we assume that $P_t = 35$ dBm and $G_t = 8$ dBi [85], while for the HAPS and LEO systems, we set $P_t = 33$ dBm and $G_t = 43.2$ dBi [7].

Given the specular reflection paradigm, Fig. 5.6 presents the received power as a function of the number of reflectors, for different platforms. We notice that for UAVs and LEO satellites, the minimum required number of reflectors for specular reflection is larger than the maximum number of reflectors that can be placed on the platform's surface. Therefore, specular reflection cannot be achieved for RIS-equipped UAVs and LEO satellites for the specified coverage areas. This is due to the limited available RIS area over UAVs and to the relatively high operating altitude of LEO satellites. However, specular reflection can be realized using RIS-equipped HAPS or terrestrial environments. Indeed, this is realizable due to the clear LoS links to/from the HAPS, and to the relatively short communication distances in terrestrial environments. As it can be seen, $N_{\min} = 27,000$ reflectors for HAPS provides coverage in a 100 km circular area at $P_r = -64$ dBm. For

[8]This assumption for the terrestrial RIS is justified by the fact that the latter cannot be moved over time to be placed at a more adequate location, given that Tx and Rx locations may change.

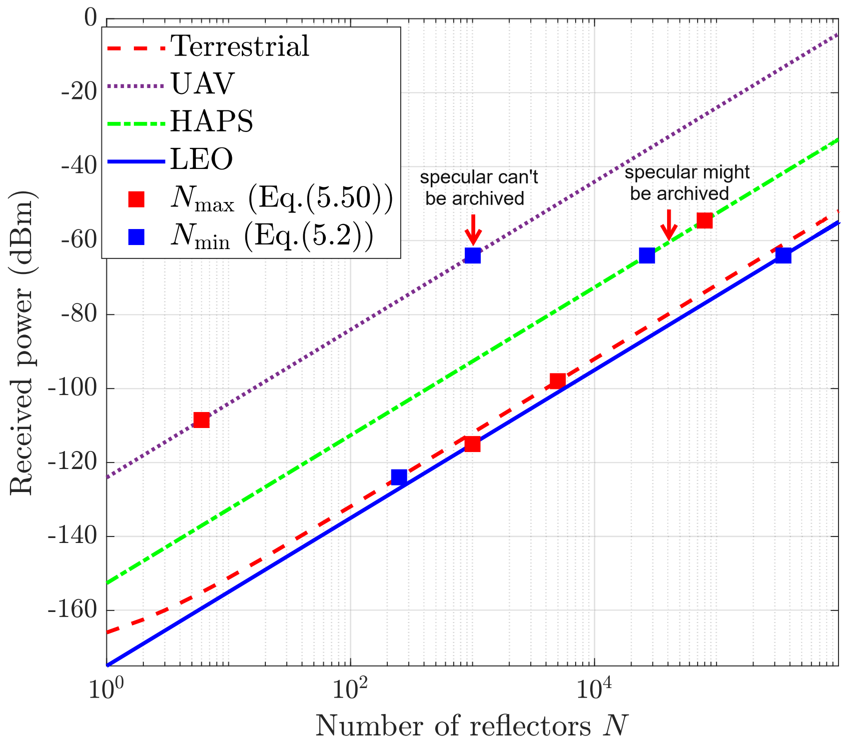

Figure 5.6: Received power vs. number of reflectors (different platforms; specular reflection paradigm).

a smaller coverage footprint, it is expected that a lower number of reflectors is used. Although a small number of reflectors is required in the terrestrial environment for the specular reflection, the received power is worse than in the HAPS scenario. This is due to degraded terrestrial communication channels, compared to LoS wireless links for the RIS-equipped HAPS. Accordingly, HAPS is the preferred RIS mounting platform in the specular reflection paradigm.

For the scattering reflection paradigm, we present in Fig. 5.7 the received power as a function of the number of reflectors, for different platforms. For readability purposes, we show only the results corresponding to the 3GPP channel models where different types of environments are studied, namely dense urban, urban, and rural. Given the same number of reflectors, the RIS-equipped UAV system achieves the best power performance due to short distances and cleared LoS wireless links. Moreover, the related performance gap between the rural and urban environments is very small, of about 2 dB. For a number of reflectors close or equal to $N_{\max}$, the LEO system has the worst received power performance, which significantly degrades for more urbanized environments. In contrast, the HAPS system realizes the best P_r values for a number of reflectors near or equal to $N_{\max}$. This is valid

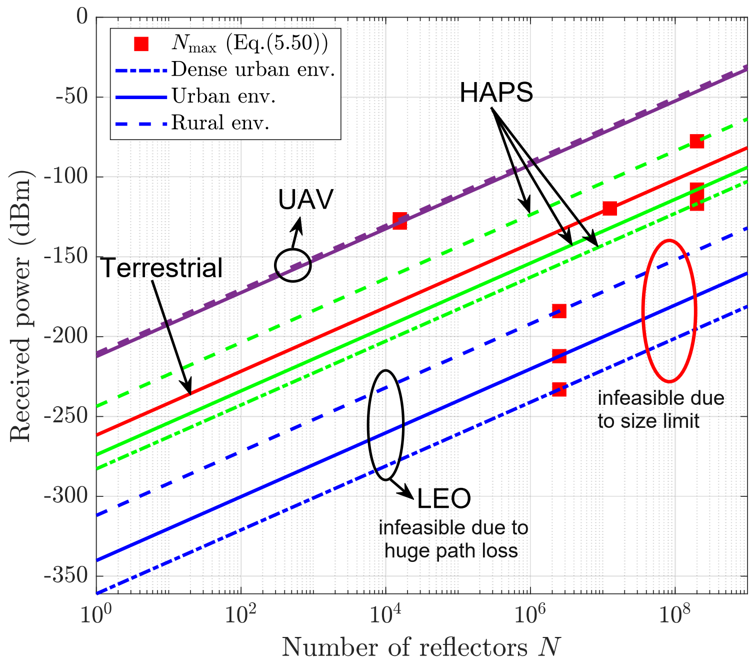

Figure 5.7: Received power vs. number of reflectors (different platforms and environment types; scattering reflection paradigm).

even when the environment becomes densely urbanized, despite a noticeable HAPS system performance degradation that the latter may compensate using a higher number of RIS reflectors or by reducing its coverage footprint, i.e., Tx and Rx are closer. Consequently, it is interesting to highlight that the RIS-equipped LEO system may require further redesign in order to be feasible, while the HAPS coverage footprint needs to be adjusted according to the environment type of the served area.

5.4.2 Impact of the Carrier Frequency

As shown in Table 5.3, the carrier frequency is a dominant parameter in the link budget analysis. Although using higher frequencies enables high capacity links and addresses the spectrum scarcity issues, these frequencies, such as millimeter wave and terahertz, may suffer from an important signal attenuation. Nevertheless, high frequencies enable designing small-sized reflectors, which can be integrated in a very large number to small areas. Eventually, the large number of reflectors may thwart the signal attenuation.

In Fig. 5.8, we evaluate the received power as a function of the carrier frequency, for the same communication model introduced previously. Here, we assume that each plat-

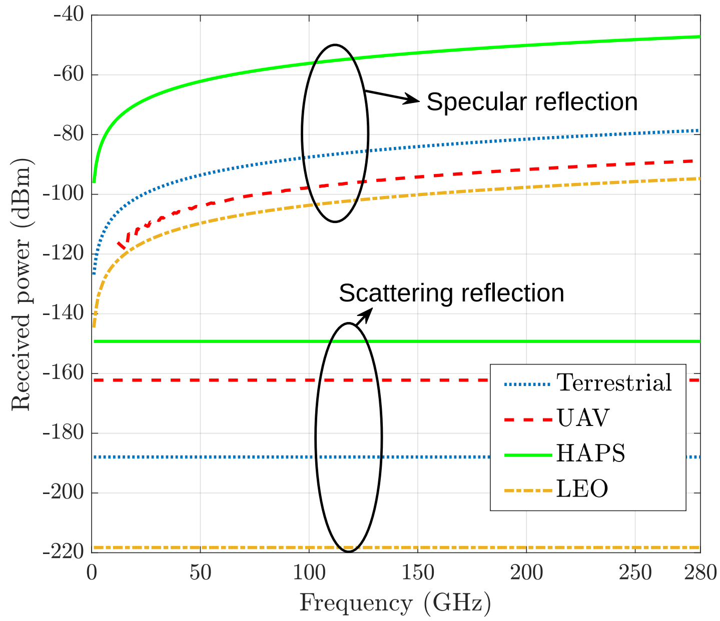

Figure 5.8: Received power vs. carrier frequency (different platforms).

form hosts the maximal number of reflectors $N_{\max}$, and that link budget analysis for the scattering reflection paradigm is realized for the log-distance channel model for comparison purposes. The results show that in both specular and scattering reflection paradigms, the HAPS system provides the best performance due to its large surface area that accommodates the highest number of RIS reflectors. On the other hand, the RIS-equipped UAV performs worse than the terrestrial RIS under the specular reflection paradigm because of its small surface area, which accommodates a very small number of reflectors. In particular, when $f \leq 12$ GHz, the UAV, with dimensions 0.25×0.25 m^2, cannot host a single reflector. Given the scattering reflection paradigm, all platforms demonstrate stable performance for any carrier frequency. Indeed, by combining (5.50) into (5.14) and (5.34) respectively, we obtain the maximal received power, expressed by

$$\begin{aligned} P_r^{\max} &= P_t G_t G_r \left(\frac{\lambda}{4\pi}\right)^4 \frac{A_t^2}{\left(c_1 c_2 \lambda^2\right)^2 \left(d_t d_r\right)^\alpha} \\ &= \frac{P_t G_t G_r}{\left(4\pi\right)^4} \left(\frac{A_t}{c_1 c_2}\right)^2 \frac{1}{\left(d_t d_r\right)^\alpha}, \end{aligned} \tag{5.51}$$

for the terrestrial environment. However, for the non-terrestrial one, (if $d \leq H_{RIS}$) $P_r^{\max}$

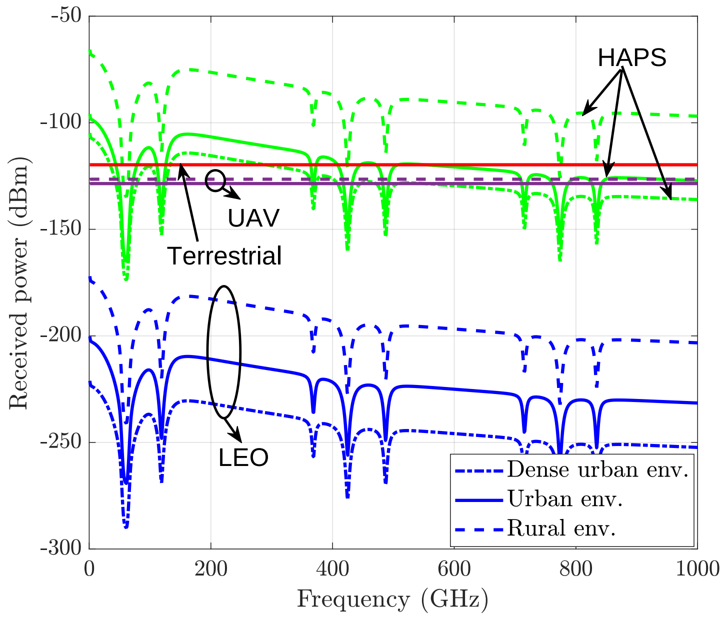

Figure 5.9: Received power vs. carrier frequency (different platforms and environment types).

is expressed as

$$\begin{aligned} P_r^{\max} &= P_t G_t G_r \left(\frac{\lambda}{4\pi}\right)^4 \frac{A_t^2}{(c_1 c_2 \lambda^2)^2 \left(H_{RIS}^2 + d^2\right)^2} \\ &= \frac{P_t G_t G_r}{(4\pi)^4} \left(\frac{A_t}{c_1 c_2}\right)^2 \frac{1}{\left(H_{RIS}^2 + d^2\right)^2}, \end{aligned} \tag{5.52}$$

otherwise (i.e., $d > H_{RIS}$),

$$P_r^{\max} = \frac{P_t G_t G_r}{(4\pi)^4} \left(\frac{A_t}{c_1 c_2}\right)^2 \frac{1}{\left(2H_{RIS} d\right)^2}. \tag{5.53}$$

According to (5.51)–(5.53), the received power is no longer dependent on the frequency (or the wavelength), but rather on A_t, c_1 and c_2.

Fig. 5.9 illustrates the received power as a function of the carrier frequency, given different RIS-equipped platforms and environment types. These results are obtained using the 3GPP channel models for the scattering reflection paradigm, i.e., (5.20), (5.39) and (5.49). Also, we assume the use of the maximal number of reflectors $N_{\max}$, dry air atmospheric attenuation, and an average tropospheric scintillation of 0.5 dB for the HAPS and LEO systems. We notice that both the terrestrial and UAV systems received powers are insensitive to frequency. Indeed, the frequency attenuation is successfully addressed through the deployment of a higher number of reflectors, since $N_{\max}$ increases with f. In contrast, HAPS and LEO systems performance are affected by frequency, and deeply by the atmospheric attenuation at specific frequency ranges. Nevertheless, some spectrum regions present a stable received power behaviour, such as below 40 GHz, and in 150-350 GHz and 500-700 GHz bands. The latter can be fully exploited for high capacity communications. Finally, depending on the operating frequency band and environment (dense urban, urban, or rural), one of the systems may be more suitable than the other ones, e.g., the RIS-equipped HAPS is the most interesting one in rural areas for most of the frequency bands.

5.4.3 Data Rate Evaluation and Impact of Platform Location

For the following simulations, we consider the same assumptions as in Fig. 5.7. Subsequently, (5.20), (5.39) and (5.49) can be used to evaluate the received power. The related data rate is calculated as

$$\mathcal{R} = B_w \log_2\left(1 + \frac{P_r}{P_N F}\right), \tag{5.54}$$

where B_w denotes the bandwidth, F stands for the noise figure, and P_N refers to the noise power, given by

$$P_N = KTB_wF, \tag{5.55}$$

where $k = 1.38 \times 10^{-23}$J.°K^{-1} is the Boltzmann constant and T is the temperature in °K. According to [7], when aerial networks operate in frequency bands $f \geq 6$ GHz, B_w can be up to 800 MHz in both uplink and downlink, while $F = 7$ dB.

Assuming that each platform is using $N_{\max}$ reflectors and that $B_w = 100$ MHz, we depict in Fig. 5.10 the resulting data rates as a function of the receiver gain G_r. Since typical user equipment or an IoT sensor have $G_r \leq 5$ dBi, both RIS-equipped terrestrial and HAPS systems can directly support the downlink communication to users, due mainly to their large RIS areas. However, RIS-equipped UAV and LEO satellite are unable to do the same due to the small RIS area in UAVs and the excessive propagation loss through LEO satellites. Alternatively, mounting RIS over UAVs and LEO satellites may be used to support inter-UAVs and inter-satellites communications [72]. Also, a swarm of RIS-equipped UAVs can be utilized to assist the communications cooperatively [69, 71].

The platform placement has an important impact on the data rate performance. Unlike LEO satellites that orbit around the Earth, the UAV and HAPS can be placed at a fixed

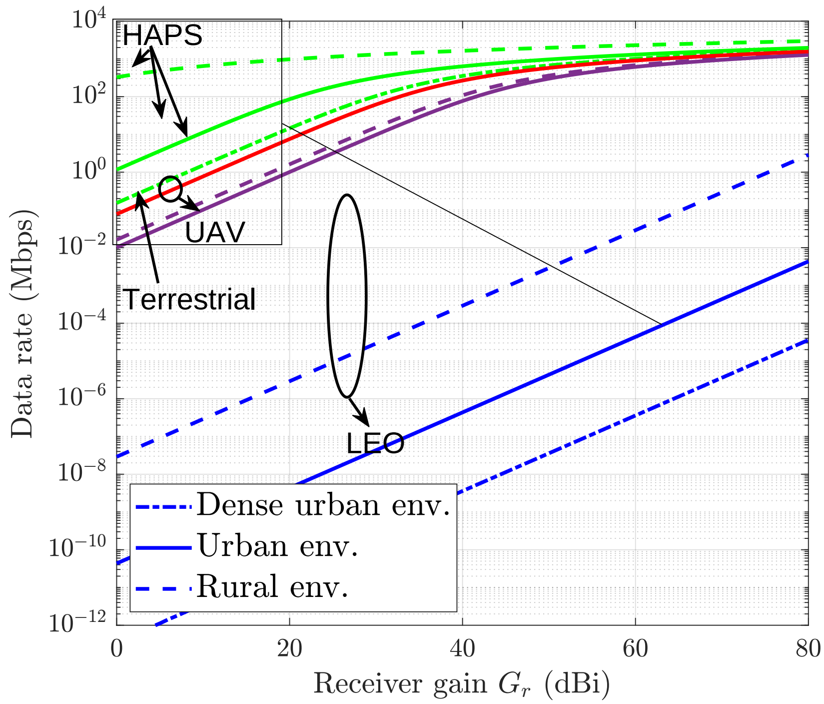

Figure 5.10: Data rate vs. receiver antenna gain.

position above the intended coverage area. However, due to wind and turbulence, these platforms may drift from the initial position, thus degrading the communication's performance. To assess such an effect, we present in Fig. 5.11 the data rate performance as a function of $\nu = 2 - \frac{r}{d}$, the normalized horizontal Rx-RIS distance. Moreover, we identify the optimal aerial platform location as calculated by (5.32) and the one provided by the simulations. Here, we assume that $G_r = 0$ dBi, while the remaining parameters are as for Fig. 5.10.

As discussed earlier, the optimal placement of the RIS-equipped aerial platform is dependent on the latter's altitude H_{RIS} and coverage radius d. For the RIS-equiped UAV, the obtained optimal UAV location r^* that achieves the highest data rate (red dot) agrees with that of (5.32) (blue circle), for any environment type. For the RIS-equipped HAPS, we distinguish between two cases, namely for $d = 50$ km and $d = 10$ km. In both cases, the optimal simulated HAPS locations and those of (5.32) agree in the rural environment, but the latter drift away as the environment becomes urbanized. This is mainly due to the additional shadowing and NLoS links effects in the 3GPP model of urban environments, which were ignored in the calculation of (5.32). Moreover, this location gap is larger for $d = 10$ km due to a higher shadowing impact. For the terrestrial networks, the best location is either being the closest to Tx or Rx, with a preference for Tx. Indeed, since the BS (at

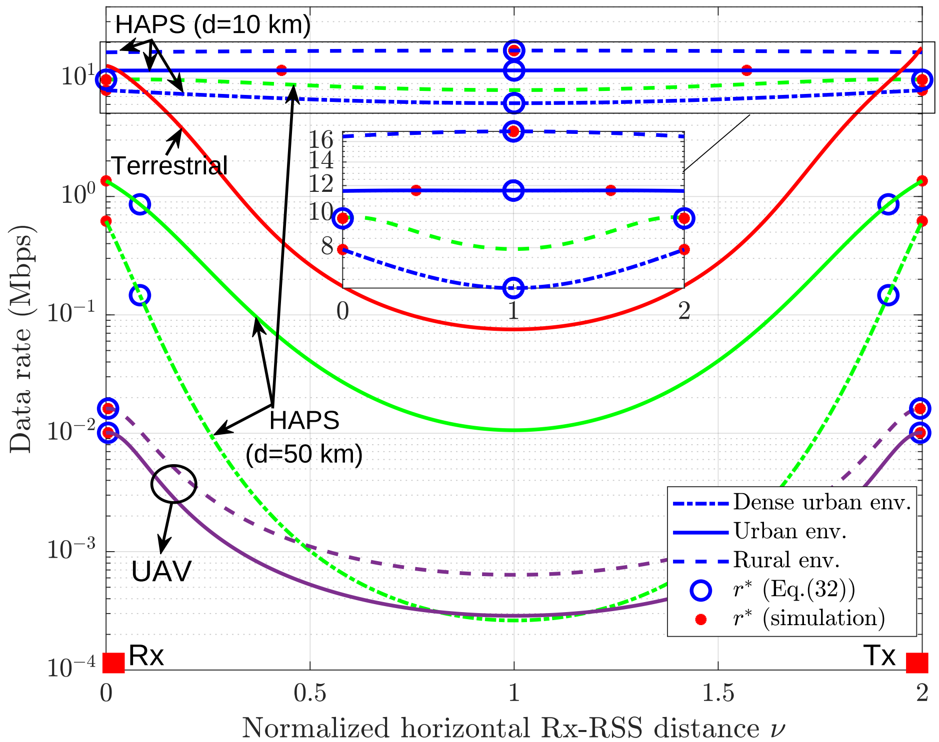

Figure 5.11: Data rate vs. normalized Rx-RIS distance ν (different platforms and environment types).

altitude 25 m) has a strong LoS link towards the RIS, the received signal is slightly better than being the closest to Rx (at altitude 1.5 m).

When an RIS-equipped HAPS operates in a rural environment, drifting from its initial location would have a small impact on the communication's performance. However, for a more urbanized environment, the data rate significantly degrades when the HAPS moves towards the middle of the Tx-Rx segment. The terrestrial RIS achieves the highest performance at optimal locations. However, due to its deployment inflexibility, it may not perform often at its best due to the varying Tx and Rx locations. In any case, when designed to assist cellular networks, deploying the RIS the closest to the BSs would eventually guarantee operating at near-optimal performance.

5.4.4 Outage Probability Analysis

The links between the presented aerial platforms and the terrestrial terminals are subjected to random variations due to shadowing and blockages. The instantaneous received power at a terrestrial terminal can be generally written as

$$P_r = \overline{P_r} + X, \tag{5.56}$$

where $\overline{P_r}$ is the average received power, defined as

$$\overline{P_r} = P_t + G_t + G_r - (\overline{PL_{Tx-RIS}} + \overline{PL_{RIS-Rx}}) + 20\log(N), \tag{5.57}$$

where $\overline{PL_{Tx-RIS}}$ and $\overline{PL_{RIS-Rx}}$ denote the average path-loss of links between the RIS-equipped aerial platform and the transmitter and the receiver, respectively. Also, X represents the resulting shadow fading of both links. It is modeled as a zero-mean normal distribution with a standard deviation $\sigma_s = \sqrt{\sigma^2_{Tx-RIS} + \sigma^2_{RIS-Rx}}$. The probability density function (pdf) of the received power can be written as

$$f(P_r) = \frac{1}{\sigma_s\sqrt{2\pi}} \exp\left(-\frac{(P_r - \overline{P_r})^2}{2\sigma_s^2}\right),\ P_r \geq 0. \tag{5.58}$$

Accordingly, the outage probability can be obtained from the cumulative distribution function (cdf) as

$$\mathcal{P}_{\text{out}} = \mathbb{P}(P_r \leq x) = \int_0^x f(P_r)\, dP_r = 1 - \frac{1}{2}\text{erfc}\left(\frac{x - \overline{P_r}}{\sigma_s\sqrt{2}}\right), \tag{5.59}$$

where x reflects the receiver sensitivity and $\text{erfc}(x) = \frac{2}{\sqrt{\pi}}\int_x^\infty \exp(-t^2)\, dt$ is the complementary error function.

Using the 3GPP models under scattering reflection paradigm (Table 5.3) with the characteristics of aerial platforms (Table 5.4) and same assumptions as in Fig. 5.7, we depict in Fig. 5.12 the cdf of the received power at user terminals with 0 dB gain, and assisted by RIS mounted on different aerial platforms in various environments. For any aerial platform, as the receiver's sensitivity degrades, i.e., x increases, the outage probability increases. This performance degradation is more significant in highly urbanized environments due to higher shadowing loss. Nevertheless, the outage performance gap between rural and urban is more noticeable for HAPS-RIS assisted communications than UAV-RIS assisted ones.

The outage probability performance depends on the coverage area of the aerial platform. To analyze the impact of the coverage area, we illustrate in Fig. 5.13 the outage performance as a function of the coverage radius. For these simulations, we assume a receiver power sensitivity $P_r^{\text{th}} = -115$ dBm. From Fig. 5.13, an outage probability lower than 10% requires a coverage radius below 0.5 km for a terrestrial RIS and below 1 km for a UAV-RIS, respectively, whereas a HAPS-RIS can support an area between 40 km and 80 km in radius ($\approx$ 80 times larger than for a terrestrial RIS). This demonstrates the high potential of deploying RIS on HAPS compared to the other alternatives.

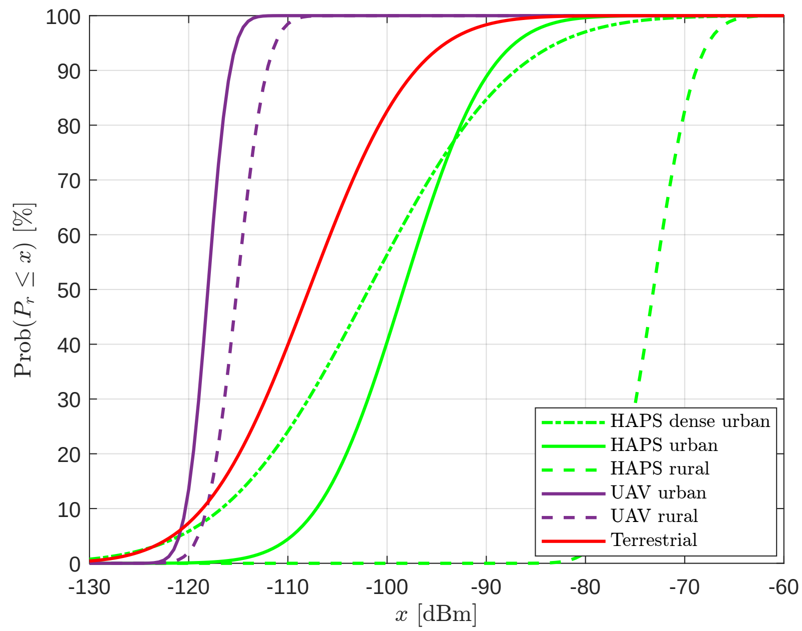

Figure 5.12: cdf of the received power at ground terminals assisted by RIS-equipped aerial platforms (different environment types).

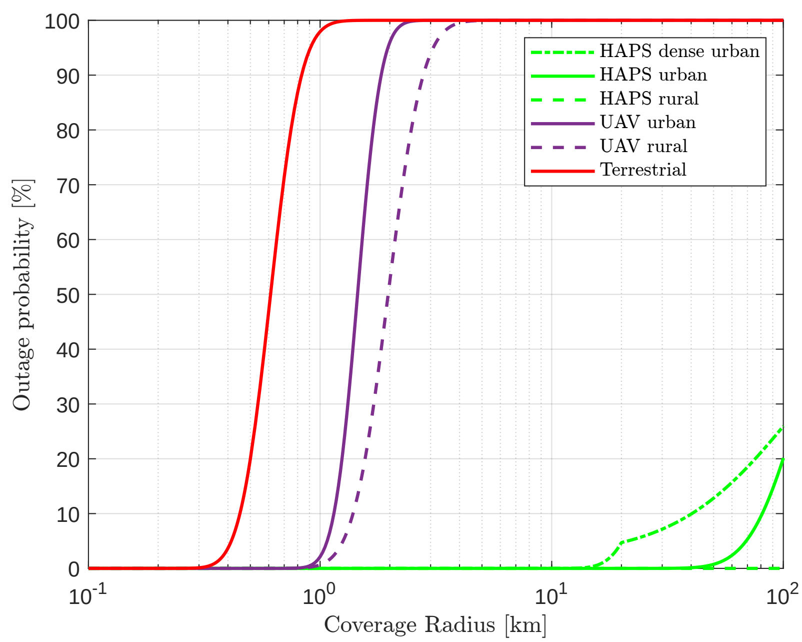

Figure 5.13: Outage probability vs. coverage radius for RIS-assisted communications (different environment types).

5.5 Conclusion

In this chapter, we conducted the link budget analysis for the envisioned RIS-equipped aerial platforms, namely UAVs, HAPS, and LEO satellites. Through literature overview, we identified two reflection paradigms, i.e., specular and scattering. For each reflection paradigm, we discussed its realization conditions, then we derived the associated optimal RIS-equipped platform location that maximizes the received power. Numerical results provided important insights on the design conditions of RIS-assisted communications:

- The scattering paradigm is gaining more interest in the research community than the specular one due to its practical accuracy.
- The RIS-equipped HAPS presents superior performance in different types of environments, compared to terrestrial and other aerial platforms supported communications.
- The received power performance is limited by the sizes of the RIS surface and reflector.
- When using the maximal number of reflectors in a surface, the link budget of the scattering reflection paradigm becomes independent from the carrier frequency.
- Supporting ground users with RIS-equipped UAVs and LEO satellites might not be feasible. Nevertheless, RIS can be used to assist inter-UAV or inter-LEO communications. Also, a swarm of RIS-equipped UAVs can support terrestrial users.
- The best RIS-equipped platform location significantly depends on the operating altitude, coverage footprint, and environment type.
- Finally, unlike other RIS assisted communications, HAPS-RIS assisted ones sustain the best outage probability/coverage performances in any type of environment.

Based on the aforementioned findings and the distinct features of HAPS-RIS, we will further explore and investigate in the next chapter the potentials of HAPS-RIS for complementing current terrestrial networks. To be noted, this study focused on the feasibility of the communication links while ignoring the impact of the channel estimation overhead, which also deserves further studies.

Chapter 6

Beyond-Cell Communications via HAPS-RIS

6.1 Introduction

One of the main goals of future wireless network is to provide ubiquitous connectivity (i.e., wireless connectivity to everyone and everything, everywhere, every time at an affordable rate) [100]. Ubiquitous connectivity can be achieved in urban areas through the dense deployment of base stations (BSs), including small cells. However, with increasing numbers of users and hampered by severe shadowing, blockages, and non-line-of-sight (NLoS) links, even ultra dense networks cannot support all users in an urban area. Further, deploying a large number of BSs inevitably leads to high capital expenditures (CAPEX) and operational expenditures (OPEX) [101].

Recent studies have proposed deploying reconfigurable intelligent surfaces (RIS) around BSs as an energy-efficient solution to overcome severe shadowing and blockage effects [102]. Also, RIS are seen as energy-efficient alternative to active antenna architecture such as re-

The main contents of this chapter have been produced in two papers: 1) A paper accepted in IEEE Global Communications Workshops (Globecom) 2022: **S. Alfattani**, A. Yadav, H. Yanikomeroglu, and A. Yongacoglu, "Beyond-Cell Communications via HAPS-RIS", *IEEE Global Communications Workshop (Globecom Workshop)* , 04–08 December 2022, Rio de Janeiro, Brazil.

2) A paper under review in in IEEE Wireless Communications Letters: 9. **S. Alfattani**, A. Yadav, H. Yanikomeroglu, and A. Yongacoglu, "Resource-efficient HAPS-RIS enabled beyond-cell communications", under review in *IEEE Wireless Communications Letters* (submission: 20 Jul 2022, 1st results: 16 Sep 2022, 2nd submission: 27 Oct 2022).

lays [69, 12]. However, the deployment of RIS in terrestrial networks involves several challenges, including inflexible deployment and weak wireless channel conditions due to shadowing, blockages and NLoS links. In addition, dynamic and unpredictable network traffic generates unprecedented data rate demands, which can overload some BSs. Accordingly, even an optimized deployment of BSs and RIS in urban areas might be unable to cope with the dynamic demands.

To overcome these issues, we proposed in chapter 4 integrating RIS with non-terrestrial networks (NTN). Due to the limited energy on aerial platforms, integrating RIS with NTN is more appealing than integrating them in terrestrial networks. In that chapter, we also discussed several benefits of RIS-aided NTN, including energy and cost savings, favorable wireless channel conditions, strong LoS links, a wider coverage area, and flexible placement. In chapter 5, we provided a detailed link budget analysis of different RIS-aided aerial platforms, such as unmanned aerial vehicles (UAVs), high altitude platform station (HAPS) nodes, and low Earth orbit (LEO) satellites, and we compared that to RIS-aided terrestrial networks.

As we also showed in chapter 5 and [103], the typical large size of a HAPS allows the accommodation of a large number of reflecting units. Thus, it can outperform other aerial RIS-aided systems, such as UAV-RIS. Therefore, motivated by the aforementioned findings, we propose in this chapter a novel *beyond-cell* communications approach involving an HAPS equipped with RIS (HAPS-RIS). This approach works in tandem with legacy terrestrial networks by offering service to unsupported users whose quality-of-service (QoS) requirements cannot be fulfilled by legacy networks. In our proposed scheme, unsupported users are connected to a dedicated control station (CS) via a HAPS-RIS. The main contributions in this chapter include, but are not limited to, the following:

- We formulate four novel optimization problems, including throughput maximization, worst user rate maximization, and reflecting units usage minimization to design optimal power and RIS unit assignment strategies for the users supported through *beyond-cell* communications. Also, A novel resource-efficient optimization problem that maximizes the percentage of connected UEs while minimizing the usage of RIS units and transmit power is presented.
- We present thorough numerical simulation results, which indicate that *beyond-cell* communications complement legacy terrestrial networks well and enhance the total

number of users served. The percentage of users that satisfy the QoS requirements increases while the required number of terrestrial BSs decreases.

- We also provide important insights about the different allocation schemes. For instance, by conceding a small degradation (1%) in the system sum rate, the worst user rate maximization-based allocation scheme maximizes the fairness among the users and increases the rate of the worst user (∼15%). Moreover, by increasing the CS power by 1 dB, the size of the HAPS or the required number of reflectors is decreased by ∼11%.

- For the resource-efficiency problem, since the resulting problem is a mixed-integer nonlinear program (MINLP) and hard to solve, a low complexity two-stage algorithm is proposed to solve it.

- Finally, through numerical results, we study the impact of HAPS size and QoS requirements of UEs on the percentage of connected UEs and demonstrate significant improvements in RE of the system.

The remainder of the chapter is organized as follows. Section 6.2 presents the system model for all user equipment (UE), whether connected to a BS or supported by a HAPS-RIS. Section 6.3 details the problem formulations for different system objectives. The proposed solutions are discussed in Section 6.5, while the numerical results are presented and discussed in Section 6.7. Finally, Section 6.8 concludes the chapter.

6.2 System Model

We consider a downlink transmission scenario in an integrated terrestrial and non-terrestrial wireless network consisting of a single HAPS with a coverage area that includes L base stations (BSs) and K single-antenna UEs (e.g., smart phones, sensing nodes or IoT devices, etc.). The HAPS is located in the center of the coverage area at an altitude of 20 km[1], and it is equipped with the RIS with a total of $N_{\max}$ reflecting units. Since the antennas of BSs are down-tilted to serve terrestrial UEs, we consider the HAPS coverage area also includes a dedicated high-directional antenna gain transceiver, known as the ground CS. The CS is connected to the core network with the primary aim of supporting unserved UEs via the

[1] Generally, HAPS systems are quasi-stationary [102], and hence, their mobility is ignored in this model.

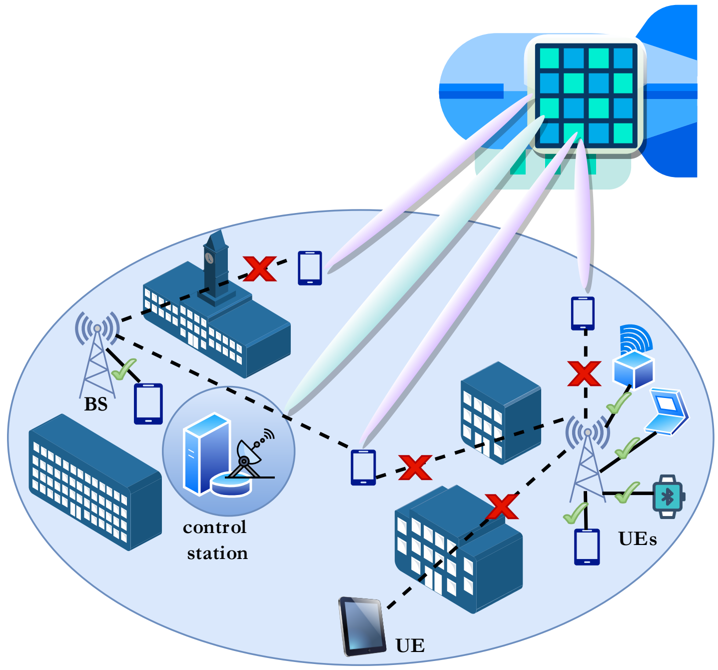

Figure 6.1: System model for HAPS-RIS beyond-cell communications.

HAPS-RIS. Further, the CS also manages the association between the BSs and the UEs and configures the RIS.

The environment for this scenario is an urban one where K UEs are uniformly distributed in the HAPS coverage area. In contrast, the BSs are optimally placed to maximize the number of connected UEs. We adopt Lloyd's algorithm for optimizing the placement of BSs. The algorithm aims to minimize the Euclidean distances between the UEs and the BSs; this distance is the factor that most affects the quality of the channel links[2]. In an urban environment, wireless signals suffer severe blockages and shadowing [85]. Accordingly, some UEs might not be associated with any BSs due to poor channel quality. Moreover, some UEs might not have service when BSs are fully loaded. Thus, the UEs in the system can be divided into two groups. The first group includes the UEs that can be served by BSs; the second group consists of the remaining UEs that can be served by the CS via HAPS-RIS.

[2]This algorithm is also known as a k-means clustering algorithm [104].

6.2.1 Within-Cell Connection: UEs to Terrestrial BSs

In this work, we employ the orthogonal frequency division multiplexing (OFDM) transmission scheme, where the entire terrestrial system bandwidth B_{BS} Hz is divided into equal subcarriers each of bandwidth B_{UE} Hz. Without loss of generality, the UEs in each cell are allowed to use only one subcarrier to transmit their data. However, the UEs from other cells can use the same subcarrier. Thus, there will be inter-cell interference but no intra-cell interference.

Accordingly, the received signal at UE k from BS l on a given subcarrier can be written as

$$y_{kl} = \sqrt{P_{kl}^{\mathrm{BS}}} h_{kl} x_{kl} + \sum_{l'=1, l' \neq l}^{L} \sqrt{P_{kl'}^{\mathrm{BS}}} h_{kl'} x_{kl'} + w_{kl}, \tag{6.1}$$

where P_{kl}^{BS} and x_{kl} denote the transmitted power and the transmitted symbol, respectively. w_{kl} denotes the additive white Gaussian noise (AWGN) with zero mean and power spectral density N_0. h_{kl} denotes the channel coefficient between UE k and BS l on a given subcarrier, and it can be expressed as

$$h_{kl} = \sqrt{G_l^{\mathrm{BS}} G_k^{\mathrm{UE}} (\mathsf{PL}_{kl}^{\mathrm{BS}})^{-1}}, \tag{6.2}$$

where G_l^{BS} and G_k^{UE} denote the antenna gain of BS l and UE k, respectively. $\mathsf{PL}_{kl}^{\mathrm{BS}}$ denotes the path loss of the channel between BS l and UE k. Now, the achievable signal-to-interference-plus-noise ratio (SINR) at UE k served by BS l can be written as

$$\gamma_{kl} = \frac{P_{kl}^{\mathrm{BS}} |h_{kl}|^2}{\sum_{l'=1, l' \neq l}^{L} P_{kl'}^{\mathrm{BS}} |h_{kl'}|^2 + N_0 B_{\mathrm{UE}}}. \tag{6.3}$$

The corresponding achievable rate in bits per seconds (bps) between BS l and UE k can be written as

$$R_{kl} = B_{\mathrm{UE}} \log_2(1 + \gamma_{kl}). \tag{6.4}$$

For a UE to be directly associated with a BS l, the data rate between them should be above the minimum required data rate, i.e., $R_{kl} \geq R_{\mathrm{min}}$. Let $\mathcal{S}_k \subset \{R_{k1}, ..., R_{kL}\}$ denote the set of data rates between UE k and L BSs that have a data rate higher than the minimum required rate R_{min}. The UE k is associated with the BS l with the highest data rate in the set $\mathcal{S}_k$, i.e., ($l = \max_{\boldsymbol{l}} \mathcal{S}_k$). Also, let $\mathcal{M}_l \subset \{1, ..., k\}$ denote the set of UEs with the best channel toward BS l, and the cardinality of the set is denoted as $|\mathcal{M}_l|$.

For the UE $j, j \neq k$ with $\mathcal{S}_j = \{\phi\}$ (i.e., $R_{jl} < R_{\mathrm{min}}, \forall\, l \in \{1, ..., L\}$), its communication is supported by the CS through HAPS-RIS. Also, when $|\mathcal{M}_l| > (B_{\mathrm{BS}}/B_{\mathrm{UE}})$, we declare the BS l as fully loaded or its capacity as fully utilized. Hence, we drop UEs with the lowest channel gain to be served by the CS via HAPS-RIS until $|\mathcal{M}_l| \leq (B_{\text{BS}}/B_{\text{UE}})$. Accordingly, we denote the set of K_1 UEs supported by direct links from the BSs (*within-cell* communications) with $\mathcal{K}_1 = \{1, \ldots, K_1\}$. Similarly, we denote the set of K_2 UEs supported by the CS through HAPS-RIS (*beyond-cell* communications) with $\mathcal{K}_2 = \{1, \ldots, K_2\}$.

6.2.2 Beyond-Cell Connection: UEs to CS via HAPS-RIS

The unsupported UEs that cannot form a direct connection with the terrestrial BS will be served by the CS via HAPS-RIS. We assume that the CS serves the UEs in set $\mathcal{K}_2$ using the OFDM protocol, and hence, there will be no inter-UE interference. Further, both *within-cell* and *beyond-cell* communications occur in two orthogonal frequency bands, while keeping B_{UE} same for both types of connection. Consequently, there will be no interference between *within-cell* UEs belonging to set $\mathcal{K}_1$ and *beyond-cell* UEs belonging to set $\mathcal{K}_2$.

Accordingly, the received signal at UE $k \in \mathcal{K}_2$ on a given subcarrier can be expressed as

$$y_k = \sqrt{P_k^{\text{CS}}} h_k \Phi_k \, x_k + w_k, \tag{6.5}$$

where x_k and P_k^{CS} denote the transmitted signal and power of UE k, respectively. w_k denotes the zero-mean AWGN. h_k denotes the *effective* channel gain from the CS to the HAPS-RIS and from the HAPS-RIS to UE k, and it is given by [103][3]

$$h_k = \sqrt{G_{\text{t}}^{\text{CS}} G_{\text{r}}^{k} (\mathsf{PL}^{\text{CS}-\text{HAPS}-k})^{-1}}, \tag{6.6}$$

where G_{t}^{CS} denotes the transmit antenna gain of the control station, and G_{r}^{k} is the receiver antenna gain of UE k. $\mathsf{PL}^{\text{CS}-\text{HAPS}-k}$ represents the cascaded path loss between the control station and the HAPS (i.e., $\mathsf{PL}^{\text{CS}-\text{HAPS}}$), and between the HAPS and UE k (i.e., $\mathsf{PL}^{\text{HAPS-}k}$). Since the amplitude and phase responses of RIS reflecting units are frequency-dependent [80] and each UE uses different subcarrier, then each UE is assigned with a distinct and dedicated set of RIS units tuned to its respective subcarrier. Thus, Φ_{k} represents the reflection gain of the RIS corresponding to UE k, and is expressed as

$$\Phi_k = \sum_{i=1}^{N_k} \rho_i e^{-j\left(\phi_{i,k} - \theta_i - \theta_{i,k}\right)}, \tag{6.7}$$

[3]Here, we consider negligible difference in channels between UE k and RIS reflecting units, since they are dominated by LoS links.

where ρ_i denotes the reflection loss corresponding to RIS unit i. θ_i and $\theta_{i,k}$ represent the corresponding phases between RIS unit i and both the control station and UE k, respectively. $\phi_{i,k}$ represents the adjusted phase shift of RIS unit i corresponding to user k, while N_k represents the total number of reflecting units allocated to UE k. The RIS reflecting units are divided among the UEs because each UE uses different subcarrier.

Accordingly, the signal-to-noise ratio (SNR) at UE k can be written as

$$\gamma_k = \frac{P_k^{\mathrm{CS}} \left|h_k \Phi_k\right|^2}{N_0 B_{\mathrm{UE}}}, \tag{6.8}$$

and the achievable rate of UE $k \in \mathcal{K}_2$ can be expressed as

$$R_k = B_{\mathrm{UE}} \log_2(1 + \gamma_k). \tag{6.9}$$

6.3 Problem Formulation

In this section, we discuss three resources (available power at the CS and reflecting units at the HAPS) allocation schemes for the UEs assisted by the *beyond-cell* communication, and accordingly, formulate three optimization problems.

6.3.1 Sum Rate (Throughput) Maximization

The goal of this problem is to support all the K_2 UEs and maximize their sum rate by optimally allocating the reflecting units and transmitting power to all the UEs. Thus, the formulation becomes

$$
\begin{aligned}
\max_{\Phi_k, N_k, P_k^{\mathrm{CS}}} \quad & \sum_{k=1}^{K_2} R_k && \text{(6.10a)}\\
\text{s.t.} \quad & L \leq L_{\max}, && \text{(6.10b)}\\
& R_k \geq R_{\mathrm{th}}, \ \ \forall k = 1, 2, \ldots, K_2, && \text{(6.10c)}\\
& \sum_{k=1}^{K_2} N_k \leq N_{\max}, && \text{(6.10d)}\\
& \phi_{i,k} \in \{0, \Delta\phi, 2\Delta\phi, \ldots, (2^b - 1)\Delta\phi\}, \ \ \forall i = 1, 2, \ldots, N_k, \ \forall k = 1, 2, \ldots, K_2, && \text{(6.10e)}\\
& \sum_{k=1}^{K_2} P_k^{\mathrm{CS}} \leq P_{\max}^{\mathrm{CS}}, && \text{(6.10f)}\\
& N_k \in \{N_{k,\min}, N_{k,\min} + 1, \ldots, N_{k,\max}\}, \ \ \forall k = 1, 2, \ldots, K_2, && \text{(6.10g)}\\
& P_{k,\min}^{\mathrm{CS}} \leq P_k^{\mathrm{CS}} \leq P_{k,\max}^{\mathrm{CS}}, \ \ \forall k = 1, 2, \ldots, K_2, && \text{(6.10h)}
\end{aligned}
$$

where (6.10b) limits the number of terrestrial BSs in the area; and thus, limits the expenditure incurred by network operators. Note that, the value of K_2 is dependent on the value of L. Higher the value of L, lower is the value of K_2. Constraint (6.10c) ensures that the minimum required rate is achieved by each UE. Constraint (6.10d) guarantees that the total number of allocated reflecting units to all UEs is less than the maximum number available at the HAPS. In practice, the value of $N_{\max}$ is dependent on the HAPS size. Constraint (6.10e) determines the discrete range of the adjustable phase shifts values for each RIS unit, where $\Delta\phi_{i,k} = 2\pi/2^b$ with b as the number of bits used to uniformly quantize the phase shifts of each RIS element. Constraint (6.10f) ensures the total allocated power for each UE does not exceed the maximum power, $P_{\max}^{\text{CS}}$, of the control station. Constraints (6.10g)-(6.10h) ensure feasible and fair allocation of both reflecting units and CS power, respectively, where $N_{k,\min}, N_{k,\max}$, $P_{k,\min}^{\text{CS}}$, and $P_{k,\min}^{\text{CS}}$ denote the minimum and maximum allocated RIS units and power per UE.

6.3.2 Minimum Rate Maximization (Max-Min Rate)

Sum rate (throughput) maximization based allocation scheme might be biased toward UEs with better channel links. Therefore, for fair resource allocation, we consider in this subsection the problem of maximizing the minimum rate among all UEs. Accordingly, the max-min fairness problem can be formulated as

$$\underset{\Phi_k, N_k, P_k^{\text{CS}}}{\text{maximize}} \quad \min_{k=1,\dots,K_2} \; R_k \tag{6.11a}$$

$$\text{s.t.} \quad (6.10\text{b}) - (6.10\text{h}). \tag{6.11b}$$

6.3.3 Reflecting Units Minimization

Despite being passive in nature, the RIS reflecting units consume energy for control and configuration [69, 12]. The energy consumption might be significant for HAPS equipped with a large number of reflectors. For a cost-effective deployment of HAPS in terms of onboard energy consumption and size of HAPS, it is essential to minimize the total number of RIS reflecting units. Accordingly, the RIS reflecting units minimization problem can be formulated as

$$\min_{\Phi_k, N_k, P_k^{\text{CS}}} \sum_{k=1}^{K_2} N_k \tag{6.12a}$$

$$\text{s.t.} \quad (6.10\text{b}) - (6.10\text{h}). \tag{6.12b}$$

6.4 Resource-efficient Maximization

Using power efficiently at the HAPS-RIS for activating the RIS units, and at the CS for transmitting signals offer sustainable environment and longer refueling intervals for HAPS. Also, in case of a large UE density or strict QoS requirement, it might infeasible to serve all unserved UEs by the CS via HAPS-RIS. Therefore, we need to select as many UEs that can be supported by the CS, while using as minimum system resources (transmit power and RIS units) as possible. Accordingly, we define a novel performance metric known as resource efficiency as follows:

Definition 1. *Resource efficiency (RE) of the beyond-cell communication system, η, is defined as the ratio between the percentage of served UEs and the average power consumption in dBm by each supported UE, which includes the consumption towards signal transmission and RIS units configuration:*

$$\eta = \frac{\frac{1}{K}\left(K_1 + \sum_{k=1}^{K_2} u_k\right)}{\frac{1}{|\mathcal{U}|}\sum_{k=1}^{K_2}\left(P_k^{\text{CS}} u_k + P_{\text{RIS}} N_k u_k\right)}, \tag{6.13}$$

where u_k is the indicator variable, if $u_k = 1$, user k will get service by HAPS-RIS, otherwise not if $u_k = 0$. In the denominator, the terms $\sum_{k=1}^{K_2} P_k^{\text{CS}} u_k$ and $\sum_{k=1}^{K_2} P_{\text{RIS}} N_k u_k$ represent the total transmit power consumption at the CS and the total power consumed by the RIS units for all supported UEs, respectively. P_{RIS} denotes the consumed power by each RIS unit for phase shifting, which is dependent on the RIS configuration technology and its resolution. Finally, $|\mathcal{U}|$ denotes the cardinality of the set, which constitutes the UEs supported by the CS via HAPS-RIS.

In the following, we formulate the resource-efficient UEs maximization problem. It can be expressed as

$$\max_{u_k,\Phi_k,N_k,P_k^{\text{CS}}} \eta \tag{6.14a}$$

$$\text{s.t. } L \leq L_{\max}, \tag{6.14b}$$

$$R_k \geq u_k R_{\text{th}}, \ \ \forall k = 1, 2, \ldots, K_2, \tag{6.14c}$$

$$\sum_{k=1}^{K_2} u_k N_k \leq N_{\max}, \tag{6.14d}$$

$$\phi_{i,k} \in \{0, \Delta\phi, 2\Delta\phi, \ldots, (2^b - 1)\Delta\phi\}, \ \ \forall i = 1, 2, \ldots, N_k, \ \forall k = 1, 2, \ldots, K_2, \tag{6.14e}$$

$$\sum_{k=1}^{K_2} u_k P_k^{\text{CS}} \leq P_{\max}^{\text{CS}}, \tag{6.14f}$$

$$N_k \in \{N_{k,\min}, N_{k,\min} + 1, \ldots, N_{k,\max}\}, \quad \forall k = 1, 2, \ldots, K_2, \tag{6.14g}$$

$$P_{k,\min}^{\text{CS}} \leq P_k^{\text{CS}} \leq u_k P_{k,\max}^{\text{CS}}, \ \ \forall k = 1, 2, \ldots, K_2, \tag{6.14h}$$

$$u_k \in \{0, 1\}, \tag{6.14i}$$

where all the terms are as defined previously in (6.10).

6.5 Proposed Solution

In this section, we discuss the solution approaches for the aforementioned optimization problems.

6.5.1 Sum Rate Maximization

In problem (6.10), constraint (6.10b) is determined by an expenditure analysis of the network deployment, and typically it is selected as $L = L_{\max}$ to maximize the percentage of UEs with direct connections to BSs. It should be noted that the variables N_k and $\phi_{i,k}$ are discrete variables; and thus (6.10) becomes computationally challenging to solve as it requires employing heuristic discrete optimization algorithms. However, for a large RIS area, N_k can be approximated as a continuous variable. This approximation is substantiated by the fact that each UE is allocated a subarea of the RIS, and the total area allocated to all UEs is approximately equivalent to the total RIS area. Similarly, $\phi_{i,k}$ in (6.10e) practically has a range of discrete phase shifts. However, several works have shown that close to optimal continuous performance can be achieved even with low resolution discrete phase shifts

[105]. Therefore, $\phi_{i,k}$ can be approximated as a continuous variable. Moreover, for large values of γ_k the rate of UE k, given in (6.9), can be approximated as $R_k \approx B_{\mathrm{UE}} \log_2(\gamma_k)$. Accordingly, the sum rate of the set $\mathcal{K}_2$ UEs is given as

$$\sum_{k=1}^{K_2} R_k \approx B_{\mathrm{UE}} \log_2 \left(\prod_{k=1}^{K_2} \gamma_k \right). \tag{6.15}$$

Moreover, the rate constraint (6.10c) of each UE can be written in terms of its SNR. Accordingly, problem (6.10) can be reformulated as

$$\min_{\Phi_k, N_k, P_k^{\mathrm{CS}}} \quad \frac{1}{\prod_{k=1}^{K_2} \gamma_k} \tag{6.16a}$$

$$\text{s.t.} \quad \frac{1}{\gamma_k} \leq \frac{1}{\gamma_{\min}}, \quad \forall k = 1, 2, \ldots, K_2, \tag{6.16b}$$

$$(6.10c) - (6.10h). \tag{6.16c}$$

Now, the objective as well as the constraints of problem (6.16) are posynomials.[4] Therefore, optimal solutions can be found in polynomial-time using geometric programming (GP) approach [106].

6.5.2 Minimum Rate Maximization (Max-Min Rate)

By introducing a new slack variable t, (6.11) can be reformulated as

$$\min_{\Phi_k, N_k, P_k^{\mathrm{CS}}} \quad t \tag{6.17a}$$

$$\text{s.t.} \quad \frac{1}{\gamma_k} \leq \frac{1}{t}, \quad \forall k = 1, 2, \ldots, K_2, \tag{6.17b}$$

$$(6.16b), (6.10c) - (6.10h). \tag{6.17c}$$

The objective function (6.17) is a monomial function, whereas the constraints (6.17b – 6.17c) are posynomial constraints. Therefore, it is an GP problem that can be solved optimally [106].

[4] The term 'posynomial' refers to a function consists of a sum of positive polynomials [106].

6.5.3 Reflecting Units Minimization

Following the same procedure applied in the previous subsection, and by relaxing N_k to be a continuous variable, the problem (6.12) can be re-written as

$$\min_{\Phi_k, N_k, P_k^{\mathrm{CS}}} \sum_{k=1}^{K_2} N_k \tag{6.18a}$$
$$\text{s.t.} \quad (6.16b), (6.10c) - (6.10h). \tag{6.18b}$$

It is easy to notice that (6.18) is also an GP problem and can be solved optimally [106], and the final value of N_k is approximated as $\lceil N_k^* \rceil$.

6.6 Resource-efficient Maximization

Since problem (6.14) is an MINLP, it is hard to solve jointly with the involved variables in an optimal manner with lower complexity. Therefore, we decoupled the problem into two subproblems and develop a low-complexity algorithm to solve it suboptimally. The main step of the proposed algorithm involves solving (6.14) in two stages.

In the first subproblem, we maximize the numerator of (6.14a) by maximizing the number of UEs, which can establish direct connection with TNs (i.e., by setting $L = L_{\max}$[5]), and then finding the set of maximum feasible UEs $\in \mathcal{K}_2$, which can be supported by the CS via HAPS-RIS. To this end, we first sort the channel gains of all UEs. Secondly, under the assumptions of equal power allocation to each UE and perfect reflection of each RIS unit, we allocate the minimum required number of RIS units to each UE as follows:

$$N_k = \left\lceil \sqrt{\frac{N_0 B_{\mathrm{UE}} (2^{\frac{R_{\min}}{B_{\mathrm{UE}}}} - 1)}{P_k^{\mathrm{CS}} \left| h_k \right|^2}} \right\rceil. \tag{6.19}$$

The initial RIS units allocation starts with UEs with the best channel conditions until all RIS units are utilized. As a result, a set $\mathcal{U}$ with the largest number of feasible UEs is determined.

In the second subproblem, the denominator of (6.14a) is minimized by optimally allocating the CS power and RIS units to each UE belongs to set $\mathcal{U}$. This is accomplished by

[5] This value is dependent on the communication frequency, and the statistics of the users density and their rate demands. It is also determined by operator's expenditure analysis.

solving the following optimization problem:

$$\min_{\Phi_k, N_k, P_k^{\text{CS}}} \sum_{k=1}^{|\mathcal{U}|} P_k^{\text{CS}} + P_{\text{RIS}} N_k \tag{6.20a}$$

$$\text{s.t. } R_k \geq R_{\text{th}}, \ \forall k = 1, 2, \ldots, |\mathcal{U}|, \tag{6.20b}$$

$$\sum_{k=1}^{K_2} N_k \leq N_{\max}, \tag{6.20c}$$

$$\phi_{i,k} \in \{0, \Delta\phi, 2\Delta\phi, \ldots, (2^b - 1)\Delta\phi\}, \ \forall i = 1, 2, \ldots, N_k, \ \forall k = 1, 2, \ldots, K_2, \tag{6.20d}$$

$$\sum_{k=1}^{K_2} P_k^{\text{CS}} \leq P_{\max}^{\text{CS}}, \tag{6.20e}$$

$$\{N_{k,\min}, N_{k,\min} + 1, \ldots, N_{k,\max}\} \tag{6.20f}$$

$$P_{k,\min}^{\text{CS}} \leq P_k^{\text{CS}} \leq P_{k,\max}^{\text{CS}}, \ \forall k = 1, 2, \ldots, |\mathcal{U}|. \tag{6.20g}$$

Without loss of generality, problem (6.20) can be re-written as

$$\min_{\Phi_k, N_k, P_k^{\text{CS}}} \sum_{k=1}^{|\mathcal{U}|} P_k^{\text{CS}} + P_{\text{RIS}} N_k \tag{6.21a}$$

$$\text{s.t. } \frac{1}{\gamma_k} \leq \frac{1}{\gamma_{\min}}, \ \forall k = 1, 2, \ldots, |\mathcal{U}|, \tag{6.21b}$$

$$(6.20c) - (6.20g). \tag{6.21c}$$

Due to the involvement of integer and discrete variables N_k and $\phi_{i,k}$, respectively, problem (6.21) is a challenging problem and is difficult to solve optimally in polynomial time. To solve it efficiently, we relax N_k and $\phi_{i,k}$ to be continuous variables. After this relaxation, the objective and the constraints of (6.21) become posynomials, which can be solved optimally using geometric programming (GP) technique [106]. At the solution of the relaxed problem, the final solution to (6.21) is obtained by approximation as $N_k \approx \lceil N_k^* \rceil$. The pseudo-code of the proposed two-stage algorithm is described in Algorithm 4. Note that in practice $\phi_{i,k}$ should be selected from a set of discrete phase shifts. The cardinality of the set is based on the resolution of the phase shift. The selection optimization of the discrete phase shifts is still an open problem. We investigated this problem in [105] and showed that with our proposed algorithm, the performance gap between continuous phase shifts and a set of two discrete phase shifts is about 30%. The impact of relaxing $\phi_{i,k}$ and the performance gap can be significantly reduced with a set of large number of phase shifts.

6.6.0.1 Complexity Analysis

The iteration-complexity of Algorithm 4 is the same as of the standard barrier-based interior-point method with accuracy error ϵ, and is in the order of $\mathcal{O}(2.5\sqrt{|\mathcal{U}|+1}\ln\frac{6(|\mathcal{U}|+1)\Delta}{\epsilon})$, where the term Δ is associated to a perturbation in the feasible set [107]. However, the complexity of solving the original formulated problem optimally without relaxations and without decoupling them into two subproblems is computationally prohibited as it requires searching all possible combinations of RIS unit allocation and phase shifts configurations, and can be given as $\mathcal{O}\big((2^b)^{N_{\max}}\sum_{k=1}^{K_2}\prod_{i=1}^{N_{k,\max}}\binom{N_{\max}}{i}\big)$.

Algorithm 4 Efficient maximization of connected UEs

1: Set $L = L_{\max}$ and obtained set $\mathcal{K}_2$.
2: **Input:** $h_k, k \in \{1, 2, \dots, K_2\}$.
3: Sort K_2 UEs in descending order based on their channel gains $K_{S2} \leftarrow K_2$
4: **for** $k = 1 \dots K_{S2}$ **do**
5: **while** $\sum_{k=1}^{K_{S2}} N_k \leq N_{\max}$ **do**
6: $P_k^{\text{CS}} = P_{\max}^{\text{CS}}/K_{S2}$
7: Obtain initial N_k from (6.19).
8: **end while**
9: **end for**
10: **Stage-1 Output:** Selected UEs $\mathcal{U}$.
11: Solve optimally (6.21) for the set $\mathcal{U}$.
12: **Stage-2 Output:** $P_k^{\text{CS}*}$ and N_k^* $(\forall k = 1, \dots, |\mathcal{U}|)$.

6.7 Numerical Results and Discussion

In this section, we discuss the performance of the proposed *beyond-cell* communication approach by comparing different power and RIS-unit allocation strategies obtained by solving the aforementioned problems (i.e., (6.10), (6.11), (6.12), and (6.14)) and a benchmark *proportional* scheme. The benchmark scheme allocates the reflectors to each UE proportionally based on its channel gain, i.e., the UE with the worst channel gain will get the largest portion of the reflecting units.

In the simulation setup, we consider an urban environment with an area of 10 km by 10 km consisting of $L_{\max} = 4$ terrestrial BSs serving $K = 100$ randomly and uniformly

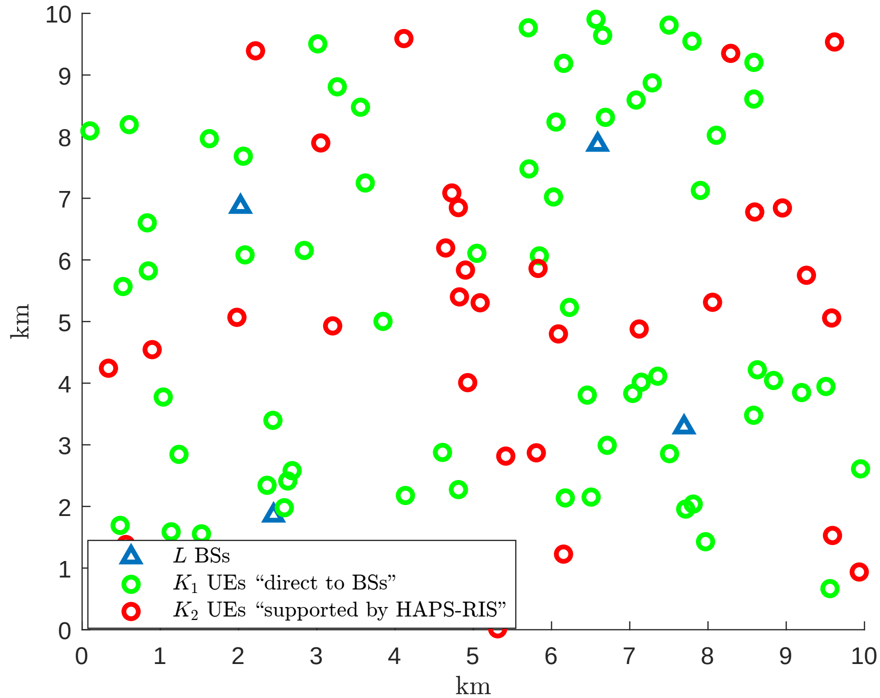

Figure 6.2: Locations of the UEs $\in \{\mathcal{K}_1, \mathcal{K}_2\}$ and BSs ($f_c = 2$ GHz, $\sigma_{\mathrm{BS-UE}} = 8$ dB).

distributed UEs with a minimum separation distance of 100 m between the UEs. The BSs are typically placed where the UE density is expected to be higher. Therefore, the BS locations are optimized using Lloyd's algorithm, which minimizes the distances between all the UEs and their associated BSs [104]. Further, we adopt the 3GPP standards [85] for terrestrial BS parameters with a BS height of $H_{\mathrm{BS}} = 25$ m and a power and antenna gain of $P^{\mathrm{BS}} = 35$ dBm and $G^{\mathrm{BS}} = 8$ dB. Also, we consider the communication at carrier frequency $f_c = 2$ GHz with shadowing standard deviation $\sigma_{\mathrm{BS-UE}} = 8$ dB, and all the UEs have the same height of 1.5 m. Then, by following the urban channel model for the path loss and the LoS probabilities detailed in [85, Tables 7.4.1-1 – 7.4.2-1], the channel gains between all UEs and all BSs are obtained. Unless stated otherwise, we consider $R_{\min} = 2$ Mb/s as the minimum rate for direct connection between a UE and a BS.

Accordingly, a UE will be associated with a BS that provides the highest data rate. Fig. 6.2 illustrates the optimized locations of BSs among randomly and uniformly distributed UEs. The UEs marked with red circles do not satisfy the minimum rate requirement for any BSs. Therefore, they will be served by the CS through HAPS-RIS. Following the standardized 3GPP channel model established for a HAPS and terrestrial nodes in urban environments [7, Sec. 6], and the scattering reflecting paradigm of the RIS as detailed in [103], the effective channel gains from the CS to all UEs in set $\mathcal{K}_2$ through the

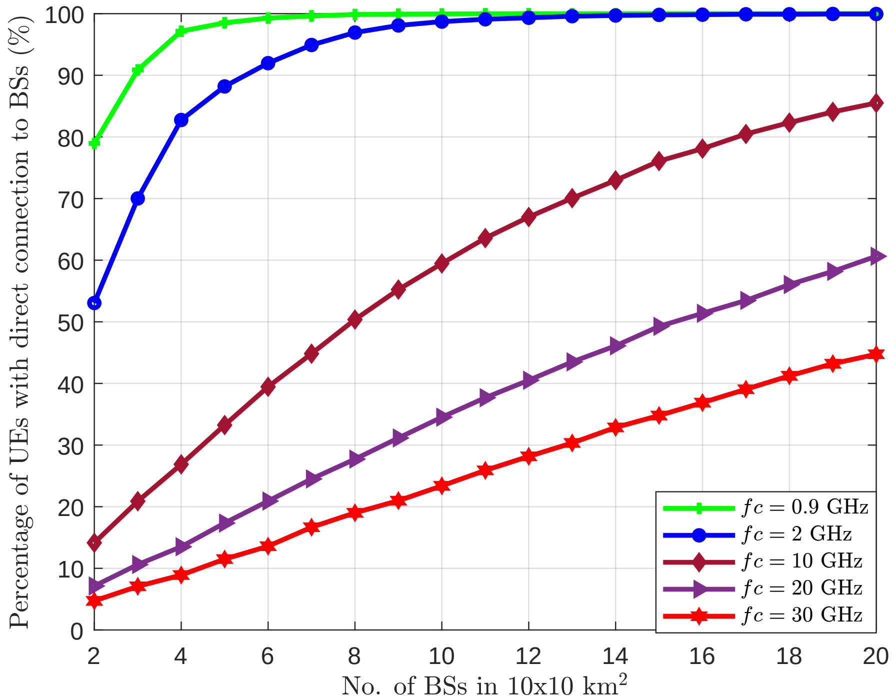

Figure 6.3: Relation between BS densities and percentage of UEs with direct connections for different frequencies.

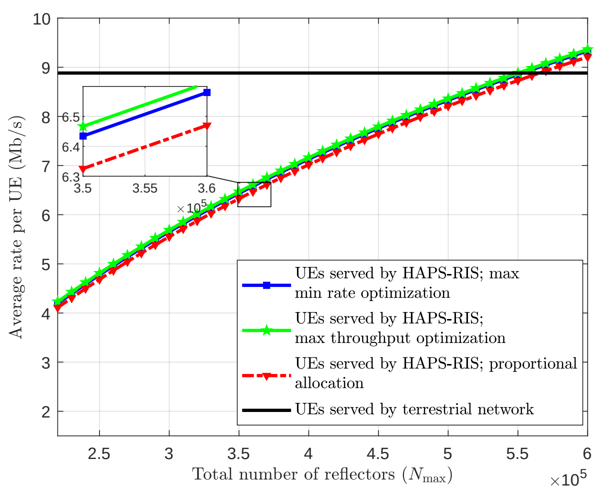

(a) Average UE rate.

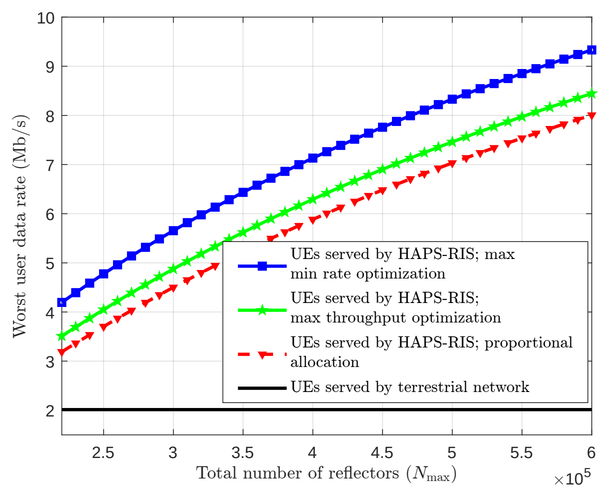

(b) Worst UE rate.

Figure 6.4: Comparison between terrestrial and HAPS-RIS communications with different allocation strategies.

HAPS-RIS are obtained (i.e., $\mathsf{PL}^{\text{CS}-\text{HAPS}}$ and $\mathsf{PL}^{\text{HAPS-}k}$). For this model, we consider dry air atmospheric attenuation. The atmosphere parameters are selected on the basis of the mean annual global reference atmosphere [97]. Further, we assume the UEs have 0 dB

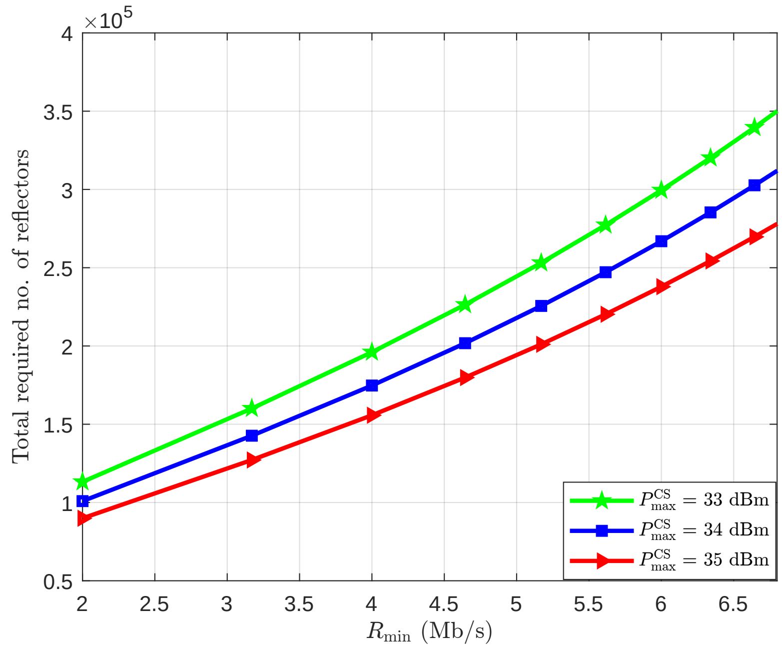

Figure 6.5: Relation between $R_{\min}$ for HAPS-RIS served UEs and the total required number of reflecting units.

gain, $N_0 = -174$ dBm/Hz, $B_{\mathrm{BS}} = 50$ MHz and $B_{\mathrm{UE}} = 2$ MHz. We further set $P_{\max}^{\mathrm{CS}} = 33$ dBm, and $G_{\mathrm{t}}^{\mathrm{CS}} = 43.2$ dB [7] in all of the simulations, unless otherwise stated.

6.7.1 Relationship between BS Density and Direction Connection with UEs

It should be noted that the percentage of UEs supported by the CS via the HAPS-RIS depends on the number of UEs that fail to connect with any terrestrial BS directly. The chances of UEs being supported by the BSs directly depends on the BS and UE densities and the carrier frequency. For a fixed density of BSs, as the density of UEs increases, the percentage of UEs with direct connections drops because the BSs cannot serve more users beyond their maximum loading capacities. Fig. 6.3 shows how the percentage of UEs with direct connections increases as the density of BSs increases. However, as the carrier frequency increases to provide high data rate communications, the percentage of UEs with direct connections significantly drops, even with the large number of BSs. For instance, four BSs communicating at $f_c \leq 2$ GHz are sufficient to support more than 80% of UEs directly connected to BSs, whereas more than 20 BSs are required to support 80% of UEs communicating at $f_c \geq 10$ GHz. Therefore, the HAPS-RIS may offer a more cost-effective solution in such situations than just increasing the density of the BSs.

6.7.2 Comparison Between Allocation Schemes

6.7.2.1 Sum rate and worst UE rate maximization based allocation

In this simulation, we set $N_{k,\min} = 1000$, $N_{k,\max} = 10,000$ reflectors and $P^{\mathrm{CS}}_{k,\min} = 15$ dBm and $P^{\mathrm{CS}}_{k,\max} = 20$ dBm.

Fig. 6.4 compares the achievable average and worst rate performances for the UEs belonging to set $\mathcal{K}_1$ and $\mathcal{K}_2$. For set $\mathcal{K}_2$, the performance plots are obtained using the optimized power and reflecting units allocation schemes and are compared with the *proportional* allocation strategy for benchmark purposes.

For the selected range of $N_{\max}$, i.e., 200,000 – 600,000 reflecting units[6], it can be observed that for most of the values of $N_{\max}$ the average rate of the terrestrial UEs is higher than that of the UEs supported by the HAPS-RIS (Fig. 6.4(a)). This is because the average performance is dominated by the excellent channel conditions between some UEs belonging to set $\mathcal{K}_1$ and the BSs. However, for HAPS-RIS to outperform RIS-assisted terrestrial networks in terms of the average rate, $N_{\max}$ should be more than 550,000 reflecting units. Because the rate performance of the worst UE is one of the concerns of network operators, we see in Fig. 6.4(b) that the rate performance of the worst UE assisted by HAPS-RIS is significantly higher than that are supported by the terrestrial networks.

For the UEs belonging to set $\mathcal{K}_2$, we observe that the *max throughput* allocation scheme achieved the best performance in terms of average UEs rate. However, in terms of the worst UE performance, the *max-min R* allocation scheme significantly improves the rate of the UE with the weakest channel gain, and it substantially outperforms the *max throughput* and the *proportional allocation* schemes. It should be noted that the improvement in the worst UE rate leads to the degradation of the sum and average UE rates. Since the *max min R* scheme distributes the system resources fairly and maximizes the fairness among all the UEs, it results in a performance loss for the whole system. It is interesting to note from Fig. 6.4 that the performance enhancement for the worst UE rate by *max min R*

[6] This is equivalent to an RIS area between 180 - 540 m^2. This can represent a partial area of a HAPS, as the length of an airship is between 100 and 200 m, whereas an aerodynamic HAPS has wingspans between 35 and 80 m. However, the size of each reflector unit is about $(0.2\lambda)^2$ [3].

scheme is about 15%, while the degradation in terms of the average rate or throughput is 1% less than the optimized *max throughput* allocation scheme.

6.7.2.2 Reflectors Minimization Based Allocation

Fig. 6.5 shows the variation of the minimum number of reflectors required with the different values of the minimum rate requirements of the UE. The number of reflectors and power P_k^{CS} corresponding to all $\mathcal{K}_2$ UEs that satisfy the minimum rate requirements are obtained by solving the problem (6.18a). As we can see, an almost linear relationship exists between the rate requirement and the minimum required number of reflectors. Moreover, by doubling the rate required for the UEs, the RIS unit requirement is increased by 100%. Fig. 6.5 also shows the relationship between the different values of the maximum transmit power available at the CS ($P_{\max}^{\mathrm{CS}}$) and the optimized number of reflectors. It can be observed that by increasing $P_{\max}^{\mathrm{CS}}$ by 1 dB, the minimum required number of reflectors is reduced by about 11%.

6.7.3 Resource-efficiency maximization

Fig. 6.6 plots the normalized RE obtained using Algorithm 4 (on the left-hand side y-axis) and the percentage of connected UEs (on the right-hand side y-axis) versus different values of minimum rate requirement $R_{\min}$. It also compares the performance of Algorithm 4 with the benchmark approach. The maximum number of RIS units mounted on HAPS is set to $N_{\max} = 220,000$ units. It can be observed that as the QoS (represented by $R_{\min}$) increases, the percentage of connected UEs and the RE drops. However, this performance degradation is more significant in terms of the percentage of connected UEs than the RE. Furthermore, we observed that the RE obtained using Algorithm 4 significantly outperforms the one obtained using the benchmark approach. This is due to the fact that Algorithm 4 optimizes allocation of both power and RIS units to UEs.

6.7.4 Percentage of connected UEs

Figs. 6.7 and 6.8 plot and compare the percentage of connected UEs obtained through Algorithm 4, the benchmark approach, and *within-cell* communication approach for different values of the number of RIS units $N_{\max}$ available at the HAPS, and maximum power $P_{\max}^{\mathrm{CS}}$ available at the CS, respectively.

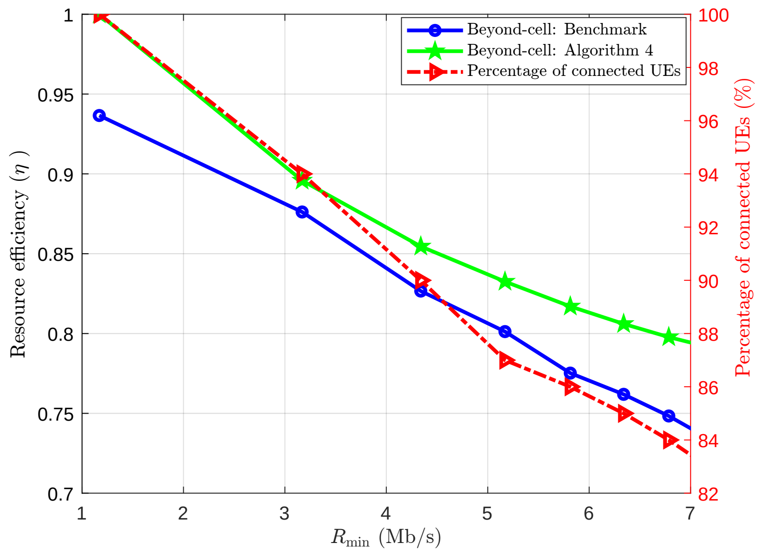

Figure 6.6: Resource-efficiency performance of connected UEs for different $R_{\min}$.

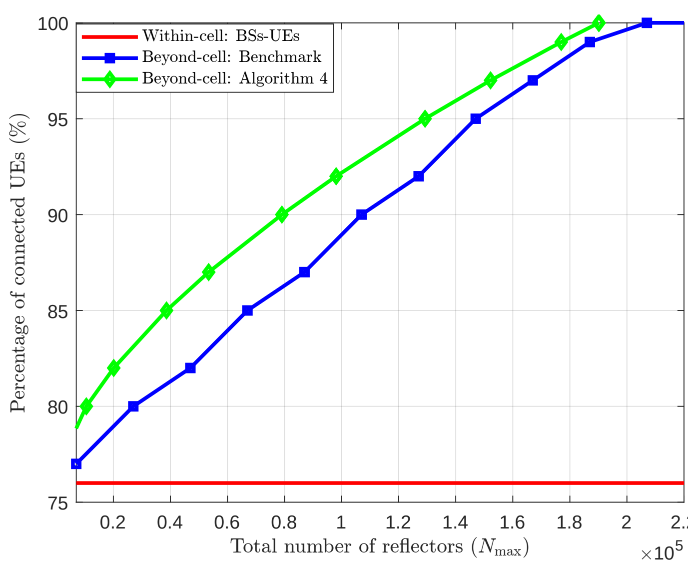

Figure 6.7: Maximizing connected UEs performance for different $N_{\max}$.

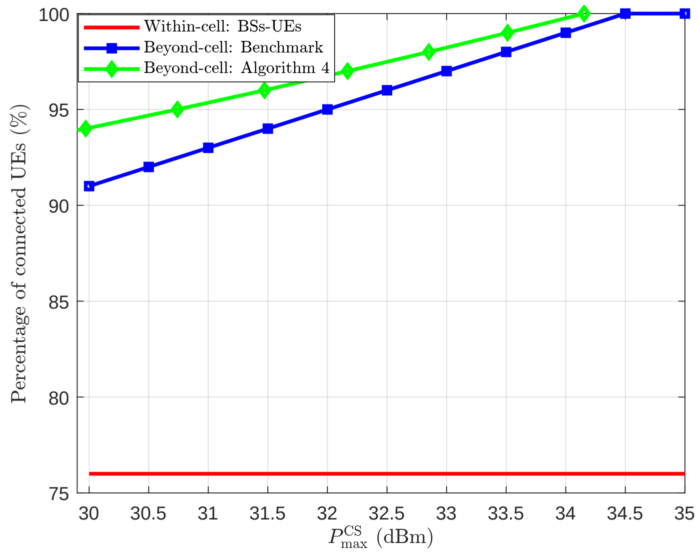

Figure 6.8: Maximizing connected UEs performance for different $P_{\max}^{\mathrm{CS}}$.

In Fig. 6.7, to study the impact of $N_{\max}$, we consider only the second term (i.e., $P_{\mathrm{RIS}}N_k$) of the objective function in (6.21a). The selected range of $N_{\max}$ is set between 10,000 and 220,000 units. This range corresponds to a total RIS area between 9 m^2 and 198 m^2 at carrier frequency of 2 GHz [7]. In Fig. 6.8, only the first term of (6.21a) (i.e., P_k^{CS}) is considered to study the effect of $P_{\max}^{\mathrm{CS}}$ on the percentage of connected UEs. The maximum transmit power of CS is set to vary between 30 dBm and 35 dBm, and $N_{\max}$ is set to 150,000 units. It can be observed from the figures that the percentage of connected UEs increases with the maximum power of the CS $P_{\max}^{\mathrm{CS}}$, and the maximum number of RIS units $N_{\max}$ (or the size of HAPS). These behaviors are intuitive as making available more system resources ($P_{\max}^{\mathrm{CS}}$ and $N_{\max}$) allow more number of stranded users to be served by the CS via HAPS-RIS.

Figs. 6.7 and 6.8 also show that the performance of the proposed approach is 1-3 % higher than the benchmark approach. Moreover, $P_{\max}^{\mathrm{CS}}$ has more significant impact than $N_{\max}$ on the percentage of connected UEs. By increasing $P_{\max}^{\mathrm{CS}}$ by 2 dB, the percentage of connected UEs increases about 4%, whereas doubling of the RIS size is needed to achieve the same increase in the percentage of connected UEs.

Furthermore, it can be observed from the figures that 76% UEs are served through

[7] This represents a limited area on a typical HAPS surface, as the length of an airship is between 100-200 m, whereas aerodynamic HAPS have wingspans between 35m and 80 m. The size of each RIS unit is $(0.2\lambda)^2$ [3].

within-cell communication approach, and the CS supports the remaining UEs via HAPS-RIS. Hence, *beyond-cell* communications via HAPS-RIS is able to complement TNs.

6.8 Conclusion

In this chapter, we introduced the novel concept of *beyond-cell* communications using HAPS-RIS technology to complement terrestrial networks by supporting unserved UEs. We formulated several resource allocation optimization problems to design the CS power and RIS unit allocation strategies. The optimization objectives included throughput maximization, max min rate, and minimal usage of RIS reflectors. In addition, given the limitations of the CS power and HAPS-RIS size, it might not be feasible to support all unserved UEs. Therefore, another novel resource-efficient optimization problem is formulated, which simultaneously maximizes the percentage of connected UEs using minimal CS power and RIS units. The results showed the capability of *beyond-cell* communications approach to support a larger number of users with a minimal number of terrestrial BSs. Furthermore, the results showed the superiority of the proposed solutions over the benchmark approach and demonstrated the trade-off between the total and average rate performance and the fairness among UEs. Finally, the results demonstrate the impact of the HAPS size and the QoS requirement on the percentage of connected UEs and the efficiency of the system. In the following chapter, we discuss the various options of HAPS communication payload and their associated applications. Then, we propose the multi-mode HAPS to increase its capabilities while minimizing its energy consumption.

Chapter 7

Multi-Mode HAPS for Next Generation Wireless Networks

7.1 Introduction

Beyond fifth-generation (B5G) and sixth-generation (6G) technologies are expected to support novel use cases thanks to their anticipated ubiquitous and reliable connectivity with a massive numbers of devices with high data rates and low latency. But it has been shown to be unfeasible and cost-inefficient to attempt to fulfill the requirements of future networks by relying solely on terrestrial networks. To complement terrestrial systems, non-terrestrial networks (NTN) are envisioned as a key enabler for next-generation networks. More specifically, given the intrinsic features of NTN, including flexible deployment, strong channel links, and wide coverage footprints, the latter can support terrestrial networks by enhancing aspects such as communication, computing, and caching capabilities.

Typically, three types of NTN systems are proposed to support future networks, namely unmanned aerial vehicles (UAVs) [108], high altitude platform station (HAPS) systems [3], and low-Earth-orbit (LEO) satellites [109]. These NTN systems have different features

This main content in this chapter was submitted to IEEE global competition of the NTN for beyond B5G and 6G, organized by the IEEE Future Networks Initiative and sponsored by Communications and Information Technology Commission (CITC), Saudi Arabia. This work was awarded the grand prize during the "*Connecting the World from the Skies*" forum in Riyadh, Saudi Arabia (Nov 8-Nov 10, 2022).
Also, this work was submitted to IEEE VTC magazine: **S. Alfattani**, W. Jaafar, H. Yanikomeroglu, and A. Yongacoglu, "Multi-mode high altitude platform stations (HAPS) for next generation wireless networks", under review in *IEEE Vehicular Technology Magazine* , (submission: 17 Sep 2022).

such as operating altitude, size, payload, flight duration, and communication capabilities. While UAVs are limited by energy consumption and flight time, LEO satellites suffer from significant path loss, high mobility, and long communication delays. By contrast, HAPS systems have the largest platform size and payload, less path-loss and delay than LEO satellites, and they can sustain longer missions than UAVs. Accordingly, the development of HAPS technologies has attracted significant interest from both academia and the industry [69, 3, 110]. Examples of current HAPS projects include X-station by StratXX, Zephyr by Airbus, Stratobus by Thales, Hawk30 by HAPSMobile, and Phasa-35 by BAE Systems.

One of the main issues in HAPS research is the design of the communication payload subsystem, as it impacts the range of supported applications, energy consumption, flight duration, and deployment costs. Traditionally, HAPS were developed to serve rural and hard-to-reach areas, and the communication payload was designed in a single mode to operate either as a base station (HAPS-BS) or as a relay station (HAPS-RS). An advanced HAPS-BS, referred to as HAPS super macro base station (HAPS-SMBS), was recently proposed in [89], where it was used in urban areas for novel applications beyond connectivity, such as computing, storage, and sensing. Similarly, an energy-efficient version of a HAPS-RS was proposed and analyzed in chapters 4–6, where a HAPS is equipped with a reconfigurable intelligent surface (RIS), aiming to provide relaying functions. The latter is called HAPS-RIS.

Nevertheless, designing a HAPS with a single payload mode either increases its energy consumption or limits its communication capabilities. Hence, to cope with the user traffic and service demand dynamics in the most efficient and cost-effective manner, we propose here the design of a multi-mode HAPS payload, where the HAPS can adaptively switch between different operating modes, i.e., HAPS-SMBS, HAPS-RS, and HAPS-RIS, based on the received demands. Consequently, the usage of active components on the HAPS will be minimized and a more energy-efficient operation achieved.

7.2 HAPS versus other NTN Systems

In comparing HAPS and other NTN systems supported by UAVs or LEO satellites, we discuss their differences in terms of communication payload capabilities, and suitable applications.

7.2.1 HAPS versus LEO Satellites

HAPS systems have unique properties compared to LEO satellites. First, HAPS are typically located at an altitude of 20 km, whereas LEO satellites are deployed at altitudes between 350 and 2000 km. Hence, a HAPS experiences less communication path-loss and stronger line-of-sight (LoS) links. The high quality of its communication link to the ground allows it to connect directly to the user equipment (UE) without requiring a special receiver design. This is in contrast to LEO systems, where sophisticated receivers with high antenna gain are required. Also, due to its low altitude, a HAPS is more appealing for delay-sensitive and critical applications than a LEO satellite.

Second, HAPS systems are quasi-stationary, whereas LEO satellites orbit the Earth at high speeds. Thus, unlike HAPS, satellites suffer from Doppler effects, frequent handover and wasted capacity due to orbiting through under-populated areas for a part of its trajectory. Moreover, due to the continuous movements of LEO satellites, a tracking system in the receiver is required.

Third, HAPS are giant platforms. Typically, aerostatic HAPS (e.g., airships) have lengths between 100 and 200 m, while aerodynamic HAPS have wingspans between 35 and 80 m. This is up to 20 times the size of a standard LEO satellite. Such HAPS sizes allow accommodating several communication technologies, including massive MIMO and large RIS. Moreover, HAPS can host heavier payloads, e.g., storage and computing equipment.

Finally, the lifetime of HAPS is estimated to be between a few months and several years, depending on the nature of its mission. Although this is lower than the LEO satellite lifetime, HAPS offer other advantages. Indeed, they are recoverable at the end of their lifetime, unlike satellites. Moreover, HAPS can be maintained either in the sky or by bringing them back to Earth, which makes it possible to extend their lifetime.

7.2.2 HAPS versus UAVs

Although UAVs can communicate with ground UEs over small distances of up to a few hundred meters while ensuring reliable and low-latency communications, HAPS systems outperform UAVs in several other aspects. First, due to the higher altitude of HAPS, they enjoy a wider footprint radius ranging between 40 and 100 km for high throughput communications, and this can be extended to 500 km (ITU-R F.1500). By contrast, the coverage footprint of UAVs is very small, which requires the deployment of costly swarms of UAVs in large areas. Also, a better LoS probability can be realized with HAPS, while UAV links are sensitive to blockages and high-rise buildings.

Second, given that HAPS are mainly powered by renewable energy sources, e.g., solar panels, whereas UAVs rely on limited battery capacities, HAPS can sustain multiple and longer missions than UAV systems.

Finally, the small size of UAVs limits their communication payload and potential applications. For instance, authors of [103] showed that RIS-equipped UAVs perform worse than RIS-equipped HAPS. For the same reason, high storage and computation power cannot be deployed on UAVs, in contrast to HAPS.

7.3 Single-Mode HAPS Communication Payload

A HAPS consists of three onboard subsystems: an energy management subsystem, a flight subsystem, and a communication payload subsystem [3]. The energy management subsystem is responsible for power generation using photovoltaic (PV) panels, and for energy storage through Lithium-ion batteries or fuel cells. Moreover, this subsystem controls the energy consumption required by the other subsystems. The flight subsystem controls the mobility and stabilization of the HAPS, whereas the communication payload subsystem mainly manages the communications between the HAPS and other aerial or terrestrial nodes, while also processing and storing other required data. Based on the capabilities of the HAPS in terms of communication, computing, and storage, its power requirements and applications may vary. Typically, three types of HAPS communication payload have been defined, namely HAPS-SMBS [89], HAPS-RS, and HAPS-RIS[69, 103]. The type of communication payload impacts the potential applications supported, onboard consumed energy, and thus the flight duration of the HAPS. In what follows, we discuss the properties and potential use cases of each HAPS-equipped communication payload type.

7.3.1 HAPS-SMBS

The main role of the HAPS-SMBS communication payload involves radio frequency (RF) filtering, frequency conversion, and signal amplification. Its multiple antennas transceivers can also encode/decode, precode and modulate/demodulate signals, as well as switch and route data. The communication payload of the HAPS-SMBS used exclusively for communications is called a "*regenerative payload*" by the 3rd Generation Partnership Project

(3GPP) standards (TR 38.811), and it supports similar tasks to a ground base station or a Node B (gNB). A HAPS-SMBS's "*regenerative payload*" can fully process signals and serve users directly, unlike other communication payload types.

When the communication payload of a HAPS-SMBS integrates computation and caching capabilities, its role can be extended beyond simple data transmission and reception for users in rural and underserved areas. Indeed, HAPS-SMBS can work in tandem with terrestrial networks in dense urban areas to provide numerous applications and novel services for 5G and beyond networks. We discuss some unique HAPS-SMBS use cases below.

7.3.1.1 Increasing network capacity

To cope with the increasing demands in metropolitan areas, network operators have traditionally relied on densification with macro and small gNBs. However, this might not be a cost-effective solution in dynamic and highly mobile environments. In addition, small-cell densification might not be sufficient to absorb the ever-increasing traffic of connected devices. Moreover, the fixed deployment of terrestrial networks is unable to handle unpredictable congestion caused by temporary events. To tackle this issue, a HAPS-SMBS can complement a terrestrial network by providing wide coverage, continuous, and agile connectivity to the terrestrial network's cell-edge and high-traffic demanding UEs.

7.3.1.2 Supporting aerial networks and aerial users

The deployment of UAVs as BSs or relays is seen as a key enabler of future networks, given the flexibility and mobility of UAVs. However, their processing and computation powers are limited, and so they may not be able to execute all required tasks. Hence, UAV-BSs can rely on a HAPS-SMBS to offload their tasks and serve as a reliable computing/storage server. On the other hand, the massive deployment of UAV users (UAV-UEs) is envisioned in the near future for numerous applications such as mail/package delivery, search and rescue, and traffic monitoring [111]. However, supporting and managing UAV-UEs through current gNBs might not be practical, since they are designed to serve ground UEs. But a HAPS-SMBS would be able to manage UAV-UE swarms and support their command and control functions.

7.3.1.3 Supporting intelligent transportation systems

Intelligent transportation system (ITS) is a paradigm shift that encompasses technologies such as IoT networks and connected autonomous vehicles (CAVs). This shift aims to enhance the safety, mobility, productivity, and comfort of transportation. Efficient ITS services require the implementation of several tasks, such as traffic and road condition monitoring, accident reporting, and vehicle platooning, which depends on the availability of connectivity, computing, and storage capabilities along roads and highways. In this context, given a HAPS-SMBS's mobility, sustainability, and communication payload capacity, it is envisioned as a key enabler of future ITS services, particularly on highways [110].

7.3.1.4 Providing aerial datacenter services

Given the high payload of a HAPS-SMBS, which is up to a few hundreds of kilograms [3], it can host datacenter equipment to support intensive computation applications, such as virtual/augmented reality (VR/AR). Hence, IoT and low-power devices can offload their computation tasks to the HAPS-SMBS. Also, in case of a terrestrial infrastructure failure, the HAPS-SMBS can provide backup storage and computing services.

7.3.2 HAPS-RS

The HAPS-RS can be seen as a lighter version of the HAPS-SMBS. As such, it focuses only on communications and thus consumes less power than the HAPS-SMBS. This is mainly due to the absence of the energy-greedy computing and caching functionalities. HAPS-RS's payload is referred to as a "bent pipe payload" (TR 38.811), whose functions are limited to RF filtering, frequency conversion, and signal amplification. Typically, a HAPS-RS ensures communications through a ground gateway. Hence, any communication to/from a ground user has to go through two links, namely the gateway-HAPS-RS link and the user-HAPS-RS link. Compared to the previous mode, the propagation delay in the HAPS-RS mode is longer. Accordingly, a HAPS-RS supports lighter applications than a HAPS-SMBS, such as:

7.3.2.1 Backhauling traffic from small cells

Wired backhauling infrastructure might not be cost-effective for small cells, especially in rural or hard-to-reach areas due to limited population sizes and the high cost of connecting such areas to the core network through fiber links. In such cases, a HAPS-RS can ensure the connectivity of small BSs to the core network using RF or free-space optical (FSO) links for higher backhaul capacity.

7.3.2.2 Supporting IoT networks

IoT and massive machine type communications have been promoted as key enablers of future industrial networks. IoT devices are expected to be widely deployed even in areas with limited cellular coverage, such as highways, forests, and oceans. For these particular environments, connectivity through satellites has been previously adopted. However, relying on satellites may be suitable only for delay-tolerant applications, while services with stringent quality-of-service (QoS) demands would require a more effective solution. To satisfy such demands, a HAPS-RS can be leveraged for IoT data collection and forwarding to the ground control center through its gateway.

7.3.2.3 Establishing and maintaining inter-HAPS links

To support connectivity over wide areas, such as countries and trans-continental highways, several HAPS-RS nodes can be deployed. Together, the nodes can form a HAPS constellation with several gateways and inter-HAPS links to enable mesh networking among them and bypass any failure within the constellation. These inter-HAPS links can be achieved through the HAPS-RS mode using either RF or FSO signals [110].

7.3.3 HAPS-RIS

Both HAPS-SMBS and HAPS-RS require active communication payloads, which consume considerable amounts of energy. Although a HAPS-RS consumes less energy than a HAPS-SMBS, the energy consumed by the former nevertheless impacts the operating lifetime of the HAPS. To further reduce power consumption and extend the loitering time of HAPS, a passive communication payload can be utilized. Passive communication payloads have already been adopted in satellites, such as the Echo satellite, the Lincoln calibration sphere, and the Passive Geodetic Earth Orbiting Satellite (PAGEOS), launched in 1960, 1965, and 1966, respectively, and all using passive reflective satellite surfaces. Nevertheless, due to the high altitude of these satellites, applications were limited to low-rate and delay-tolerant ones.

Recently, RIS has attracted interest as a novel passive communication technology. More specifically, RIS is a nearly passive technology that uses massive reflective elements to alter and reflect the incident RF signals through phase shifting. Since RIS phase shifting can be smartly and dynamically adjusted, the RIS performs better than conventional passive reflection [69]. Also, due to the absence of RF chains in RIS, it is more energy-efficient than conventional relays.

Given the opportunities offered by RIS, its integration into HAPS as a light communication payload has been discussed in chapter 4 and presented in previous works [69, 103]. A comparison between HAPS-RS and HAPS-RIS conducted in chapter 4 (Table 4.1) has shown that HAPS-RIS is more energy-efficient and cost-effective. Moreover, most of the applications targeted by HAPS-RS, such as backhauling, supporting IoT systems, and inter-HAPS links, can be handled by HAPS-RIS. Other use cases can be also listed, including the following:

7.3.3.1 Securing communications

Due to its unique properties for signal manipulation, including reflection and absorption, RIS can be used to enhance physical layer security (PLS). This was studied in UAV systems [112], where a UAV-RIS trajectory was jointly optimized with phase shifting to maximize the secrecy energy efficiency. The results demonstrated the UAV-RIS's ability to enhance secure energy efficiency by up to 38% compared to a benchmark without an RIS. With HAPS-RIS, PLS can be extended to large areas where legitimate signals are focused towards their users, while nulling the signals' energy in an eavesdropper's direction. Also, HAPS-RIS can send jamming signals to an eavesdropper to prevent decoding legitimate signals. Finally, HAPS-RIS can block the jamming signal of an attacker through signal absorption.

7.3.3.2 Supporting beyond-cell communications

In dense urban environments, communication links between gNBs and users may be degraded because of blockages or overloaded gNBs. To bypass these issues and connect

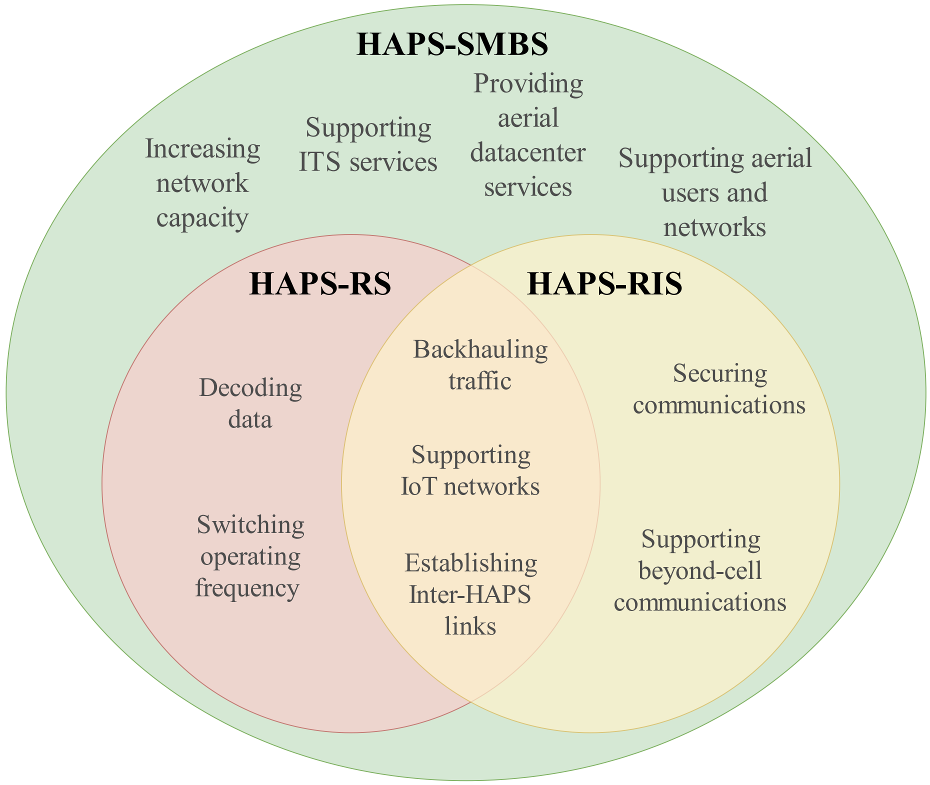

Figure 7.1: Relation between applications and enabling HAPS modes.

dropped users by the gNBs, HAPS-RIS can be leveraged to connect those users through a dedicated ground station [113].

7.4 Proposed Multi-Mode HAPS Communication Payload

As discussed in the previous section, based on the HAPS payload type, different applications and use cases can be realized. The relation between a payload type and the suitable applications is shown in Fig. 7.1. In general, as more active elements and processing power are included in HAPS payload, more use cases can be served. However, this will inevitably increase energy consumption and limit the mission duration. Also, demands may change dynamically, and so deploying a single-mode HAPS may not be cost-effective.

To overcome the limits of a single mode payload, we propose a multi-mode HAPS payload, where both passive and active components can be integrated. For the passive

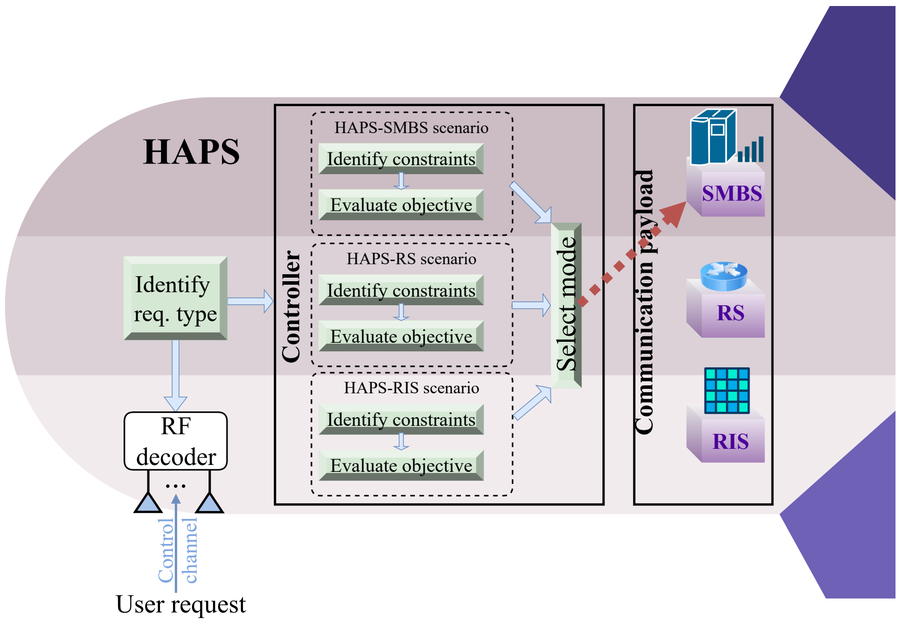

Figure 7.2: HAPS mode selection mechanism.

payload, RIS layer can be integrated on the underside of HAPS. Also, active components for signal processing and channel estimation can be included. The active elements can be remotely controlled and switched ON/OFF opportunistically based on the use case demands and the application requirements. The functioning mechanism of the multiple HAPS payload can be either based on a mode selection or cooperation-based approach. While a mode selection based approach maximizes the energy efficiency, a cooperation-based approach enhances reliability and communication performance.

7.4.1 HAPS Mode Selection

The mode selection mechanism is summarized in Fig. 7.2. We assume that the HAPS has a control circuit that exploits a low-power control channel to receive user requests. Whenever a request is received, the HAPS starts identifying the nature of the request among different types, such as *communication*, *content delivery*, *caching* or *task-offloading/computation*.

For a communication request, all modes compete among each other to maximize/minimize a predefined objective. For instance, assuming that the objective is to minimize the HAPS's communication energy consumption in a backhauling scenario, then the HAPS-RIS mode might be selected if it satisfies the QoS requirements with minimal energy. If the objective is to maximize the backhauling capacity, then based on HAPS's location, available energy, and RIS size constraints, the best mode can be determined.

When a content delivery request is received, the HAPS checks if it is able to satisfy it directly, i.e., if it has previously cached the content. If this is the case, then the HAPS-SMBS mode is activated and it precodes the content to send it to the user. Otherwise, HAPS-RS or HAPS-RIS mode is activated to forward the content from the core network to the user, via its ground communication gateway. If the pulled content is highly popular, HAPS-SMBS mode is switched on to proactively cache the content for future use.

Finally, when a task offloading/computing request is received, the HAPS-SMBS mode evaluates its capacity to process the task and resulting energy consumption, given the task offloading latency constraint. In the meantime, both HAPS-RS and HAPS-RIS modes optimize their objectives if the task is forwarded to an available ground cloud/fog/edge server. The mode that is expected to achieve the best objective performance will be chosen.

7.4.2 Benefits

A multi-mode HAPS presents several benefits. First, through its ability to adaptively switch between modes, it ensures that the active components are used only for particular demands and use cases. Hence, passive components are often used, which significantly reduces energy consumption, and this ultimately extends the HAPS flight duration. Moreover, the availability of multiple modes guarantees robustness against equipment failure. For instance, if the active radio transceivers required for the HAPS-SMBS and HAPS-RS modes fail, the HAPS-RIS mode can take over temporarily, until the faulty equipment is fixed. Finally, performance can be enhanced through the combination of several modes. For instance, by using RIS at the SMBS transmitter, reliable and high order modulation signals can be transmitted in an energy-efficient manner [103]. Also, by simultaneously using the RIS and RS modes for signal forwarding and selection combining at the receiver, the communication performances in terms of capacity and outage probability are expected to improve, as demonstrated for RIS and RS equipped UAV systems [114].

7.4.3 Challenges and Research Directions

The design of an efficient multi-mode HAPS switching mechanism is a challenging task. The mechanism needs to consider several parameters, e.g., user locations, channel state information (CSI), type of demand, current caching and computing status of the HAPS and cloud server, which may not be all available in a timely manner for a rapid switching decision. Consequently, the mode selection strategy has to rely on partial or no prior knowledge of these parameters, and it must make decisions rapidly and be adaptable to the environment's traffic and mobility dynamics. To cope with these conditions, centralized or decentralized machine learning-based mode selection can be developed and evaluated.

Moreover, since computing and caching are supported by the HAPS-SMBS mode, problems of task offloading to the cloud and reactive/proactive caching at the HAPS must be rigorously treated. Although conventional solutions to task offloading and caching can be adopted, their development in the context of HAPS systems is still in its infancy [115, 116].

Finally, mode switching may seem straightforward when aiming to satisfy a single demand or homogeneous demands. However, operating a multi-mode selection to satisfy heterogeneous demands may become difficult and very complex, since one mode may be adequate for a set of demands, but not necessarily for a different set. Consequently, more advanced mode selection approaches should be developed while taking into account the heterogeneity of demands. A combination of multiple access techniques [117] and simultaneous activation of different modes may be considered in such conditions.

7.5 Case Study

In this case study, we discuss the differences between HAPS communication modes in terms of capacity, energy efficiency, and latency. Also, we identify the conditions favorable to the selection of one specific mode over another.

7.5.1 HAPS-RS versus HAPS-RIS

We consider a backhauling scenario for traffic from a gNB located at 60 km away from its core network gateway, via a HAPS-RS or a HAPS-RIS. We assume that the gNB is equipped with two antennas: The first serves terrestrial users, while the second ensures communication with the HAPS. We assume that the gNB's transmit power and antenna gain are $P_{\mathrm{gNB}} = 35$ dBm and $G_{\mathrm{gNB}} = 15$ dB, respectively (TR 136.942). The gateway uses a highly directional antenna to communicate with the HAPS, having maximum power and gain set to $P_0^{\max} = 33$ dBm and $G_0^{\max} = 43.2$ dB, respectively (TR 38.811). For the HAPS-RS, we assume that it is equipped with a half-duplex decode-and-forward relay that has

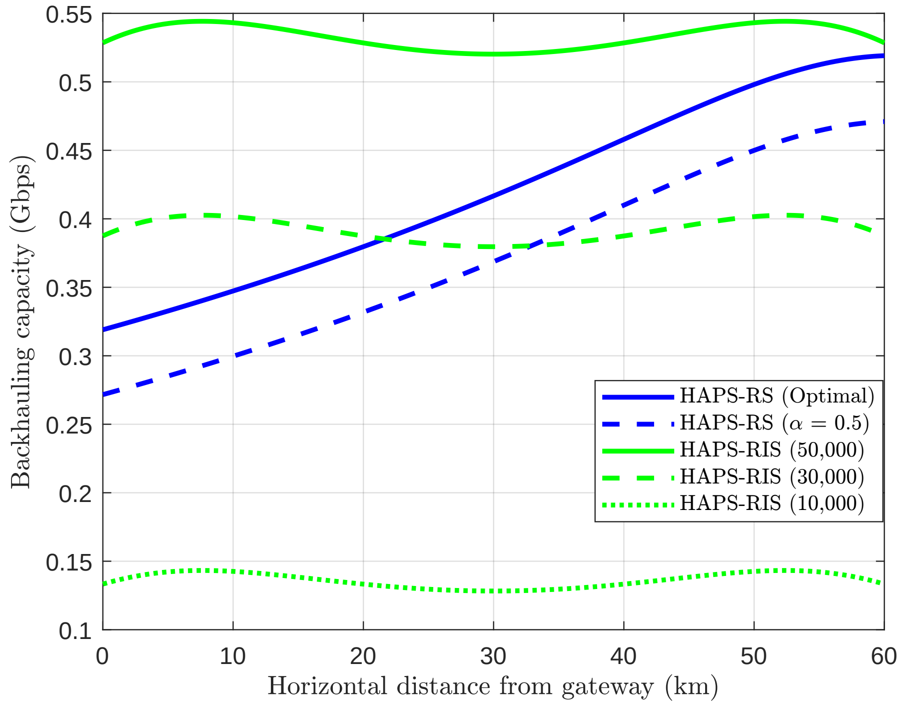

Figure 7.3: Backhauling capacity comparison between HAPS-RS and HAPS-RIS.

antenna gain $G_{\mathrm{RS}} = 15$ dB, while its payload power consumption is up to 1 kW, as specified for the X-Station HAPS developed by StratXX. Finally, for the HAPS-RIS communication payload, power consumption is issued from RIS phase-shifting, which depends on the used technology and phase-shift resolution. Typically, a 6-bit phase-shifting resolution would consume around 7.8 mW per RIS reflecting element [118]. Thus, its total consumption is $N \times 7.8$ mW, where N is the number of reflecting elements.

For a fair comparison between the HAPS-RS and HAPS-RIS, we respect the power conservation principle. Specifically, the gateway's transmit power in the HAPS-RIS scenario ($P_0^{\max}$) is equal to the sum of transmit powers of the gateway ($P_0 = \alpha P_0^{\max}$) and relay ($P_{RS} = (1-\alpha)P_0^{\max}$) in the HAPS-RS scenario, where $0 < \alpha < 1$. Finally, we set the operating frequency to 2 GHz, while the details of the channel and capacity calculations are provided in [103].

Fig. 7.3 illustrates the backhauling capacity performance of the HAPS-RS and HAPS-RIS as a function of the horizontal distance between the HAPS and gateway, where the horizontal distance is measured between the projection of the HAPS location on the ground and the gateway's location. For the HAPS-RS, we evaluated the capacity for fixed $\alpha = 0.5$ and optimal α, i.e., the one that achieves the best performance, while for the HAPS-RIS,

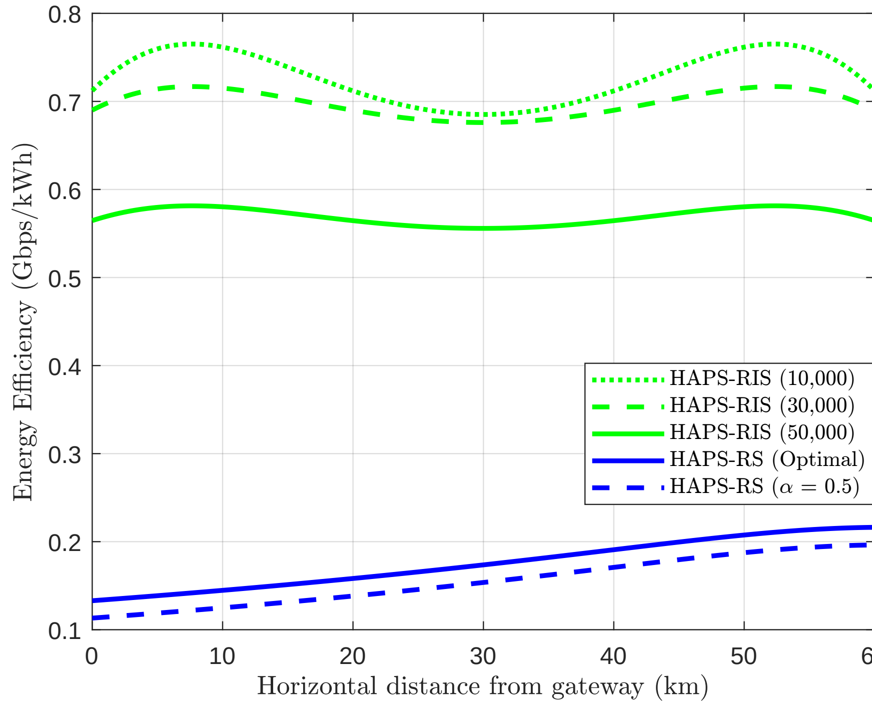

Figure 7.4: Energy efficiency comparison between HAPS-RS and HAPS-RIS.

we evaluated the capacity for $N \in \{10000, 30000, 50000\}$. As the distance from the gateway increases, i.e., HAPS gets closer to gNB, the HAPS-RS demonstrates a performance improvement with a maximal capacity achieved when it is on top of the gNB. Indeed, the decoding efficiency of the HAPS-RS improves when it gets closer to the gNB, while the gateway and its high antenna gains compensate for the degarded communication link between the HAPS-RS and the gateway. When $\alpha = 0.5$, the capacity is degraded by 11%, compared to the optimal case. Using the HAPS-RIS instead, we notice that two optimal locations are identified at distances of 6.9 km and 52.3 km. This result agrees with our findings in [103]. Also, the backhauling capacity enhances with N. This is expected since a higher number of carefully configured reflecting elements N allows the HAPS to generate a stronger reflection gain. From the backhauling capacity perspective, the mode selection between HAPS-RS and HAPS-RIS depends on several parameters, namely the HAPS's location and N. For instance, if $N = 30000$, the HAPS-RS mode would be preferred when the horizontal distance from the gateway is above 21.5 km, while the HAPS-RIS mode would be recommended if the HAPS were closer to the gateway.

Fig. 7.4 presents the related energy efficiency performance, defined as the ratio between the backhauling capacity and consumed energy. As we can see, the HAPS-RIS performs

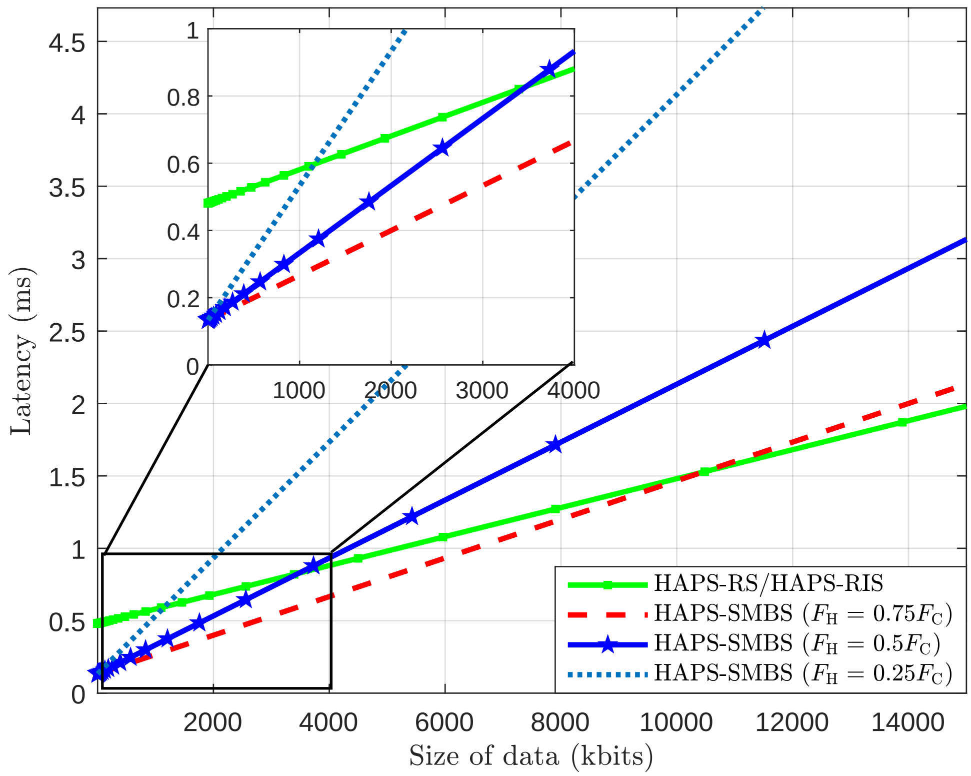

Figure 7.5: Latency comparison between HAPS-SMBS and HAPS-RS/HAPS-RIS.

better for any N and location, due to the power consumption of the RIS being lower than that of active relaying. Finally, as shown in Figs. 7.3– 7.4, HAPS-RIS mode demonstrates small performance variations with distance (around 5%), which make it more resistant to location drifting than the HAPS-RS mode.

7.5.2 HAPS-SMBS versus HAPS-RS/HAPS-RIS

We consider here a task-offloading scenario where a gNB can offload its task to the HAPS or to the cloud. Specifically, the HAPS-SMBS mode allows processing tasks using its onboard computation and caching capabilities, while the HAPS-RS/HAPS-RIS forwards the tasks to the gateway for processing within the cloud. Nevertheless, due to the relatively limited payload of the HAPS-SMBS, its computational capability F_H (in CPU cycles/second) is typically lower than that of the cloud, denoted by F_C, while its communication latency is lower than that of the HAPS-RS/HAPS-RIS systems since the latter must reach the cloud via the ground gateway. The summation of the two, i.e., computation and communication latencies, defines the task-offloading latency.

In Fig. 7.5, we compare the performance in terms of task-offloading latency for the HAPS-SMBS and HAPS-RS/HAPS-RIS systems as a function of the task's data size, and given different values of F_H. For these simulations, we considered the same assumptions as in the previous subsection, except for the location of the HAPS, which is optimized according to the adopted mode. Also, we assume that $F_C = 4 \times 10^9$ CPU cycles/second, and that each data unit requires 4 CPU cycles to be processed. Accordingly, we see in Fig. 7.5 that any mode's latency performance degrades linearly with the data size. Moreover, the HAPS-SMBS is the preferred mode for small data sizes, while HAPS-RS/HAPS-RIS modes are recommended for large data sizes and $F_H < F_C$. To conclude, the selection of the mode for task-offloading depends on several parameters, including the data size, HAPS location, F_H, and N.

7.6 Conclusion

In this chapter, we proposed a novel HAPS operating mechanism where the communication payload could switch between multiple modes, namely SMBS, RS, and RIS. First, we compared the HAPS features to those of other NTN systems, followed by a discussion about each HAPS mode, its characteristics, and potential applications. Then, we proposed our multi-mode HAPS vision, where the related mode selection mechanism, benefits, and potential challenges, were presented. Subsequently, we developed a case study to evaluate the performances of each HAPS mode and to identify the auspicious conditions for the selection of a specific mode among the available ones.

Chapter 8

Summary and Future Work

8.1 Summary

B5G networks will be a paradigm shift in wireless communication networks. They will support a wide range of use cases and novel applications. Several enabling technologies were introduced to achieve the vision and fulfill the goals of future wireless networks. These enabling technologies including IoT networks, aerial and stratospheric platforms, and reconfigurable intelligent surfaces. Rather than utilizing and studying the potentials of the aforementioned technologies separately, we focused in this dissertation on the integration of these technologies. Thus, the benefits of each technology will be reinforced and hence more use cases and applications can be supported. In this dissertation, several problems associated with the integration between these technologies were studied.

Since WSNs are the basis of IoT networks, we proposed in Chapter 2 a framework for data collection in WSNs using multiple UAVs. The framework aimed to collect data in the shortest time and at the lowest cost, in terms of deployed cluster heads and UAVs. Specifically, we used clustering to optimize the number and locations of cluster heads. Then, we leveraged heuristic solutions to mTSP and TSPN to obtain optimized number and trajectories of UAVs. Simulation results provide guidelines for data collection design in WSNs including clustering approach and requirements, and UAVs trajectory design. For the trajectory planing, the heuristic GA was shown to be near-optimal with only 3.5% degradation. By considering the UAVs coverage areas in determining the UAVs hovering locations of visited CHs, data collection times can be minimized. In addition, the data collection time is significantly affected by the environment and the UAV altitude. Finally, the importance of fairness measure in designing the trajectories of multiple UAVs in large WSNs is discussed.

Following the data collection framework presented in Chapter 2, we proposed in Chapter 3 an improved clustering algorithm to optimize the number and locations of CHs, which gather data from associated IoT sensors. Then, we optimized the UAVs trajectories taking into account the IoT network deadlines and the UAVs energy constraints. Simulation results show the efficiency of the proposed clustering algorithm which outperforms baseline approaches. Moreover, we showed that moving CHs closer to the dockstation provided a significant energy saving. On the other hand, the trajectory planning was formulated as a CVRPTW problem, and several heuristic approach were utilized to solve it. By comparing different trajectory designs including Tabu search, gradient descent and simulated annealing, it is shown that Tabu search achieves the best UAV trajectory design. Finally, we studied in this Chapter the impact of the battery capacity and time deadline in terms of energy consumption, number of visited CHs, and number of deployed UAVs.

Given the limited energy issue of UAVs, discussed on Chapter 3, which limit their flight duration, we proposed in Chapter 4 the integration of an energy-efficient communication payload on aerial and stratospheric platforms. In this chapter, we introduced our vision for integrating RIS technology into aerial platforms as a novel B5G paradigm. In this chapter, an overview of RIS technology, its operations, and types of communication were provided. Then, a control architecture for RIS-equipped aerial platforms was proposed. We discussed further potential use cases for integrating RIS on HAPS, UAVs and tethered balloons. These use cases include backhauling, IoT data collection and supporting terrestrial and aerial users. The main advantages achieved by integrating RIS in aerial platforms are energy efficiency, lighter payload, and lower system complexity, which results in extended flight durations and more cost-effective deployment. Finally, we discussed several challenges and research problems related to this integration.

Following our vision of integrated RIS in aerial platforms presented in Chapter 4, we discuss in details in Chapter 5 the link budget analysis for RIS-equipped HAPS, UAVs and LEO satellites. We presented two reflection paradigms, namely, specular and scattering reflection, and discussed their realization conditions. Also, we derived the optimal location for RIS-equipped platform under each reflection paradigm. The performance of RIS-assisted aerial platforms was evaluated using 3GPP standards for the channel models. The obtained numerical results provided important insights and design guidelines:

- While specular reflection has better performance, the scattering paradigm is gaining more interest in the research community due to its practical accuracy.

- HAPS-RIS has superior performance in different types of environments, compared to terrestrial and other aerial platforms.

- The received power performance is limited by the sizes of the RIS surface and reflector unit.

- The link budget of the scattering refection paradigm becomes independent from the carrier frequency, when the maximal number of reflectors in a surface is utilized.

- Supporting ground users with RIS-equipped LEO satellites or a single UAV might not be feasible. Nevertheless, RIS can be used to assist inter-UAV or inter-LEO communications. Also, a swarm of RIS-equipped UAVs can support terrestrial users.

- Finally, the best RIS-equipped platform location significantly depends on the operating altitude, coverage footprint, and environment type.

Based on the potentials of HAPS-RIS demonstrated in Chapters 4 and 5, we introduced in Chapter 6 the concept *beyond-cell* communications , where HAPS-RIS is utilized to complement terrestrial networks by supporting unserved UEs. Several resource allocation optimization problems were formulated to design the CS power and RIS unit allocation strategies. The optimization objectives included throughput maximization, max min rate, and minimal usage of RIS reflectors. Besides, for an area with a large number of UEs or covered by a limited size of HAPS-RIS, we proposed a resource-efficient approach for maximizing the percentage of connected UEs using minimal CS power or RIS units. The results showed the capability of *beyond-cell* communications approach to complement terrestrial networks and support unserved UEs with a minimal BSs density. Furthermore, the results showed the superiority of the proposed solutions over the benchmark approach and demonstrated the trade-off between the total and average rate performance and the fairness among UEs. Finally, the results demonstrate the impact of the HAPS size and the QoS requirement on the percentage of connected UEs and the efficiency of the system.

Given the differences between HAPS communication payload in terms of capabilities and energy requirements, we propose in Chapter 7 a novel multi-mode HAPS, where the communication payload adaptively switch between multiple modes, namely SMBS, RS, and RIS. We started by comparing the HAPS features to UAVs and LEO satellites. Then, we discuss the characteristics of each HAPS mode and its potential applications. Next, the vision of multi-mode HAPS payload and its selection mechanism is illustrated. Subsequently, the benefits of multi-mode HAPS and the associated potential challenges were presented. Finally, a case study is developed to evaluate the performances of each HAPS mode and to identify the conditions for selecting a specific mode among others.

8.2 Future Research Directions

8.2.1 Hybrid OMA/NOMA Beyond-cell Communications Assisted by HAPS-RIS

In Chapter 6, it is demonstrated that *beyond-cell* communications through HAPS-RIS can work in tandem with terrestrial networks, absorb increase in UEs density and support unserved users. In that study, different network objectives were studied including throughput maximization, worst UE rate maximization, reflecting units minimization and resource efficient maximization. In that study, Orthogonal Multiple Access (OMA) communications were considered to avoid the strong interference between supported UEs. However, given that the HAPS coverage area is wide, and the number of UEs to be supported is large, OMA might not be a spectral-efficient solution. Non Orthogonal Multiple Access (NOMA) is considered as one of the promising technologies for future networks that offer spectral-efficient communications [119]. Therefore, we propose to enhance the "*beyond-cell*" communications through HAPS-RIS by adopting a hybrid OMA/NOMA scheme. The basic idea is that K UEs in the area will be divided in two sets, $K1$ supported through direct connection to BSs, whereas $K2$ will be supported through HAPS-RIS. Then, $K2$ UEs will be divided in clusters, based on their locations. As illustrated in Fig. 8.1, UEs in same clusters use different subcarriers (OMA) communications, while UEs in different clusters can use same subcarriers through NOMA technique. This hybrid OMA/NOMA scheme can be realized in two different ways, as discussed in the following subsections.

8.2.1.1 Frequency-division based NOMA transmission

In this scheme, we divide K_2 users in C clusters with two users in each cluster such that $K_2 = 2C$. Further, total bandwidth is also divided into C subcarriers each of bandwith $\triangle B$. On each subcarrier, not more than two users can be served simultaneously, and the

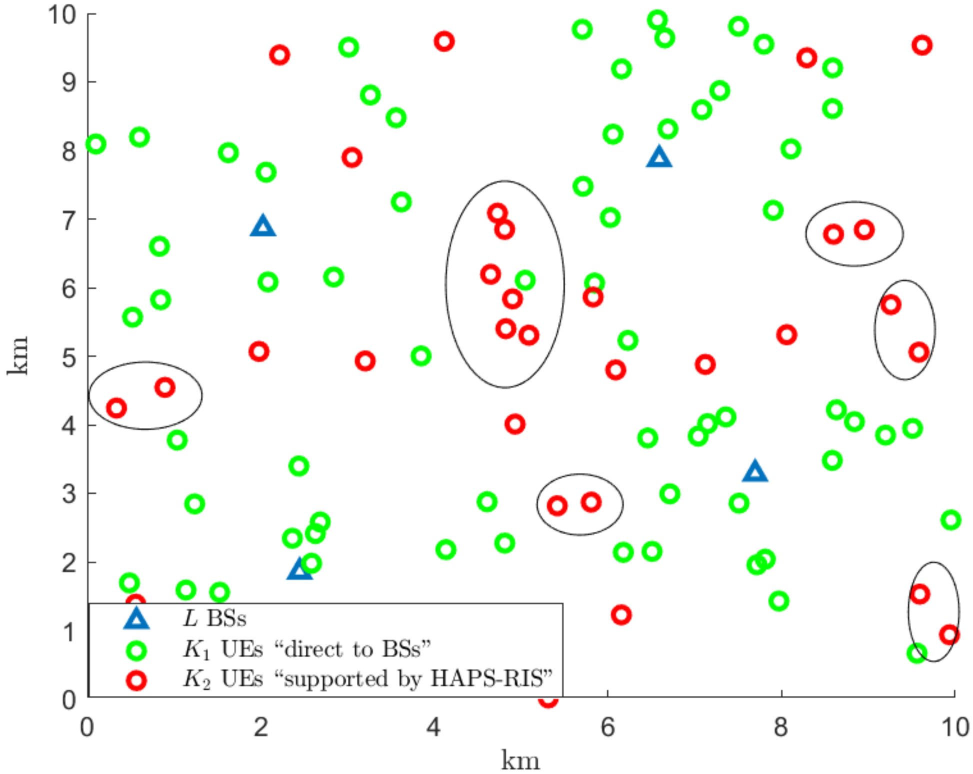

Figure 8.1: Hybrid OMA/NOMA scheme, where UEs in the same cluster use OMA scheme.

data of those two users are transmitted using the NOMA principle. Further, each user is allowed to be served via one subcarrier.

We define a binary user-subcarrier association matrix $\mathbf{F}$ with elements are denoted by $f_{k,j}\, \forall k \in \{1, \ldots, K_2\}, j \in \{1, \ldots, C\}$ and takes value either a 1 or a 0. $f_{k,j} = 1$ indicates that the user k uses the subcarrier j otherwise is zero. The total sum rate (SR) of the proposed system via the FD-based RIS-enabled HAPS is expressed as:

$$\mathrm{SR} = \sum_{j=1}^{C} \frac{1}{C} \sum_{k=1}^{K_2} \log_2 \left(1 + \frac{|\mathbf{h}_{k,j}^H \mathbf{\Phi}_j \mathbf{H}_j|^2 p_{k,j} f_{k,j}}{\sum_{m>i}^{K_2} |\mathbf{h}_{k,j}^H \mathbf{\Phi}_j \mathbf{H}_j|^2 p_{m,j} f_{m,j} + \triangle B N_0} \right), \tag{8.1}$$

where $\mathbf{h}_{k,j}$ and $\mathbf{H}_j$ denote the jth subcarrier's channel vector and matrix between the RIS and the user k and between the control station and the RIS. $\mathbf{\Phi}_j$ denotes the reflection coefficient (RC) matrix used for the subcarrier j and $p_{k,j}$ denotes the power allocated to the user k on the subcarrier j.

8.2.1.2 Time-division based NOMA transmission

In this scheme, the total transmission time is divided into C *equal* timeslots of duration $\triangle T$ and each of the timeslots uses the full available bandwidth. In each timeslot, not more than two users can be served simultaneously, and the data of those two users are transmitted using the NOMA principle. Further, each user is allowed to use only one timeslot.

Similar to the previous case, we define a binary user-timeslot association matrix $\mathbf{F}$ with elements are denoted by $f_{k,j}\,\forall k \in \{1,\ldots,K_2\}, t \in \{1,\ldots,C\}$ and takes value either a 1 or a 0. $f_{k,t} = 1$ indicates that the user k uses the timeslot t otherwise is zero. The total sum rate of the proposed system via the TD-based RIS-enabled HAPS is expressed as:

$$\mathrm{SR} = \sum_{t=1}^{C} \triangle T \sum_{k=1}^{K_2} \log_2\left(1 + \frac{|\mathbf{h}_{k,t}^H \mathbf{\Phi}_t \mathbf{H}_t|^2 p_{k,t} f_{k,t}}{\sum_{m>i}^{K_2} |\mathbf{h}_{k,t}^H \mathbf{\Phi}_t \mathbf{H}_t|^2 p_{m,t} f_{m,t} + \sigma^2}\right), \tag{8.2}$$

where $\mathbf{h}_{k,t}$ and $\mathbf{H}_t$ denote the tth timeslots's channel vector and matrix between the RIS and the user k and between the control station and the RIS. $\mathbf{\Phi}_t$ denotes the RC matrix used for the timeslot t and $p_{k,t}$ denotes the power allocated to the user k in the timeslot t.

8.2.1.3 Problem Formulation

Our goal is to maximize SR of all UEs based on different time/frequency allocation strategies and by utilizing NOMA techniques. The formulated problem and the system constraints can be written as:

$$\begin{aligned}
&\underset{\mathbf{F},\Phi,\mathbf{P}}{\text{maximize}}\ \mathrm{SR} && \text{(8.3a)}\\
&\text{s.t.}\quad R_k \geq R_{\text{th}},\ \ \forall k = 1,2,\ldots,K2 && \text{(8.3b)}\\
&\sum_{j=1}^{C} N_j \leq N_{\max} && \text{(8.3c)}\\
&\phi_{i,k} \in \{0, \Delta\phi, 2\Delta\phi, \ldots, (2^b-1)\Delta\phi\},\ \ \forall i = 1,2,\ldots,N_k,\ \forall k = 1,2,\ldots,K_2, && \text{(8.3d)}\\
&\sum_{j=1}^{J}\sum_{k=1}^{K_2} p_{k,j} \leq P_{\max}^{cs} && \text{(8.3e)}\\
&N_{j,\min} \leq N_j \leq N_{j,\max} && \text{(8.3f)}\\
&\sum_{k=1}^{K_2} f_{k,j} = 2,\ \forall j \in \{1,\ldots,C\} && \text{(8.3g)}\\
&\sum_{j=1}^{J} f_{k,j} = 1,\ \forall j \in \{1,\ldots,C\} && \text{(8.3h)}\\
&f_{k,j} \in \mathbb{B},\ \forall j \in \{1,\ldots,C\}, k \in \{1,\ldots,K_2\} && \text{(8.3i)}
\end{aligned}$$

8.2.2 Configuration of RIS-equipped Aerial Platforms

In Chapter 5, we analyze the link budget of RIS-equipped aerial platforms assuming the RIS has the capability of perfect phase shift. However, in practice, RIS units can be configured for a discrete finite set of phase shifts and thus perfect phase shifts can't be realized.

Indeed, each element of RIS units has a tunable impedance which is controlled using switches. Based on the configuration of the switches, the reflection coefficient can be changed, which implies that the amplitude and phase-shift of the reflected signal are modified. To focus the reflected beam toward a user in a certain direction, as indicated in Fig. 8.2, we need to configure the switches of the RIS units in such a way that the signals from N RIS units will be added constructively at the receiver.

Since the RIS is passive, it will not amplify or process the signals. The transmitter, which might be a BS or a gateway, will send the best configurations for the RIS units.

As a future work, we plan to propose an approach for optimizing the configuration of the RIS units. This will include estimation of the channels and determination of the best configurations. Also, we aim to study the impact of the number of available states for the RIS units on the system complexity and the achieved performance. Furthermore, we intend to investigate the mobility of aerial platforms and the associated effects such the Doppler effects on the RIS configurations.

8.2.2.1 System Model

We consider the RIS-assisted communications on aerial platforms are carried out using orthogonal frequency-division multiplexing (OFDM). Let $x[k]$ denote the transmitted discrete-time signal in the complex baseband domain. The corresponding received discrete-time signal is $y[k]$ in the complex baseband and is given by

$$y[k] = \sum_{l=0}^{M-1} h_\theta[l] x[k-l] + w[k] \tag{8.4}$$

where $h_\theta[l] : l = 0, ..., M-1$ is the finite impulse response (FIR) filter with M coefficients, that describes the communication channel and $w[k]$ is the receiver noise. For K subcarriers, the transmitted OFDM block can be represented as

$$\bar{y}[v] = \bar{h_\theta}[v]\bar{x}[v] + \bar{w}, \;\; v = 0, \dot{K} - 1 \tag{8.5}$$

where

$$\bar{y}[v] = \frac{1}{\sqrt{K}} \sum_{k=0}^{K-1} y[k] e^{-j2\pi kv/K}, \tag{8.6}$$

$$\bar{x}[v] = \frac{1}{\sqrt{K}} \sum_{k=0}^{K-1} x[k] e^{-j2\pi kv/K}, \tag{8.7}$$

$$\bar{h_\theta}[v] = \frac{1}{\sqrt{K}} \sum_{k=0}^{M-1} h[k] e^{-j2\pi kv/K}, \tag{8.8}$$

$$\bar{w}[v] = \frac{1}{\sqrt{K}} \sum_{k=0}^{K-1} w[k] e^{-j2\pi kv/K}. \tag{8.9}$$

In a short form, the received signal of one OFDM block can be written as

$$\bar{\mathbf{y}} = \bar{\mathbf{h}}_\theta \odot \bar{\mathbf{x}} + \bar{\mathbf{w}}, \tag{8.10}$$

where all the vectors are of length K and $\odot$ denotes element-wise product. The discrete-time impulse response of the channel ($h_\theta[k]$) can be represented as

$$h_\theta[k] = \left(\underbrace{\begin{bmatrix} \sqrt{\alpha_1} e^{-j2\pi f_c \tau_{\alpha_1}} \\ \vdots \\ \sqrt{\alpha_N} e^{-j2\pi f_c \tau_{\alpha_N}} \end{bmatrix}}_{\text{Channel Tx-RIS}} \odot \underbrace{\begin{bmatrix} \sqrt{\beta_1} e^{-j2\pi f_c \tau_{\beta_1}} \\ \vdots \\ \sqrt{\beta_N} e^{-j2\pi f_c \tau_{\beta_N}} \end{bmatrix}}_{\text{Channel RIS-Rx}} \right)^T \underbrace{\begin{bmatrix} \sqrt{\gamma_1} e^{-j2\pi f_c \tau_{\theta_1}} \\ \vdots \\ \sqrt{\gamma_N} e^{-j2\pi f_c \tau_{\theta_N}} \end{bmatrix}}_{\text{RIS configurations}} \tag{8.11}$$

where $\{\alpha_n, \tau_{\alpha_n}\}$ and $\{\beta_n, \tau_{\beta_n}\}$ denote the losses between the transmitter and n^{th} element, and from n^{th} element to the receiver, respectively. Also, γ_n and τ_{θ_N} represents the reflection loss and the induced phase shift by the n^{th} element.

It is clear from (8.11) that the channel vector $\bar{\mathbf{h}}_\theta$ depends on the RIS configurations and the cascaded channels between RIS and the transmitter, and between RIS and the receiver.

To select good configurations of the RIS, we need to estimate the unknown part of $\bar{\mathbf{h}}_\theta$, which is the cascaded channels. This can be estimated by sending pilot signals with different configurations, and trying to extract $\bar{\mathbf{h}}_\theta$ from the noisy received signal $\bar{\mathbf{y}}$.

We intend in this line of research to study the estimation of the channel and the optimization of the RIS configurations.

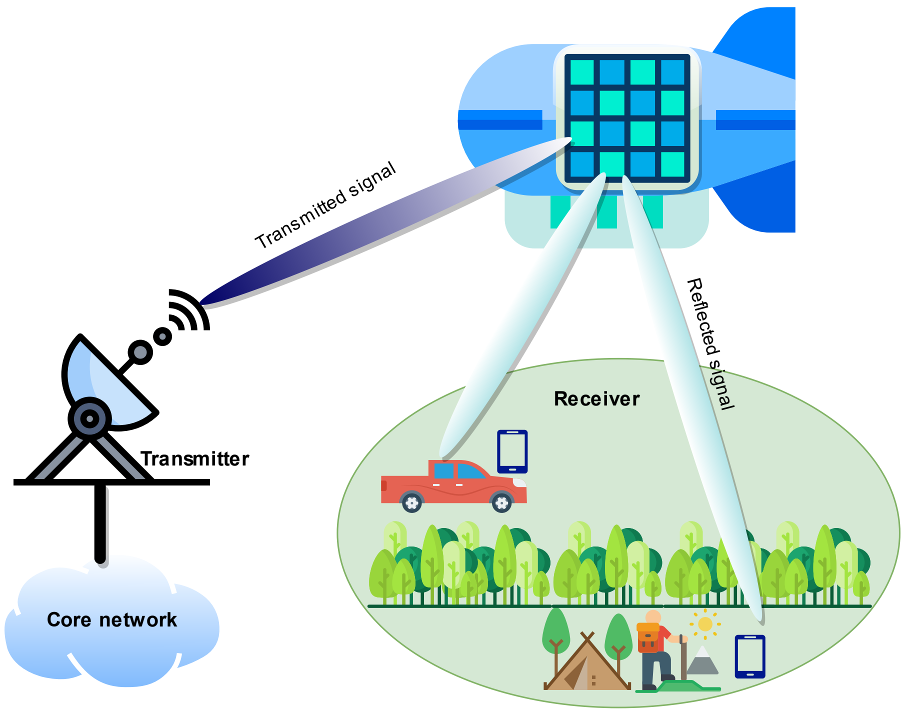

Figure 8.2: RIS on aerial platforms focus the reflected signal toward a targeted user.

8.2.3 Energy Management for HAPS with Reconfigurable Smart Surfaces

The communications performance for RIS-assisted communications was extensively investigated form different aspects in the literature. Although the main motivation introduced for RIS technology is the energy saving, few studies discuss the energy issues for RIS systems. Due to the passive nature of RIS units, the energy consumption of RIS-assisted communications is often ignored in most studies.

In fact, RIS technology consumes energy for controlling and configuring the switches of the RIS units. This energy consumption might be negligible when utilizing RIS in terrestrial environments. However, aerial platforms have limited onboard energy, and therefore the energy consumption analysis of RIS-equipped aerial platforms is essential.

As demonstrated in Chapter 5, HAPS-RIS has superior performance compared to other platforms due to its huge size surface. However, large surfaces consume more energy for configuration, and thus the energy consumption should be carefully studied. Also, the main source of energy for HAPS is the solar energy generated by the solar cells on the surface.

Therefore, the surface areas dedicated to RIS for communications versus the surface area dedicated to solar cells for energy generation should be carefully designed.

As a future work, we intend to fill the gap in literature about analyzing the energy consumption for RIS communication systems. We plan to study this in the context of RIS-equipped HAPS assisted communications. As illustrated in Fig. 8.3, HAPS includes three onboard subsystems, namely, the energy subsystem, flight subsystem and the communication payload subsystem. The energy subsystem is responsible to generate the energy using the solar cells. The generated energy by the energy subsystem is consumed by the other two subsystems. We aim to study the trade off between the achieved performance with RIS-assisted communications and the reduction of the generated energy due a smaller area remaining for the solar cells. Also, we intend to compare that to tradditional HAPS payload, such as HAPS-BS and HAPS-RS.

8.2.3.1 System model

HAPS can relay on different energy sources such as fuel tanks, batteries and microwave or laser beams. However, most recent HAPS projects consider the solar energy as the main energy source for HAPS. Solar panel area (A_p) plays a crucial role in determining the amount of the generated energy (E_g). It is expressed as [120]

$$E_g = A_p \psi G_{Ti} \tag{8.12}$$

where ψ is the efficiency of the solar cells, and G_{Ti} is total solar irradiance per m^2 at stratospheric altitude on a given day of the year at a particular latitude.

The generated energy during the daylight will be stored for night to fulfill the flight and the communications functions. Thus, the total consumed energy by HAPS-RIS (E_{tc}) is

$$E_{tc} = E_f + E_{RIS} \tag{8.13}$$

where E_f is the energy consumed by the flight subsystem, which is dependent on the type of HAPS, the characteristics of its propulsion system and the flight pattern. E_{RIS} is the consumed energy by the RIS layer on the HAPS. The power consumption of RIS units depends on their types, configuration technology and the phase shifting resolution. The consumed energy E_{RIS} can be expressed as

$$E_{RIS} = NP_n(b)T_{com} \tag{8.14}$$

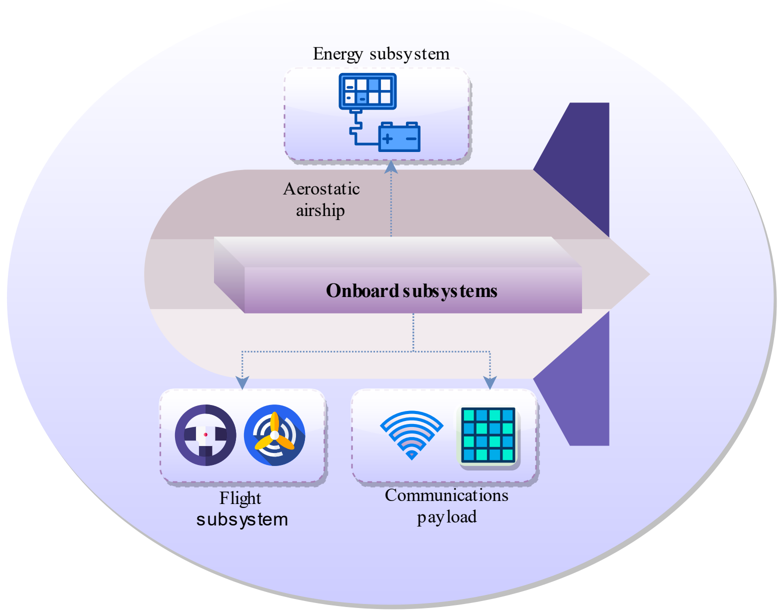

Figure 8.3: HAPS onboard subsystems.

where N denotes the number of reflector units, and $P_n(b)$ stands for the power consumed by each RIS unit with b-bit resolution. T_{com} is the communications duration, which is equal to 3600 s for continuous 24 h communications support.

For sustainable HAPS deployment, the generated energy must be sufficiently large than the consumed energy by the payload and the flight subsystems. As discussed previously, the performance of RIS-assisted communications enhances proportionally with the number of reflector units N and their resolution. However, this will involve an increased of the RIS consumed energy, as indicated in (8.14). Also, increasing N implies reduction in the area for the solar cells A_p, which will reduce E_g, as seen in (8.12). Therefore, careful design and selection of these parameters is essential for energy-efficient HAPS-RIS communications.

8.2.4 Reconfigurable intelligent Surface-Assisted Control of Unmanned Aerial Vehicles in Dense Urban Environments

UAVs have been extensively used for military applications in the past. Nowadays, UAVs are utilized for several civil applications such as package delivery, monitoring, putting off fires, disinfecting areas and collecting data from WSNs. These UAVs are controlled through either a remote controller with a dedicated radio link, or they can be connected and controlled through mobile network. Utilizing terrestrial BSs for controlling UAVS are considered more beneficial due to the potential of real time information exchange between the UAVs and the control BS. Also, the availability of terrestrial BSs and their support of NLOS communications as well as their handover mechanism make them more favorable for controlling UAVs. However, one of the biggest issues that hinder using mobile networks for controlling UAVs is the limited coverage of the terrestrial BSs at the UAV height levels. This is due to current terrestrial BSs are optimized for terrestrial users, where the BS antennas are tilted down for increasing terrestrial coverage and mitigating inter-cell interference. Hence, UAVs in the sky are served by side-lobes of the BS antennas, which results in limited coverage. It is experimentally validated in [121] that in spite of a favorable free space wireless channel between a BS and a UAV, it is subjected to an excessive path loss dependent on the tilt angle and the UAV position. Therefore typically, the mobile network coverage is limited to a maximum height of (1000 ft $\simeq$ 300 m). The popularity of civil applications of UAVs, such as delivery applications, depends on how we can enhance the coverage of mobile networks for aerial users.

To this end, passive reconfigurable intelligent surfaces (RIS) have been introduced as an energy-efficient and cost-effective solution for improving wireless communications. By configuring the RIS units, electromagnetic signals can be adjusted and smartly focused to a target direction. RIS is a thin layer of meta-surface modeled as zero thickness sheet and therefore it is envisioned to coat different environmental objects such as walls of the buildings, furniture, clothing and any object in indoor or outdoor environments [10].

Most of the previous experiments and works about RIS consider their deployment in terrestrial environments to support indoor or outdoor terrestrial users. In Chapters 4 and 5, we introduced our vision of using RIS on aerial platforms and discuss in detail their potentials.

On the other hand, RIS in terrestrial environments can be utilized to support aerial users. We envision in future wireless communications, several buildings, especially in dense urban environments, will be coated by RIS layers to support both terrestrial and aerial users. Through the reflections of coated buildings with RIS, the command and control signals sent by a terrestrial BS can be reflected and focused toward the UAV during its path toward the destination.

8.2.4.1 System model

We consider an urban environment consists of conventional buildings and other modern smart buildings which are coated with RIS. Based on the size of each smart building, the number of reflectors on each building is different. The area of interest is served by a single or several terrestrial BSs dedicated for terrestrial users. A UAV controlled by the BS has to reach the destination point for a certain mission. An illustration of the described system is depicted in Fig. 8.4. In order to support the control signals transmitted by the BS to the UAV, RIS on smart buildings reflect the transmitted signal to the UAV location. As seen in Fig. 8.4, there are three wireless links: (BS-UAV, BS-RIS, and RIS-UAV). The first link is the direct signal between the BS and the UAV, which is modeled by free space path loss model. However, Since the BS antenna is tilted down, a small fraction of the antenna gain contributes to the direct link, while most of transmitted power gain dissipates in the terrestrial network. The received signal at the smart building through the BS-RIS link is subjected to multi-path fading modeled by Rayleigh distribution. The RIS adjust the phases of the received signals and reflect them to the UAV. This RIS-UAV link also undergoes to free space path loss model. The received power signal at the UAV Pr is the sum of the received powers by the direct signal Pr_1 and the reflected signal Pr_{r2}, ($P_r = Pr_1 + Pr_2$). The average received power by the direct signal from the BS to the UAV can be expressed as follows:

$$Pr_1 = \frac{gP_t}{PL_1} \tag{8.15}$$

where $g \ll 1$ represents the partial gain of the transmitted power P_t for the direct link. PL_1 is the average path loss between the BS and the UAV, which can be obtained as follows:

$$PL_1 = \left(\frac{4\pi d_1}{\lambda}\right)^2 \tag{8.16}$$

where λ is the wavelength and d_1 represents the distance from the BS to the UAV.

For the terrestrial link BS-RIS, the average received signal at the RIS (P_{rs}) obtained as

$$P_{rs} = (1-g)\frac{P_t}{PL_2}h \tag{8.17}$$

where h captures the multipath Rayleigh fading effect, and PL_2 represent the terrestrial path loss in the BS-RIS link, which can be obtained as

$$PL_2 = \left(\frac{4\pi d_0}{\lambda}\right)^2 \left(\frac{d_2}{d_0}\right)^\alpha, \alpha > 2 \tag{8.18}$$

where α is the path loss exponent, d_0 is a reference distance and d_2 is the distance between the BS and the RIS.

The RIS in a smart building controlled by software commands adjust the phases of the received multi path signals and reflect them to the UAV location. Let $S(t)$ represents the transmitted signal to the RIS, and N is the number of reflectors in a smart building. Then, the multipath received signal at the RIS is

$$y(t) = \sum_{i=1}^{N} a_i S(t - \tau_i) e^{-j\theta_i} + n \tag{8.19}$$

where a_i and θ_i represents the magnitude and phase of path i. Additionally, n denotes the additive white Gaussian noise (AWGN) with variance N_o.

Assuming narrow band system, $S(t - \tau_i) \approx S(t)$. Then, the received signal after the induced phase shift ϕ_i by each reflector is

$$y(t) = S(t) \sum_{i=1}^{N} a_i e^{-j(\theta_i - \phi_i)} + n. \tag{8.20}$$

We assume perfect knowledge of channel state information and multipath phases. Also, the capability of continuous and full control of RIS is considered. Thus, all the multipath signals are added constructively and the reflected signal will be

$$y(t) = S(t) \sum_{i=1}^{N} a_i + n \tag{8.21}$$

where a_i is a Rayleigh random variable, whose expected value is given as

$$\mathbb{E}[a_i] = \sigma \sqrt{\frac{\pi}{2}} \tag{8.22}$$

where σ is a scaling parameter of the distribution.

Thus, the average power of the reflected signal (P_{ref}) is

$$P_{ref} = \left[S\, N\, \mathbb{E}[a_i]\right]^2. \tag{8.23}$$

The received signal at the UAV which is smartly reflected by the RIS is given as

$$Pr_2 = \frac{P_{ref}}{PL_3} = \frac{\left[S\, N\, \sigma \sqrt{\frac{\pi}{2}}\right]^2}{PL_3} \tag{8.24}$$

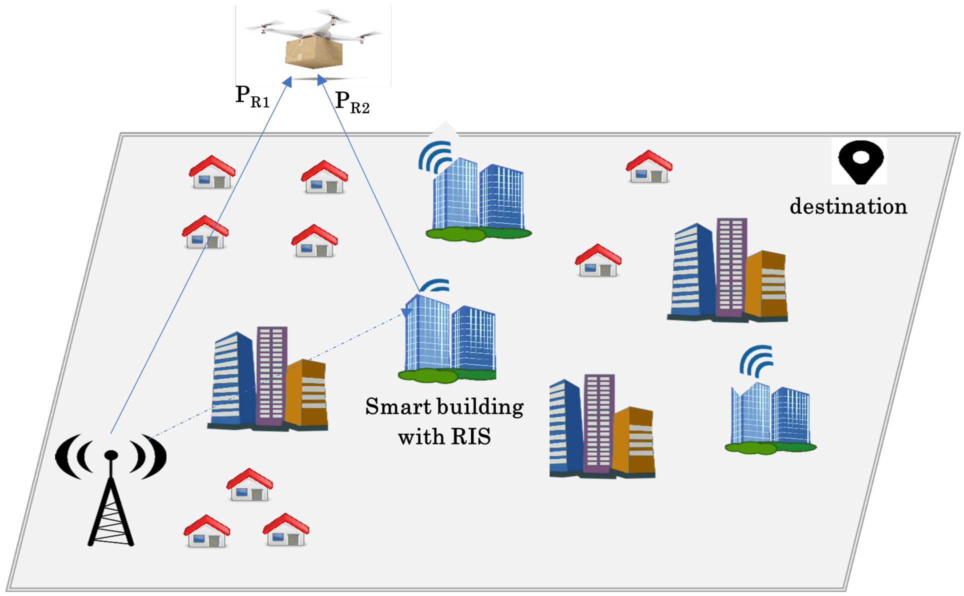

Figure 8.4: BS-UAV communications are supported by reflections from smart buildings.

where PL_3 is the free space path loss between RIS and UAV, which is dependent on the distance between them.

By combining (8.15) , (8.17) and (8.24), the total average received power at the UAV is

$$P_r = \left(\frac{\lambda}{4\pi}\right)^2 P_t \left[\frac{g}{d_1^2} + (1-g)\left(\frac{\lambda}{4\pi d_3 d_0}\right)^2 \left(\frac{d_o}{d_2}\right)^\alpha N^2\, \mathbb{E}[a]^2\right]. \tag{8.25}$$

Accordingly, the received signal-to-noise ratio (SNR) can be written as

$$\gamma = \frac{\left(\frac{\lambda}{4\pi}\right)^2 P_t \left[\frac{g}{d_1^2} + (1-g)\left(\frac{\lambda}{4\pi d_3 d_0}\right)^2 \left(\frac{d_o}{d_2}\right)^\alpha N^2\, \sigma^2 \frac{\pi}{2}\right]}{{\sigma_n}^2}. \tag{8.26}$$

When SNR γ in 8.26 is larger than γ_{th}, the communications to the UAV is considered reliable.

8.2.4.2 Problem Description

We intend to propose a framework for supporting the communication links between BSs and UAV by the reflections of smart buildings. Let (X_0^U, y_0^U, h_u), (X_f^U, y_f^U, h^U) represents the initial location and final destination of the UAV, respectively. Without loss of generality, the UAV is flying at fixed height and at any instant time n, the UAV location is given as $(X^U[n], y^U[n], h^U)$. In order for the UAV to accomplish its mission successfully, the control signals must be received reliably. Therefore, the RIS on smart buildings support the BS control signal through smart reflections. The area of interest has M smart buildings and their locations denotes as $SB = \{(X_1^s, y_1^s, 0), (X_2^s, y_2^s, 0), \ldots, (X_M^s, y_M^s, 0)\}$. The RIS reflectors in the smart buildings will be activated through activation control signals transmitted by the BS. As the UAV comes closer to a smart building, it will get a good reflection gain. However, selecting a route closer to the smart buildings, might increase its flight duration and its consumed energy. Therefore, we need to optimize the UAV route by minimizing its energy consumption. Also, the activation and the configuration of SBs for reflection involves signal processing overhead and energy consumption at the control BS. Therefore, the number of activated building for reflections need to be minimized. Thus, the overall problem seeks to minimize the total consumed energy by the UAV and the smart buildings configuration, by designing the UAV trajectory and optimizing the number and locations of the activated SBs, while guaranteeing reliable communications to the UAV.

References

[1] *IMT Vision–Framework and Overall Objectives of the Future Development of IMT for 2020 and Beyond*, ITU-R M.2083-0, Sep. 2015.

[2] U. Cisco, "Cisco annual internet report (2018–2023) white paper," Cisco: San Jose, CA, USA, 2020.

[3] G. Kurt, M. G. Khoshkholgh, S. Alfattani, A. Ibrahim, T. S. Darwish, M. S. Alam, H. Yanikomeroglu, and A. Yongacoglu, "A vision and framework for the high altitude platform station (HAPS) networks of the future," *IEEE Communications Surveys and Tutorials*, vol. 23, no. 2, pp. 729 – 779, Secondquarter 2021.

[4] F. Rinaldi, H.-L. Maattanen, J. Torsner, S. Pizzi, S. Andreev, A. Iera, Y. Koucheryavy, and G. Araniti, "Non-terrestrial networks in 5G & beyond: A survey," *IEEE Access*, vol. 8, pp. 165 178–165 200, Sep. 2020.

[5] Y. Zeng, Q. Wu, and R. Zhang, "Accessing from the sky: A tutorial on UAV communications for 5G and beyond," *Proceedings of the IEEE*, vol. 107, no. 12, pp. 2327–2375, Dec. 2019.

[6] O. Kodheli, E. Lagunas, N. Maturo, S. K. Sharma, B. Shankar, J. Montoya, J. Duncan, D. Spano, S. Chatzinotas, S. Kisseleff, *et al.*, "Satellite communications in the new space era: A survey and future challenges," *IEEE Communications Surveys and Tutorials*, vol. 23, no. 1, pp. 70–109, Firstquarter 2021.

[7] *Technical Specification Group Radio Access Network; Study on New Radio (NR) to Support Non-Terrestrial Networks*, 3GPP TR 38.811 V15.4.0, Sep. 2020.

[8] *Technical Specification Group Services and System Aspects; Enhancement for Unmanned Aerial Vehicles*, 3GPP TR 22.829 V17.1.0, Sep. 2019.

[9] *Technical Specification Group Services and System Aspects; Unmanned Aerial System (UAS) Support in 3GPP*, 3GPP TS 22.125 V17.2.0, Sep. 2020.

[10] C. Liaskos, S. Nie, A. Tsioliaridou, A. Pitsillides, S. Ioannidis, and I. Akyildiz, “A new wireless communication paradigm through software-controlled metasurfaces,” *IEEE Communications Magazine*, vol. 56, no. 9, pp. 162–169, Sep. 2018.

[11] E. Basar, M. Di Renzo, J. De Rosny, M. Debbah, M.-S. Alouini, and R. Zhang, “Wireless communications through reconfigurable intelligent surfaces,” *IEEE Access*, vol. 7, pp. 116 753–116 773, 2019.

[12] M. Di Renzo, A. Zappone, M. Debbah, M.-S. Alouini, C. Yuen, J. De Rosny, and S. Tretyakov, “Smart radio environments empowered by reconfigurable intelligent surfaces: How it works, state of research, and the road ahead,” *IEEE Journal on Selected Areas in Communications*, vol. 38, no. 11, pp. 2450–2525, Nov. 2020.

[13] F. M. Al-Turjman, H. S. Hassanein, and M. Ibnkahla, “Towards prolonged lifetime for deployed WSNs in outdoor environment monitoring,” *Ad Hoc Networks*, vol. 24, Part A, pp. 172–185, 2015.

[14] R. I. Bor-Yaliniz, A. El-Keyi, and H. Yanikomeroglu, “‘Efficient 3-D placement of an aerial base station in next generation cellular networks,” in *IEEE International Conference on Communications (ICC)*, 2016, pp. 1–5.

[15] M. Alzenad, A. El-Keyi, F. Lagum, and H. Yanikomeroglu, “3-D placement of an unmanned aerial vehicle base station (UAV-BS) for energy-efficient maximal coverage,” *IEEE Wireless Communications Letters*, vol. 64, no. 6, pp. 434–437, Aug. 2016.

[16] Y. Pang, Y. Zhang, Y. Gu, M. Pan, Z. Han, and P. Li, “Efficient data collection for wireless rechargeable sensor clusters in harsh terrains using UAVs,” in *IEEE Global Communications Conference (Globecom)*, 2014, pp. 234–239.

[17] M. Mozaffari, W. Saad, M. Bennis, and M. Debbah, “Unmanned aerial vehicle with underlaid device-to-device communications: performance and tradeoffs,” *IEEE Transactions on Wireless Communications*, vol. 15, no. 6, pp. 3949–3963, Jun. 2016.

[18] Y. Zeng, X. Xu, and R. Zhang, “Trajectory design for completion time minimization in UAV-enabled multicasting,” *IEEE Transactions on Wireless Communications*, vol. 17, no. 4, pp. 2233–2246, Apr. 2018.

[19] Y. Zeng, J. Xu, and R. Zhang, "Energy minimization for wireless communication with rotary-wing UAV," *IEEE Transactions on Wireless Communications*, vol. 18, no. 4, pp. 2329–2345, Apr. 2019.

[20] M. Mozaffari, W. Saad, M. Bennis, and M. Debbah, "Mobile Internet of things: can UAVs provide an energy-efficient mobile architecture?" in *IEEE Global Communications Conference (Globecom)*, 2016, pp. 1–6.

[21] M. Afsar and M.-H. Tayarani, "Clustering in sensor networks: a literature survey," *Elsevier Journal of Network and Computer Applications*, vol. 46, pp. 198–226, Nov. 2014.

[22] F. M. Al-Turjman, H. S. Hassanein, and M. Ibnkahla, "Quantifying connectivity in wireless sensor networks with grid-based deployments," *Journal of Network and Computer Applications*, vol. 36, no. 1, pp. 368–377, 2013.

[23] A. Al-Hourani, S. Kandeepan, and S. Lardner, "Optimal LAP altitude for maximum coverage," *IEEE Wireless Communications Letters*, vol. 3, no. 6, pp. 569–572, Dec. 2014.

[24] T. Kanungo, D. M. Mount, N. S. Netanyahu, C. D. Piatko, R. Silverman, and A. Y. Wu, "An efficient K-means clustering algorithm: analysis and implementation," *IEEE Transactions on Pattern Analysis and Machine Intelligence*, vol. 24, no. 7, pp. 881–892, Jul. 2002.

[25] G. Laporte, "The vehicle routing problem: an overview of exact and approximate algorithms," *European Journal of Operational Research*, vol. 59, no. 3, pp. 345 – 358, Jun. 1992.

[26] E. M. Arkin and R. Hassin, "Approximation algorithms for the geometric covering salesman problem," *Discrete Applied Mathematics*, vol. 55, no. 3, pp. 197–218, Dec. 1994.

[27] T. Bektas, "The multiple traveling salesman problem: an overview of formulations and solution procedures," *Omega*, vol. 34, no. 3, pp. 209 – 219, Jun. 2006.

[28] P. Larranaga, C. Kuijpers, C. Murga, and al, "Genetic algorithms for the travelling salesman problem: a review of representations and operators," *Springer Artificial Intelligence Review*, vol. 13, no. 2, pp. 129–170, Apr. 1999.

[29] F. M. Al-Turjman, H. S. Hassanein, and M. A. Ibnkahla, "Efficient deployment of wireless sensor networks targeting environment monitoring applications," *Computer Communications*, vol. 36, no. 2, pp. 135–148, 2013.

[30] S. Alfattani, W. Jaafar, H. Yanikomeroglu, and A. Yongacoglu, "Multi-UAV data collection framework for wireless sensor networks," in *IEEE Global Communications Conference (Globecom)*, 2019, pp. 1–6.

[31] M. Samir, S. Sharafeddine, C. M. Assi, T. M. Nguyen, and A. Ghrayeb, "UAV trajectory planning for data collection from time-constrained IoT devices," *IEEE Transactions on Wireless Communications*, vol. 19, no. 1, pp. 34–46, Jan. 2020.

[32] C. Zhan, Y. Zeng, and R. Zhang, "Energy-efficient data collection in UAV enabled wireless sensor network," *IEEE Wireless Communications Letters*, vol. 7, no. 3, pp. 328–331, Jun. 2018.

[33] A. T. Albu-Salih and S. A. H. Seno, "Energy-efficient data gathering framework-based clustering via multiple UAVs in deadline-based WSN applications," *IEEE Access*, vol. 6, pp. 72 275–72 286, 2018.

[34] J. K. Lenstra and A. H. G. R. Kan, "Complexity of vehicle routing and scheduling problems," *Networks*, vol. 11, no. 2, pp. 221–227, Summer 1981.

[35] F. Nielsen, *Ch. 8: Hierarchical Clustering - Introduction to HPC with MPI for Data Science*. Springer, 2016.

[36] D. Knuth. Capacitated vehicle routing problem, OR-tools. [Online]. Available: https://developers.google.com/optimization/routing/cvrp

[37] "NTT DOCOMO and metawave announce successful demonstration of 28 GHz-band 5G using world's first meta-structure technology." [Online]. Available: https://bwnews.pr/2IhH8cc

[38] "Visosurf: A hardware platform for software-driven functional metasurfaces." [Online]. Available: http://www.visorsurf.eu

[39] J. Kimionis, W. Su, J. Hester, J. Bito, X. He, T.-H. Lin, and M. M. Tentzeris, "Zero-power sensors for smart objects: Novel zero-power additively manufactured wireless sensor modules for iot applications," *IEEE Microwave Magazine*, vol. 19, no. 6, pp. 32–47, Sep. 2018.

[40] "Frequency selective surfaces (urbanFSS)." [Online]. Available: https://ggisolutions.com/solutions/fss-frequency-selective-surface/

[41] Z. Peng, L. Li, M. Wang, Z. Zhang, Q. Liu, Y. Liu, and R. Liu, "An effective coverage scheme with passive-reflectors for urban millimeter-wave communication," *IEEE Antennas and Wireless Propagation Letters*, vol. 15, pp. 398–401, Jun. 2015.

[42] S. Hu, F. Rusek, and O. Edfors, "Beyond massive MIMO: The potential of data transmission with large intelligent surfaces," *IEEE Transactions on Signal Processing*, vol. 66, no. 10, pp. 2746–2758, May 2018.

[43] N. Yu, P. Genevet, M. A. Kats, F. Aieta, J.-P. Tetienne, F. Capasso, and Z. Gaburro, "Light propagation with phase discontinuities: Generalized laws of reflection and refraction," *Science*, vol. 334, no. 6054, pp. 333–337, Oct. 2011.

[44] T. J. Cui, M. Q. Qi, X. Wan, J. Zhao, and Q. Cheng, "Coding metamaterials, digital metamaterials and programmable metamaterials," *Light: Science & Applications*, vol. 3, no. 10, p. e218, Oct. 2014.

[45] Q. Wu and R. Zhang, "Intelligent reflecting surface enhanced wireless network via joint active and passive beamforming," *IEEE Transactions on Wireless Communications*, vol. 18, no. 11, pp. 5394–5409, Nov. 2019.

[46] X. Tan, Z. Sun, D. Koutsonikolas, and J. M. Jornet, "Enabling indoor mobile millimeter-wave networks based on smart reflect-arrays," in *IEEE Conference on Computer Communications (INFOCOM)*, 2018, pp. 270–278.

[47] C. Huang, G. C. Alexandropoulos, A. Zappone, M. Debbah, and C. Yuen, "Energy efficient multi-user MISO communication using low resolution large intelligent surfaces," in *IEEE Global Communications Workshops (Globecom Workshops)*, 2018, pp. 1–6.

[48] J. Y. Dai, W. K. Tang, J. Zhao, X. Li, Q. Cheng, J. C. Ke, M. Z. Chen, S. Jin, and T. J. Cui, "Wireless communications through a simplified architecture based on time-domain digital coding metasurface," *Advanced Materials Technologies*, vol. 4, no. 7, p. 1900044, Feb. 2019.

[49] H. Kamoda, T. Iwasaki, J. Tsumochi, T. Kuki, and O. Hashimoto, "60-GHz electronically reconfigurable large reflectarray using single-bit phase shifters," *IEEE Transactions on Antennas and Propagation*, vol. 59, no. 7, pp. 2524–2531, Jul. 2011.

[50] S. V. Hum, M. Okoniewski, and R. J. Davies, "Modeling and design of electronically tunable reflectarrays," *IEEE Transactions on Antennas and Propagation*, vol. 55, no. 8, pp. 2200–2210, Aug. 2007.

[51] S. V. Hum, G. McFeetors, and M. Okoniewski, "Integrated MEMS reflectarray elements," in *IEEE First European Conference on Antennas and Propagation*, 2006, pp. 1–6.

[52] J. Perruisseau-Carrier and A. Skrivervik, "Monolithic MEMS-based reflectarray cell digitally reconfigurable over a 360° phase range," *IEEE Antennas and Wireless Propagation Letters*, vol. 7, pp. 138–141, Feb. 2008.

[53] G. Perez-Palomino, P. Baine, R. Dickie, M. Bain, J. A. Encinar, R. Cahill, M. Barba, and G. Toso, "Design and experimental validation of liquid crystal-based reconfigurable reflectarray elements with improved bandwidth in F-band," *IEEE Transactions on Antennas and Propagation*, vol. 61, no. 4, pp. 1704–1713, Apr. 2013.

[54] E. Carrasco, M. Tamagnone, and J. Perruisseau-Carrier, "Tunable graphene reflective cells for THz reflectarrays and generalized law of reflection," *Applied Physics Letters*, vol. 102, no. 10, pp. 1–5, Mar. 2013.

[55] E. Carrasco and J. Perruisseau-Carrier, "Reflectarray antenna at terahertz using graphene," *IEEE Antennas and Wireless Propagation Letters*, vol. 12, pp. 253–256, Feb. 2013.

[56] M. Alzenad, M. Z. Shakir, H. Yanikomeroglu, and M.-S. Alouini, "FSO-based vertical backhaul/fronthaul framework for 5G+ wireless networks," *IEEE Communications Magazine*, vol. 56, no. 1, pp. 218–224, Jan. 2018.

[57] Z. Jia, M. Sheng, J. Li, and Z. Han, "Towards data collection and transmission in 6G space-air-ground integrated networks: Cooperative HAP and LEO satellite schemes," *IEEE Internet of Things Journal*, vol. 9, no. 13, pp. 10 516–10 528, Jul. 2022.

[58] W. Tang, M. Z. Chen, X. Chen, J. Y. Dai, Y. Han, M. Di Renzo, Y. Zeng, S. Jin, Q. Cheng, and T. J. Cui, "Wireless communications with reconfigurable intelligent surface: Path loss modeling and experimental measurement," *IEEE Transactions on Wireless Communications*, vol. 20, no. 1, pp. 421–439, Jan. 2021.

[59] H. Lu, Y. Zeng, S. Jin, and R. Zhang, "Enabling panoramic full-angle reflection via aerial intelligent reflecting surface," in *IEEE International Conference on Communications Workshops (ICC Workshops)*, 2020, pp. 1–6.

[60] M. Samir, M. Elhattab, C. Assi, S. Sharafeddine, and A. Ghrayeb, "Optimizing age of information through aerial reconfigurable intelligent surfaces: A deep reinforcement learning approach," *IEEE Transactions on Vehicular Technology*, vol. 70, no. 4, pp. 3978–3983, Apr. 2021.

[61] C. O. Nnamani, M. R. Khandaker, and M. Sellathurai, "Joint beamforming and location optimization for secure data collection in wireless sensor networks with UAV-carried intelligent reflecting surface," *arXiv preprint arXiv:2101.06565*, Jan. 2021.

[62] M. Jung, W. Saad, and G. Kong, "Performance analysis of active large intelligent surfaces (LISs): Uplink spectral efficiency and pilot training," *IEEE Transactions on Communications*, vol. 69, no. 5, pp. 3379–3394, May 2021.

[63] "Starlink." [Online]. Available: https://www.starlink.com/

[64] "Stratobus: Why this stratospheric airship is already being called a "swiss knife" in the sky." [Online]. Available: https://www.thalesgroup.com/en/worldwide/space/magazine/stratobus-why-stratospheric-airship-already-being-called-swiss-knife-sky

[65] "Nokia drone networks." [Online]. Available: https://dac.nokia.com/applications/nokia-drone-networks/

[66] M. Di Renzo, M. Debbah, D.-T. Phan-Huy, A. Zappone, M.-S. Alouini, C. Yuen, V. Sciancalepore, G. C. Alexandropoulos, J. Hoydis, H. Gacanin, *et al.*, "Smart radio environments empowered by reconfigurable AI meta-surfaces: An idea whose time has come," *EURASIP Journal on Wireless Communications and Networking*, vol. 129, no. 1, pp. 1–20, May 2019.

[67] Q. Wu, S. Zhang, B. Zheng, C. You, and R. Zhang, "Intelligent reflecting surface aided wireless communications: A tutorial," *IEEE Transactions on Communications*, vol. 69, no. 5, pp. 3313–3351, May 2021.

[68] S. Gong, X. Lu, D. T. Hoang, D. Niyato, L. Shu, D. I. Kim, and Y.-C. Liang, "Toward smart wireless communications via intelligent reflecting surfaces: A contemporary

survey," *IEEE Communications Surveys and Tutorials*, vol. 22, no. 4, pp. 2283–2314, Fourthquarter 2020.

[69] S. Alfattani, W. Jaafar, Y. Hmamouche, H. Yanikomeroglu, A. Yongaçoglu, N. Đào, and P. Zhu, "Aerial platforms with reconfigurable smart surfaces for 5G and beyond," *IEEE Communications Magazine*, vol. 59, no. 1, pp. 96–102, Jan. 2021.

[70] A. S. Abdalla, T. F. Rahman, and V. Marojevic, "UAVs with reconfigurable intelligent surfaces: Applications, challenges, and opportunities," *arXiv preprint, [Online]. Available: https://arxiv.org/abs/2012.04775*, Dec. 2020.

[71] B. Shang, R. Shafin, and L. Liu, "UAV swarm-enabled aerial reconfigurable intelligent surface (SARIS)," *IEEE Wireless Communications*, vol. 28, no. 5, pp. 156–163, Oct. 2021.

[72] K. Tekbiyik, G. K. Kurt, A. Ekti, A. Görcin, and H. Yanikomeroglu, "Reconfigurable intelligent surface empowered terahertz communication for LEO satellite networks," *arXiv preprint, [Online]. Available: https://arxiv.org/abs/2007.04281*, Dec. 2020.

[73] I. Yildirim, A. Uyrus, and E. Basar, "Modeling and analysis of reconfigurable intelligent surfaces for indoor and outdoor applications in future wireless networks," *IEEE Transactions on Communications*, vol. 69, no. 2, pp. 1290–1301, Feb. 2021.

[74] O. Özdogan, E. Björnson, and E. G. Larsson, "Intelligent reflecting surfaces: physics, propagation, and pathloss modeling," *IEEE Wireless Communications Letters*, vol. 9, no. 5, pp. 581–585, May 2019.

[75] Q.-U.-A. Nadeem, H. Alwazani, A. Kammoun, A. Chaaban, M. Debbah, and M.-S. Alouini, "Intelligent reflecting surface-assisted multi-user MISO communication: Channel estimation and beamforming design," *IEEE Open Journal of the Communications Society*, vol. 1, pp. 661–680, 2020.

[76] M. Di Renzo, K. Ntontin, J. Song, F. H. Danufane, X. Qian, F. Lazarakis, J. de Rosny, D. T. Phan-Huy, O. Simeone, R. Zhang, M. Debbah, G. Lerosey, M. Fink, S. Tretyakov, and S. Shamai, "Reconfigurable intelligent surfaces vs. relaying: Differences, similarities, and performance comparison," *IEEE Open Journal of the Communications Society*, vol. 1, p. 798–807, 2020.

[77] E. Basar and I. Yildirim, "SimRIS channel simulator for reconfigurable intelligent surface-empowered communication systems," in *IEEE Latin-American Conference on Communications (LATINCOM)*, 2020, pp. 1–6.

[78] S. W. Ellingson, "Path loss in reconfigurable intelligent surface-enabled channels," *arXiv preprint, [Online]. Available: https://arxiv.org/abs/1912.06759*, Dec. 2019.

[79] J. C. B. Garcia, A. Sibille, and M. Kamoun, "Reconfigurable intelligent surfaces: Bridging the gap between scattering and reflection," *IEEE Journal on Selected Areas in Communications*, vol. 38, no. 11, pp. 2538–2547, Nov. 2020.

[80] E. Björnson, H. Wymeersch, B. Matthiesen, P. Popovski, L. Sanguinetti, and E. de Carvalho, "Reconfigurable intelligent surfaces: A signal processing perspective with wireless applications," *IEEE Signal Processing Magazine*, vol. 39, no. 2, pp. 135–158, Mar. 2022.

[81] S. V. Hum and J. Perruisseau-Carrier, "Reconfigurable reflectarrays and array lenses for dynamic antenna beam Control: A review," *IEEE Transactions on Antennas and Propagation*, vol. 62, no. 1, pp. 183–198, Jan. 2014.

[82] Q. Wu and R. Zhang, "Beamforming optimization for wireless network aided by intelligent reflecting surface with discrete phase shifts," *IEEE Transactions on Communications*, vol. 68, no. 3, pp. 1838–1851, Mar. 2020.

[83] T. S. Rappaport, *Wireless Communications: Principles and Practice.* Prentice Hall PTR New Jersey, 1996, vol. 2.

[84] E. Björnson, O. Özdogan, and E. G. Larsson, "Reconfigurable intelligent surfaces: Three myths and two critical questions," *IEEE Communications Magazine*, vol. 58, no. 12, pp. 90–96, Dec. 2020.

[85] *Study on Channel Model for Frequencies from 0.5 to 100 GHz*, 3GPP TR 38.901 V14.3.0, Jan. 2018.

[86] *Prediction of Building Entry Loss*, ITU-R P.2109-1 P Series, Aug. 2019.

[87] *Study on Enhanced LTE Support for Aerial Vehicles*, 3GPP TR 36.777 V1.0.0, Dec. 2017.

[88] M. Mozaffari, W. Saad, M. Bennis, Y.-H. Nam, and M. Debbah, "A tutorial on UAVs for wireless networks: Applications, challenges, and open problems," *IEEE Communications Surveys and Tutorials*, vol. 21, no. 3, pp. 2334–2360, Thirdquarter 2019.

[89] M. S. Alam, G. K. Kurt, H. Yanikomeroglu, P. Zhu, and N. D. Đào, "High altitude platform station based super macro base station constellations," *IEEE Communications Magazine*, vol. 59, no. 1, pp. 103–109, Jan. 2021.

[90] *Preferred Characteristics of Systems in the Fixed Service Using High Altitude Platforms Operating in the Bands 47.2-47.5 GHz and 47.9-48.2 GHz*, ITU-R F.1500, May 2000.

[91] C. E. Fossa, R. A. Raines, G. H. Gunsch, and M. A. Temple, "An overview of the Iridium (R) low earth orbit (LEO) satellite system," in *Proceedings of the IEEE National Aerospace and Electronics Conference. (NAECON)*, 1998, pp. 152–159.

[92] S. Cakaj, "The coverage belt for low earth orbiting satellites," in *39th International Convention on Information and Communication Technology, Electronics and Microelectronics (ICICTEM)*, 2016, pp. 554–557.

[93] Y. Su, Y. Liu, Y. Zhou, J. Yuan, H. Cao, and J. Shi, "Broadband LEO satellite communications: Architectures and key technologies," *IEEE Wireless Communications*, vol. 26, no. 2, pp. 55–61, Apr. 2019.

[94] "Hosting payloads on a communication constellation." [Online]. Available: https://directory.eoportal.org/web/eoportal/satellite-missions/i/iridium-next

[95] "Starlink satellite dimension estimates." [Online]. Available: https://lilibots.blogspot.com/2020/04/starlink-satellite-dimension-estimates.html

[96] *Attenuation by Atmospheric Gases*, ITU-R P.676-10, Sep. 2013.

[97] *Reference Standard Atmospheres*, ITU-R P.835-6 P Series, Dec. 2017.

[98] *Ionospheric Propagation Data and Prediction Methods Required for the Design of Satellite Networks and Systems*, ITU-R P.531-14 P Series, Aug. 2019.

[99] *Propagation Data and Prediction Methods Required for the Design of Earth-space Telecommunication Systems*, ITU-R P.618-13 P Series, Dec. 2017.

[100] C. De Alwis, A. Kalla, Q.-V. Pham, P. Kumar, K. Dev, W.-J. Hwang, and M. Liyanage, "Survey on 6G frontiers: Trends, applications, requirements, technologies and future research," *IEEE Open Journal of the Communications Society*, vol. 2, pp. 836–886, 2021.

[101] F. Marzouk, J. P. Barraca, and A. Radwan, "On energy efficient resource allocation in shared RANs: Survey and qualitative analysis," *IEEE Communications Surveys & Tutorials*, vol. 22, no. 3, pp. 1515–1538, Thirdquarter 2020.

[102] M. A. Kishk and M.-S. Alouini, "Exploiting randomly located blockages for large-scale deployment of intelligent surfaces," *IEEE Journal on Selected Areas in Communications*, vol. 39, no. 4, pp. 1043–1056, Apr. 2020.

[103] S. Alfattani, W. Jaafar, Y. Hmamouche, H. Yanikomeroglu, and A. Yongaçoglu, "Link budget analysis for reconfigurable smart surfaces in aerial platforms," *IEEE Open Journal of the Communications Society*, vol. 2, pp. 1980–1995, 2021.

[104] Y. Lu and H. H. Zhou, "Statistical and computational guarantees of Lloyd's algorithm and its variants," *arXiv preprint arXiv:1612.02099*, Dec. 2016.

[105] M. Rivera, M. Chegini, W. Jaafar, S. Alfattani, and H. Yanikomeroglu, "Optimization of quantized phase shifts for reconfigurable smart surfaces assisted communications," in *IEEE 19th Annual Consumer Communications & Networking Conference (CCNC)*, Las Vegas, USA, 2022, pp. 901–904.

[106] S. Boyd, S.-J. Kim, L. Vandenberghe, and A. Hassibi, "A tutorial on geometric programming," *Optimization and Engineering*, vol. 8, no. 1, pp. 67–127, Apr. 2007.

[107] O. M. Rosabal, O. L. A. López, D. E. Pérez, M. Shehab, H. Hilleshein, and H. Alves, "Minimization of the worst case average energy consumption in UAV-assisted IoT networks," *IEEE Internet of Things Journal*, vol. 9, no. 17, pp. 15 827–15 838, Mar. 2022.

[108] G. Geraci, A. Garcia-Rodriguez, M. M. Azari, A. Lozano, M. Mezzavilla, S. Chatzinotas, Y. Chen, S. Rangan, and M. D. Renzo, "What will the future of UAV cellular communications be? A flight from 5G to 6G," *IEEE Communications Surveys and Tutorials*, vol. 24, no. 3, pp. 1304–1335, Third quarter 2022.

[109] R. Wang, M. A. Kishk, and M.-S. Alouini, "Ultra-dense LEO satellite-based communication systems: A novel modeling technique," *IEEE Communications Magazine*, vol. 60, no. 4, pp. 25–31, Apr. 2022.

[110] W. Jaafar and H. Yanikomeroglu, "HAPS-ITS: Enabling future ITS services in trans-continental highways," *IEEE Communications Magazine*, vol. 60, no. 10, pp. 80–86, Oct. 2022.

[111] N. Cherif, W. Jaafar, H. Yanikomeroglu, and A. Yongacoglu, "3D aerial highway: The key enabler of the retail industry transformation," *IEEE Communications Magazine*, vol. 59, no. 9, pp. 65–71, Sep. 2021.

[112] H. Long, M. Chen, Z. Yang, B. Wang, Z. Li, X. Yun, and M. Shikh-Bahaei, "Reflections in the sky: Joint trajectory and passive beamforming design for secure UAV networks with reconfigurable intelligent surface," *arXiv preprint arXiv:2005.10559*, Jun. 2020.

[113] S. Alfattani, A. Yadav, H. Yanikomeroglu, and A. Yongacoglu, "Beyond-cell communications via HAPS-RIS," in *IEEE Global Communications Workshops (Globecom Workshops)*, 2022, pp. 1–6.

[114] T. Shafique, H. Tabassum, and E. Hossain, "Optimization of wireless relaying with flexible UAV-borne reflecting surfaces," *IEEE Transactions on Communications*, vol. 69, no. 1, pp. 309–325, Jan. 2021.

[115] Q. Ren, O. Abbasi, G. K. Kurt, H. Yanikomeroglu, and J. Chen, "High altitude platform station (HAPS) assisted computing for intelligent transportation systems," in *IEEE Global Communications Conference (Globecom)*, 2021, pp. 1–6.

[116] G. Vallero, D. Renga, and M. Meo, "Caching in the air: High altitude platform stations for urban environments," in *Wireless Communications and Networking Conference (WCNC)*, 2022, pp. 2244–2249.

[117] W. Jaafar, S. Naser, S. Muhaidat, P. C. Sofotasios, and H. Yanikomeroglu, "Multiple access in aerial networks: From orthogonal and non-orthogonal to rate-splitting," *IEEE Open Journal of Vehicular Technology*, vol. 1, pp. 372–392, Oct. 2020.

[118] C. Huang, A. Zappone, G. C. Alexandropoulos, M. Debbah, and C. Yuen, "Reconfigurable intelligent surfaces for energy efficiency in wireless communication," *IEEE Transactions on Wireless Communications*, vol. 18, no. 8, pp. 4157–4170, Aug. 2019.

[119] B. K. S. Lima, A. S. de Sena, R. Dinis, D. B. Da Costa, M. Beko, R. Oliveira, and M. Debbah, "Aerial intelligent reflecting surfaces in MIMO-NOMA networks: Fundamentals, potential achievements, and challenges," *IEEE Open Journal of the Communications Society*, vol. 3, pp. 1007–1024, 2022.

[120] S. C. Arum, D. Grace, P. D. Mitchell, M. D. Zakaria, and N. Morozs, "Energy management of solar-powered aircraft-based high altitude platform for wireless communications," *Electronics*, vol. 9, no. 1, p. 179, Jan. 2020.

[121] A. Al-Hourani and K. Gomez, "Modeling cellular-to-UAV path-loss for suburban environments," *IEEE Wireless Communications Letters*, vol. 7, no. 1, pp. 82–85, Feb. 2018.